Functionalization and Fabrication of Single-Walled Carbon Nanotube-based Chemiresistors for Sensory Applications

ARCHIVES
MASSACHUSETTS INSTITUTE OF TECHNOLOGY
JUN 23 2015
LIBRARIES

by

Kelvin Mitchell Frazier

B.S. *magna cum laude* Chemistry & Mathematics, Savannah State University, 2010

Submitted to the Department of Chemistry
In Partial Fulfillment of the Requirements for the Degree of

DOCTOR OF PHILOSOPHY IN CHEMISTRY

at the

MASSACHUSETTS INSTITUTE OF TECHNOLOGY

June 2015

©2015 Massachusetts Institute of Technology. All Rights Reserved.

Signature of Author: Signature redacted
Department of Chemistry
May 5, 2015

Certified by: Signature redacted
Timothy M. Swager
Thesis Supervisor

Accepted by: Signature redacted
Robert W. Field
Chairman, Department Committee on Graduate Students

This doctoral thesis has been examined by a Committee at the Department of Chemistry as follows:

Professor Moungi Bawendi: Signature redacted
Chairman

Professor Timothy M. Swager: Signature redacted
Thesis Supervisor

Professor Keith Nelson: Signature redacted
Department of Chemistry

Dedicated to my parents (Richard Frazier, Jr. and Edythe Frazier), my brother (Ricky Frazier, III), and the rest of my family and friends

In Memory of my grandmother Hattie M. Frazier (1930-2009)

Functionalization and Fabrication of Single-Walled Carbon Nanotube-based Chemiresistors for Sensory Applications

by

Kelvin Mitchell Frazier

Submitted to the Department of Chemistry on May 5, 2015
In Partial Fulfillment of the Requirements for the Degree of
Doctor of Philosophy in Chemistry

ABSTRACT

Chemical sensors that identify and monitor volatile organic compounds (VOCs) have an important role in assessing public security, food and water quality, industrial environment, and health. The fabrication of carbon-based sensors by printing, dip coating, drop casting, or drawing has advantages of being simple and low-cost without the need for highly specialized facilities. We have investigated the fabrication of sensors both by drop casting and drawing.

Single-walled carbon nanotubes (SWCNT) electronic and spectroscopic properties for sensory applications are described. SWCNTs have unique properties wherein their conductance can be altered by environmental effects. These carbon nanomaterials can be easily integrated into a chemiresitive device to detect various analytes.

In our studies using the drop cast method, we noncovalently functionalized SWCNT with a trifunctional selector that has three important properties: it noncovalently functionalizes SWCNTs with cofacial π–π interactions, it binds to cyclohexanone (a target analyte for explosive detection) via hydrogen bond, and it improves the overall robustness of SWCNT-based chemiresistors (e.g., humidity and heat).

In our other studies, we fabricated sensors by drawing. Abrasion is a safe, simple, solvent-free, and low cost method for deposition of carbon-based materials onto a substrate. We successfully demonstrated fabrication on a wide variety of substrates (e.g., weighing paper, polymethyl methacrylate, silicon, and adhesive tape) of fully-drawn chemical sensors on a chip that can detect in real time parts-per-million (ppm) quantities of various vapors using SWCNTs as sensing materials and graphite as electrodes. This fabrication methodology does not require specialized facilities (e.g., clean room, thermal evaporator) and can be performed entirely on a desktop (with appropriate ventilation and safety precautions for handling nanomaterials).

We also extended the abrasion method to detect anions such as fluoride (use to manufacture nuclear weapons) and cyanide (chemical warfare agent). These sensor are highly sensitive detecting the United State Environmental Protection Agency (EPA) maximum contaminant level (MCL) of fluoride and cyanide selectively.

Thesis Supervisor: Timothy M. Swager

Title: John D. MacArthur Professor of Chemistry

Table of Contents

Title Page.....1

Signature Page.....2

Dedication.....3

Abstract.....4

Table of Contents.....5

List of Abbreviations.....7

List of Figures.....9

List of Schemes.....16

List of Tables.....17

Chapter 1: Introduction Of Carbon Nanotube's Structural, Electronic, Spectroscopic, and Sensory Properties.....18

1.1 Introduction to Carbon Materials.....19
1.2 Structural Properties of Carbon Nanotubes.....20
1.3 Electronic Properties.....24
1.4 Spectroscopic characterization of Single-walled Carbon Nanotubes.....31
1.4.1 Raman Spectroscopy.....31
1.4.2 Absorption Spectroscopy.....35
1.5 Carbon Nanotube Electron Transport Applications.....37
1.6 Conclusion.....40
1.7 References.....40

Chapter 2: Robust Cyclohexanone Selective Chemiresistors Based on Single-Walled Carbon Nanotubes.....42

2.1 Introduction.....42
2.2 Results and Discussion.....46
2.3 Conclusion.....52
2.4 Experimental Section.....53
2.5 References.....54
Appendix.....57

Chapter 3: Fully-drawn carbon-based chemical sensors on organic and inorganic surfaces.....87

3.1 Introduction....88
3.2 Results and Discussion....91
3.2.1 Partially-drawn sensors: mechanical abrasion of only chemiresistive materials....91
3.2.2 Graphite electrodes by mechanical abrasion....94
3.2.3 Fabrication of fully-drawn chemical sensors....95
3.2.4 Comparing performance of fully-drawn and partially-drawn sensors....97
3.2.5 Fully-drawn sensing arrays....99
3.3 Conclusion....100
3.4 Experimental Section....101
3.4.1 Fabrication of PENCILs....101
3.4.2 Fabrication of partially-drawn sensors....102
3.4.3 Laser-etching procedure....103
3.4.4 Fabrication of fully-drawn sensors....103
3.4.5 Investigation of the sensory performance of devices....103
3.5 References....104
Appendix....108

Chapter 4: Mechanical Abrasion of Chemiresistive Anion Sensor Array Based on Single-Walled Carbon Nanotubes....133

4.1 Introduction....133
4.2 Results and Discussion....136
4.3 Conclusion....141
4.4 Experimental Section....142
4.5 References....143
Appendix....147

Curriculum Vitae....150

Acknowledgements....152

List of Abbreviations

ACGIH	American Conference of Governmental Industrial Hygienists
$\phi_i(\boldsymbol{k})$	Bloch functions
BZ	Brillouin zone
C-C	carbon-carbon
CNTs	carbon nanotubes
M	center edge of the Brillouin zone
Γ	center of the Brillouin zone
CVD	chemical vapor deposition
θ	chiral angle
(n, m)	chiral index
$\overrightarrow{\boldsymbol{C_h}}$	chiral vector
K	corner of Brillouin zone
RDX	Cyclotrimethylene trinitramine
DOS	density of states
d_t	diameter of the nanotube
DMMP	Dimethyl methylphosphonate
D-band	disorder-induced mode
DWCNTs	double-walled carbon nanotubes
DRAFT	Deposition of Resistors with Abrasion Fabrication Technique
E_g	energy band gap
$E_{g2D}^{\pm}$	energy-dispersion relation of two-dimensional graphite
$E_{\mu}^{\pm}(k)$	energy-dispersion relation of single-walled carbon nanotubes
$\Psi(\mathbf{k})$	eigenfunction
$E_{\boldsymbol{k}}$	eigenenergy
E_F	Fermi level
GC-MS	gas chromatography-mass spectrometry
V_g	gate voltage
gcd	greatest common divisor

H_k	Hamiltonian
HiPCO	high-pressure carbon monoxide conversion
$\boldsymbol{R}$	lattice vector
LOD	limit of detection
MCL	maximum contaminant level
MWCNTs	multi-walled carbon nanotubes
NIR	near-infrared
N	number of unit cells
G'-band	overtone of the disorder-induced mode
ppm	parts per million
ppt	parts per trillion
PTES	phenyltriethoxysilane
PEG	polyethylene glycol
PMMA	polymethyl methacrylate
PCA	Principle Component Analysis
PENCILs	process enhanced nanocarbon for integrated logic
RBM	radial-breathing-mode
RMS	root-mean-square
SWCNTs	single-walled carbon nanotubes
G-band	tangential mode
THF	tetrahydrofuran
$\vec{\boldsymbol{T}}$	translation vector
TES	triethoxysilane
TEC	triethyl citrate
UV	ultraviolet
EPA	United State Environmental Protection Agency
Vis	visible
VOCs	volatile organic compounds
$\mathbf{k}$	wavevector

List of Figures

Chapter 1.

Figure 1.1. Labeled graphene sheet indicating the nanotube's structural and electronic properties. The chiral vector $\overrightarrow{KV} = \overrightarrow{C_h} = 7\overrightarrow{a_1} + 4\overrightarrow{a_2}$ of a (7,4) nanotube is defined on a honeycomb lattice of carbon atoms with unit vectors $\overrightarrow{a_1}$ and $\overrightarrow{a_2}$. The nanotube's diameter, chiral angle, translation vector, and electronic type (metallic or semiconductor) can be determined by the chiral indices.....21

Figure 1.2. Graphene sheet in both real ($\overrightarrow{a_1}$ and $\overrightarrow{a_2}$) and reciprocal space ($\overrightarrow{b_1}$ and $\overrightarrow{b_2}$). A) The unit cell in real space where the honeycomb lattice contains two carbon atom sites Y and Z. B) The primitive cell in reciprocal space where the first Brillouin zone (BZ) is shaded in yellow. The high symmetry points are located at $\Gamma = (0,0)$, $K = \left(0, \frac{2\pi}{3a}\right)$, and $M = \left(\frac{2\pi}{\sqrt{3}a}, 0\right)$.....23

Figure 1.3. Graphene's electronic band structure approximation. Only the valence (π) and conductance (π^*) band is shown. The σ and σ^* bands are ignored due to not contributing many physical effects.....25

Figure 1.4. Zone-folding carbon nanotube (CNT) onto a graphene honeycomb lattice to determine the electronic property of A) metallic and B) semiconducting nanotubes. The red and green lines are cutting lines given by $\overrightarrow{K_1}$ and $\overrightarrow{K_2}$ allowed vectors of the CNT onto the graphene hexagonal lattice where the red line designates the splitting of density of states of the nanotube and the green lines are the neighboring allowed states.....28

Figure 1.5. Density of states general structure of a A) zero-dimensional quantum dot, B) one-dimensional quantum wire, C) two-dimensional quantum well, D) three-dimensional bulk semiconductor, E) metallic carbon nanotube, and F) semiconducting carbon nanotube.....30

Figure 1.6. Schematic representation of the elastic (Rayleigh) and inelastic (Stokes and Anti-Stokes) scattering of light where the incident photon laser energy is $\hbar\omega_i$.....32

Figure 1.7. Raman scattering spectroscopy of carbon nanotubes. A) Raman spectrum of pristine semiconducting single-walled carbon nanotubes (SWCNTs) bundles using a 532 nm Raman laser. B) The vibrational observation found in the radial direction along the nanotube's axis producing the radial-breathing mode (RBM) Raman scattering. C) The vibrational observation found along the nanotube circumferential direction producing the G_- Raman scattering. D) The vibrational observation found along the nanotube axis producing the G_+ Raman scattering.....34

Figure 1.8. Schematic representation of A) metallic and B) semiconducting carbon nanotube's optical transitions at the van Hove singularities.....35

Figure 1.9. UV/Vis/NIR spectrum of 0.014 mg/ml SWCNTs dispersed in aqueous solution using PEG and Triton-X 100.....36

Figure 1.10. Tunneling between two neighboring carbon nanotubes with applied voltage. E_F is the Fermi Level and λ is the barrier height for tunneling.....39

Chapter 2.

Figure 2.1. (a) Chemical structures of selectors presented in this study. (b) Schematic diagram of the sensing mechanism. (c) Normalized conductive change [$-\Delta G/G_0$ (%)] of the SWCNT-based sensor with trifunctional selector **1a** toward cyclohexanone at varying concentrations. The inset figure shows the magnitude of the normalized conductive change as a function of concentration of cyclohexanone.....45

Figure 2.2. Normalized average conductive change [$-\Delta G/G_0$ (%)] of SWCNT-based sensors with different selectors to 50 ppm cyclohexanone. The vertical error bars represent the standard deviation from the average based on three sensors exposed to 50 ppm cyclohexanone four times for 30 s.....48

Figure 2.3. (a) Plot of normalized average conductive change [$-\Delta G/G_0$ (%)] of SWCNT-based sensors with or without trifunctional selector **1a**. The sensors were exposed to various analytes at 1% equilibrium vapor concentration. (b) The plot of normalized average conductive change [$-\Delta G/G_0$ (%)] of SWCNT-based sensors with different selectors to 50 ppm cyclohexanone before and after 11 h of heating at 80 °C under reduced vapor pressure.....51

Figure A2.1. SEM images of SWCNTs-based sensors: a) SWCNT functionalized with selector **2a**. b) SWCNT functionalized with selector **2b**. c) SWCNT functionalized with selector **1a**. d) SWCNT functionalized with selector **1b**. e) Pristine SWCNT.....59

Figure A2.2. Diagram of sensing measurement setup.....60

Figure A2.3. a) The plot of normalized average conductive change ($-\Delta G/G_0$ (%)) of three SWNCT-based sensors exposed four consecutive times to 50 ppm cyclohexanone for 30 sec and allowed to recover for 30 s before and after 17 h of heating at 100 °C under reduced pressure. b) The plot shows normalized average conductive change ($-\Delta G/G_0$ (%)) of three SWNCT-based sensors exposed four consecutive times to 50 ppm cyclohexanone for 30 s and allowed to recover for 30 s before and after sonication in methanol. An Asterisk (*) denotes devices that no longer display a detectable conductance after sonication.....61

Figure A2.4. a) The plot shows normalized average resistive change ($-\Delta R/R_0$ (%)) of six SWNCT-based sensors with or without selector 1a after prolonged exposure to various humid conditions. b) The plot shows normalized average conductive change ($-\Delta G/G_0$ (%)) of six SWNCT-based sensors with selector 1a simultaneously exposed four consecutive times to 50 ppm cyclohexanone for 30 s and allowed to recover for 1 min at various humidity levels.....61

Figure A2.5. Calibration curve of sensors simultaneously exposed to various concentrations of cyclohexanone four consecutive times for 30 s and allowed to recover for 1 min.....63

Figure A2.6. ^{1}H NMR spectrum of 1-(3,5-bis(trifluoromethyl)phenyl)-3-(3-(triethoxysilyl)propyl)thiourea (d^6-DMSO).....69

Figure A2.7. ^{19}F NMR spectrum of 1-(3,5-bis(trifluoromethyl)phenyl)-3-(3-(triethoxysilyl)propyl)thiourea (d^6-DMSO).....70

Figure A2.8. ^{13}C NMR spectrum of 1-(3,5-bis(trifluoromethyl)phenyl)-3-(3-(triethoxysilyl)propyl)thiourea (d^6-DMSO).....71

Figure A2.9. ^{1}H NMR spectrum of 1-(3,5-bis(trifluoromethyl)phenyl)-3-propylthiourea (d^6-DMSO)).....72

Figure A2.10. ^{19}F NMR spectrum of 1-(3,5-bis(trifluoromethyl)phenyl)-3-propylthiourea (d^6-DMSO).).....73

Figure A2.11. ^{13}C NMR spectrum of 1-(3,5-bis(trifluoromethyl)phenyl)-3-propylthiourea (d^6-DMSO).....74

Figure A2.12. ^{1}H NMR spectrum of 3-(3,5-bis(trifluoromethyl)phenyl)-1,1-dimethylthiourea (d^6-DMSO).....75

Figure A2.13. ^{19}F NMR spectrum of 3-(3,5-bis(trifluoromethyl)phenyl)-1,1-dimethylthiourea (d^6-DMSO).....76

Figure A2.14. ^{13}C NMR spectrum of 3-(3,5-bis(trifluoromethyl)phenyl)-1,1-dimethylthiourea (d^6-DMSO).....77

Figure A2.15. ^{1}H NMR spectrum of 1-(3,5-bis(trifluoromethyl)phenyl)-1,3,3-trimethylthiourea (d^6-DMSO).....78

Figure A2.16. ^{19}F NMR spectrum of 1-(3,5-bis(trifluoromethyl)phenyl)-1,3,3-trimethylthiourea (d^6-DMSO).....79

Figure A2.17. ^{13}C NMR spectrum of 1-(3,5-bis(trifluoromethyl)phenyl)-1,3,3-trimethylthiourea (d^6-DMSO).....80

Figure A2.18. ^{1}H NMR spectrum of 1-isothiocyanatopyrene (d^6-$CDCl_3$).).....81

Figure A2.19. ^{13}C NMR spectrum of 1-isothiocyanatopyrene (d^6-$CDCl_3$).).....82

Figure A2.20. ^{1}H NMR spectrum of 1-(pyren-1-yl)-3-(3-(triethoxysilyl)propyl)thiourea (d^6-DMSO).....83

Figure A2.21. ^{13}C NMR spectrum of 1-(pyren-1-yl)-3-(3-(triethoxysilyl)propyl)thiourea (d^6-DMSO).....84

Figure A2.22. ^{1}H NMR spectrum of 1-propyl-3-(pyren-1-yl)thiourea (d^6-DMSO).....85

Figure A2.23. ^{13}C NMR spectrum of 1-propyl-3-(pyren-1-yl)thiourea (d^6-DMSO).....86

Chapter 3.

Figure 3.1. Fabrication of chemiresistive chemical sensors by drawing. Sensing materials (SWCNT-based) and graphite as electrodes were both deposited by mechanical abrasion to yield fully-drawn, chemiresistive gas-sensors on various A) unmodified substrates such as adhesive tape and unpolished silicon wafer, and B) laser-etched substrates such as PMMA and weighing paper. C) Fabrication of the sensing material consists of mechanically mixing and compressing SWCNT composites into a pellet. D) Stepwise fabrication of fully-drawn chemiresistive sensors on PMMA.....90

Figure 3.2. Mechanical deposition of sensing materials on six different substrates. A) Comparison of changes in conductance of sensing materials deposited on six different substrates in response to five consecutive exposures to 50 ppm pyridine. B–C) The average normalized conductance response (first exposure exempt) of at least six sensors on each substrate upon five consecutive exposures to various concentrations of pyridine for 30 s with 60 s recovery time....93

Figure 3.3. Comparison of device performance between fully-drawn sensors (SWCNT: TEC (1 : 2 wt. ratio) deposited by DRAFT and carbon-based electrodes deposited by mechanical abrasion) verses partially-drawn sensors (SWCNT : TEC (1 : 2 wt. ratio) deposited by DRAFT and gold electrodes deposited by thermal evaporation). A–D) Average normalized conductive response (first exposure exempt) of at least four fully-drawn sensors (black squares) and partially drawn sensors (white triangles) simultaneously exposed to various concentrations of pyridine for 30 s with 60 s recovery time. Inset: normalized conductance over time of seven fully-drawn and seven partially-drawn devices.....96

Figure 3.4. Fully-drawn sensor array. A) Schematic diagram of the selector's chemical structure used in the sensor array. L represents selectors that are liquids (Bp > 200 °C) and S represents selectors that are solids at room temperature prior to mixing with SWCNTs. The selectors were mixed with pristine SWCNTs mechanically and compressed into a pellet to make PENCILs. B) Average normalized conductive response (first exposure exempt) to simultaneous exposure to various gas analytes at ppm concentrations 5 consecutive times for 30 s with a 60 s recovery time. The PENCILs were deposited by DRAFT on weighing paper and the carbon-based electrodes (with 1 mm gap size) were deposited by abrasion using graphite pencil on the etched surface of weighing paper. C) Principal Component Analysis (PCA) plot discriminates between various gas analytes from the average conductive responses (first exposure exempt) of the sensor array.....98

Figure A3.1. A stepwise procedure for the fabrication of partially-drawn SWCNT-based chemiresistive sensors on laser-etched glass. Step 1 involves laser etching of glass to define regions onto which the sensing material will be deposited. Step 2 involves deposition of gold electrodes on the surface of glass by thermal evaporation. Step 3 involves bridging the gap between the gold electrodes by depositing a film of SWCNTs by mechanical abrasion into etched regions of glass.....110

Figure A3.2. Sensing response of Pristine SWCNTs devices deposited by abrasion onto various substrates using gold electrodes (0.3 mm gap size). a) Normalized change of conductance over

time from devices simultaneously exposed four consecutive times to 50 ppm pyridine for 30 s with recovery time of 60 s. b) Normalized average conductive responses (first exposure exempt) of at least three sensors simultaneously exposed four consecutive times to 50 ppm pyridine for 30 s with recovery time of 60 s.....111

Figure A3.3. Characterization of abraded films of sensing materials using high resolution Scanning Electron Microscopy (SEM). a-e) Images of compressed pristine SWCNTs deposited by abrasion between and on top of gold electrodes onto alumina, PMMA, weighing paper, adhesive tape, and glass, respectively.....112

Figure A3.4. Characterization of abraded films of sensing materials using high resolution Scanning Electron Microscopy (SEM). a-c) Images of compressed pristine SWCNTs deposited by abrasion between and on top of gold electrodes onto chemically etched glass, and laser etched glass/PMMA.....113

Figure A3.5. Investigation of the effect of ball milling on performance of SWCNTs as chemical sensing materials. Normalized average conductive responses of three pristine SWCNT-based sensors on weighing paper with gold electrodes simultaneously exposed four consecutive times to 50 ppm pyridine (first exposure exempt) for 30 s with recovery time of 60 s.....114

Figure A3.6. SWCNT and TEC was mechanically mixed at different mass ratios, compressed, and deposited between and on top of gold electrodes onto weighing paper (0.3 mm gap size). Normalized average conductive responses of two sensors simultaneously exposed four consecutive times to 50 ppm pyridine (first exposure exempt) for 30 s with a recovery time of 60 s.....115

Figure A3.7. Stability of PENCILs. SWCNT and TEC (2:1 mass ratio) was mechanically mixed and deposited between and on top of gold electrodes onto weighing paper. Normalized average conductive responses of at least two sensors simultaneously exposed at least four consecutive times to 50 ppm pyridine (first exposure exempt) for 30 s with a recovery time of 60 s.....116

Figure A3.8. Investigation of the SWCNT-based chemiresistor's sensitivity on various unmodified substrates. Normalized change of conductance over time from devices simultaneously exposed five consecutive times to 1 ppm pyridine for 30 s with a recovery time of 60s. Devices were fabricated by depositing SWCNT:TEC (2:1 mass ratio) on top of and between gold electrodes by abrasion onto various substrates.....117

Figure A3.9. Comparison study of SWCNT-based chemiresistor's sensitivity on various modified or unmodified substrates. Normalized change of conductance over time of devices simultaneously exposed five consecutive times to 1 ppm (a) and 50 ppm (b) pyridine for 30 s with recovery time of 60s. The devices were fabricated by depositing SWCNT:TEC (2:1 mass ratio) on top of and between gold electrodes by abrasion onto various modified and unmodified substrates.....119

Figure A3.10. Sensing response of SWCNTs-TEC (2:1 wt. ratio) deposited by abrasion on various substrates between gold electrodes (1 mm gap size). a) Normalized average conductive responses (first exposure exempt) of at least six sensors simultaneously exposed five consecutive

times to various concentrations of pyridine for 30 s with recovery time of 60 s. b) Substrate effects on the sensory performance was further investigated by analyzing the normalized average conductive responses (first exposure exempt) upon exposure to 550 ppm pyridine.....120

Figure A3.11. Sensing response of chemiresistor array fabricated on adhesive tape. The devices were fabricated by depositing SWCNT:Selector mixtures on top of and between gold electrodes by abrasion onto adhesive tape. a) Schematic diagram of the chemical structures of selectors used in the array. b) Normalized average conductive response (first exposure exempt) of three devices simultaneously exposed five consecutive times to various VOCs for 30 s with a recovery time of 60s.....121

Figure A3.12. Comparison of sensing responses from graphite and pristine SWCNTs deposited on the surface of weighing paper between gold electrodes. Resistance range of the sensors was between 1-2 kΩ. Normalized change of conductance over time for three devices simultaneously exposed four consecutive times to various analytes for 30 s with a recovery time of 60 s.....122

Figure A3.13. Normalized average conductive response (first exposure exempt) of at least four devices simultaneously exposed five consecutive times to various concentrations of pyridine for 30 s with recovery time of 60s. The devices were fabricated by depositing SWCNT:TEC (2:1 mass ratio) between carbon-based electrodes or gold electrodes by abrasion onto weighing paper. The carbon-based electrodes were fabricated by depositing graphite by abrasion on weighing paper.....123

Figure A3.14. User-to-user reproducibility for fully-drawn carbon-based chemiresistors. Normalized change of conductance over time of 2 devices from user 1 and 5 devices from user 2 simultaneously exposed five consecutive times to 1 and 550 ppm pyridine for 30 s with a recovery time of 60s. The devices were fabricated by depositing SWCNT:TEC (1:1 mass ratio) between carbon-based electrodes. The carbon-based electrodes were fabricated by depositing graphite by abrasion onto laser-etched PMMA.....125

Figure A3.15. Sensing response traces of four fully drawn devices on various substrates. Normalized change of conductance over time for three devices simultaneously exposed five consecutive times to various concentrations of pyridine for 30 s with recovery time of 60s. The devices were fabricated by depositing SWCNTs-TEC (2:1 wt. ratio) as the sensing material and graphite as the electrode by abrasion on various modified (PMMA and weighing paper) and unmodified (adhesive tape and silicon wafer) substrates.....126

Figure A3.16. Discrimination of pyridine threshold value limit (1_ppm). Average normalized conductive response (first exposure exempt) of at least four sensors simultaneously exposed to 1 ppm and 20 ppm of pyridine for 30 s with 60 s recovery time. SWCT:TEC (1:2 wt. ratio) pellet was deposited by mechanical abrasion between carbon-based on non-etched substrates (adhesive tape and silicon wafer) and laser etched substrates (weighing paper and PMMA).....127

Figure A3.17. Investigation of sensing material's level of saturation towards pyridine vapor. PENCILs were deposited onto the surface of weighing paper between gold electrodes by abrasion. Resistance range of the sensors was between 100-200 kΩ. Normalized change of

conductance over time for three devices simultaneously exposed 2 consecutive times to 50 ppm pyridine for 30 min with recovery time of 30 min.....129

Chapter 4.

Figure 4.1. Single-walled carbon nanotube (SWCNT) based chemiresistive response towards anions. Plot displays sensory response traces over a period of time for pristine SWCNT and SWCNT:PTES (50 : 0.025 m/v ratio) exposed simultaneously to A) 4ppm F^- and B) 200 ppb CN^- four consecutive times for 5 min with a 10 min recovery rate.....137

Figure 4.2. Single-walled carbon nanotube (SWCNT) mixed with various selectors chemiresistive response towards anions. Plot displays sensory response traces over a period of time for pristine SWCNTs, SWCNT:PTES (50 : 0.025 m/v ratio), SWCNT: Thiourea-Selector (50 : 0.25 m/v ratio), and SWCNT:Salicylaldehyde-selector:PTES (50 : 50 : 0.025 m/m/v ratio) mixtures exposed to A) 4 ppm F^- and B) 200 ppb CN^- four consecutive times for 5 min with a 10 min recovery rate. The sensory performance of SWCNT:Salicylaldehyde-selector:PTES mixture is shown in response towards C) 4ppm F^- and D) 200 ppb CN^- exposures.....139

Figure 4.3. Bar graph of average chemiresistive array responses of two devices simultaneously exposed one time for 5 min to 4 ppm of various anions (F^-, CN^-, $H_2PO_4^-$, and Cl^-). The red, blue, and green bars correlates to fabricated sensors using pristine SWCNTs, SWCNT:PTES (50 : 0.025 m/v ratio), and SWCNT:Salicylaldehyde-selector:PTES (50 : 50 : 0.025 m/m/v ratio) mixtures, respectively.....141

Figure A4.1. Image of PENCILs drawn between and on top of gold electrodes with 0.3 mm gap size on chemically-etched glass by DRAFT method.....148

Figure A4.2. Recovery kinetics of SWCNT:PTES exposure to 4 ppm F^- for 5 min.....148

Figure A4.3. Sensory response traces over a period of time for pristine SWCNT and mixtures of Thiourea-selector derivatives simultaneously exposed to 4 ppm F^- four consecutive times for 5 min with a 10 min recovery time. PENCILs were drawn between and on top of gold electrodes with 0.3 mm gap size on chemically-etched glass.....149

List of Schemes

Chapter 2.

Scheme 2.1. Thiourea-selector's enhanced dipole interactions with cyclohexanone.....47

Chapter 4.

Scheme 4.1. Proposed mechanism for CN^- detection using the Salicylaldehyde-selector.....140

List of Tables

Chapter 3.

Table A3.1. Device-to-device variance of chemiresistive material on 6 different substrates. Normalized average conductive response to 50 ppm pyridine 5 consecutive times for 30 s with recovery time of 60 s. Devices were fabricated by depositing SWCNT:TEC (2:1 mass ratio) on top on and between gold electrodes onto glass, adhesive tape, alumina, weighing paper, PMMA, or silicon.....118

Table A3.2. Parameters used in laser-etching.....124

Table A3.3. Resistive measurements of carbon-based electrodes used for chemiresitive sensors. Resistance ranges were derived from at least 2 drawn conductive lines. Functionalized SWCNTs with graphite electrodes (drawn within this range or below) had similar sensory performance as functionalized SWCNTs with gold electrodes.....124

Table A3.4. Device-to-device variance of fully-drawn sensors on 4 different substrates. Normalized average conductive response to 50 ppm pyridine 5 consecutive times for 30 s with recovery time of 60 s. Devices were fabricated by depositing SWCNT:TEC (2:1 mass ratio) between graphite electrodes onto silicon, adhesive tape, and laser-etch substrates (weighing paper and PMMA).....128

Table A3.5. Average Sensory Response of Array.....130

Table A3.6. Principle Component Scores.....130

Table A3.7. Principle Component Coefficient.....131

Table A3.8. Hotelling's T^2 Statistic.....131

Table A3.9. Principal Component Eigenvalues.....132

Table A3.10. Percentage of the Total Variance.....132

Chapter 1

Introduction Of Carbon Nanotube's Structural, Electronic, Spectroscopic, and Sensory Properties

1.1 Introduction to Carbon Materials

The arrangement of electrons around the nucleus of the carbon atom results in various physical properties of the carbon material. The carbon atom has six electrons shared evenly between the 1s, 2s, and 2p orbitals where there are four valence electrons (one 2s and three in 2p). Carbon materials are made up of carbon-carbon (C-C) covalent bonds formed by 2s orbitals hybridizing with one or more 2p orbitals. Three allotropic forms of carbon exist in the solid phase: diamond, graphitic materials (graphite, carbon nanotubes, and graphene), and buckministerfullerenes/fullerenes. Diamond (hardest substance known[1]) has sp^3-hybridized carbons where each carbon atom is bonded with four other carbon atoms in a tetrahedral arrangement. Graphite has sp^2-hybridized carbons with a hexagonal lattice where each carbon atom is bonded to only three other carbon atoms. The electrons can move freely through states composed of pure p-orbitals, thus forming an endless delocalized π-bonded network to make graphite electrically conductive. Buckminsterfullerenes or fullerenes are in the family of spherical or cylindrical carbon molecules with sp^2-hybridization. The properties of nanotubes will be the focus of this chapter.

Ijima first demonstrated the synthesis of and characterization of carbon nanotubes (CNTs) in the 1990s.[2] Since their discovery, CNT research has developed into the leading area in nanotechnology producing thousands of publications per year.[3] CNTs can be synthesized using various methods such as arc-discharge, high-pressure carbon monoxide conversion (HiPCO), laser ablation, chemical vapor deposition (CVD), and in flames with restricted oxygen.[1]

1.2 Structural Properties of Carbon Nanotubes

There are three different layer-dependent types of nanotubes: single-walled carbon nanotubes (SWCNTs), double-walled carbon nanotubes (DWCNTs) and multi-walled carbon nanotubes (MWCNTs). The nanotube structure is essentially sp^2-hybridization carbon sheet(s), with a hexagonal honeycomb lattice, rolled into a hollow cylindrical tube. The wall-to-wall spacing between layers are in the same range as the interlayer distance of graphite (3.41 Å).[4] SWCNTs are interesting materials due to their small structure of 10-40 carbon atoms along the circumference (typical diameter ~1.4 nm)[5] with a μm long tube length along the cylinder axis[6], one atom thick layer (the entire surface area susceptible to environmental changes), high surface area (the theoretical surface area of 1315 m^2g^{-1})[7], quasi-one-dimensional electron confinement, and high electrical and thermal conductivity (the thermal conductivity of nearly 3500 W/mK at room temperature for a 2.6 μm length and 1.7 nm diameter SWCNT).[8]

Figure 1.1 shows a graphene sheet, with a hexagonal lattice of carbon atoms, where the unit cell (*KFF'V*) is spanned by two real space basis vectors $\overrightarrow{a_1}$ and $\overrightarrow{a_2}$. SWCNT's structural and electronic properties can be characterized by the direction of rolling the tube, which is known as chirality. Equation 1 describes the circumferential vector ($\overrightarrow{KV}$) or chiral vector ($\overrightarrow{C_h}$) that forms along the cylinder axis,

$$\overrightarrow{C_h} = n\,\overrightarrow{a_1} + m\,\overrightarrow{a_2} = (n, m) \tag{1}$$

where n and m are integers. The chiral index (n, m) used to determine the chiral angle (θ) is expressed as

$$\theta = \tan^{-1}\left[\sqrt{3}\left(m/(2n + m)\right)\right]. \tag{2}$$

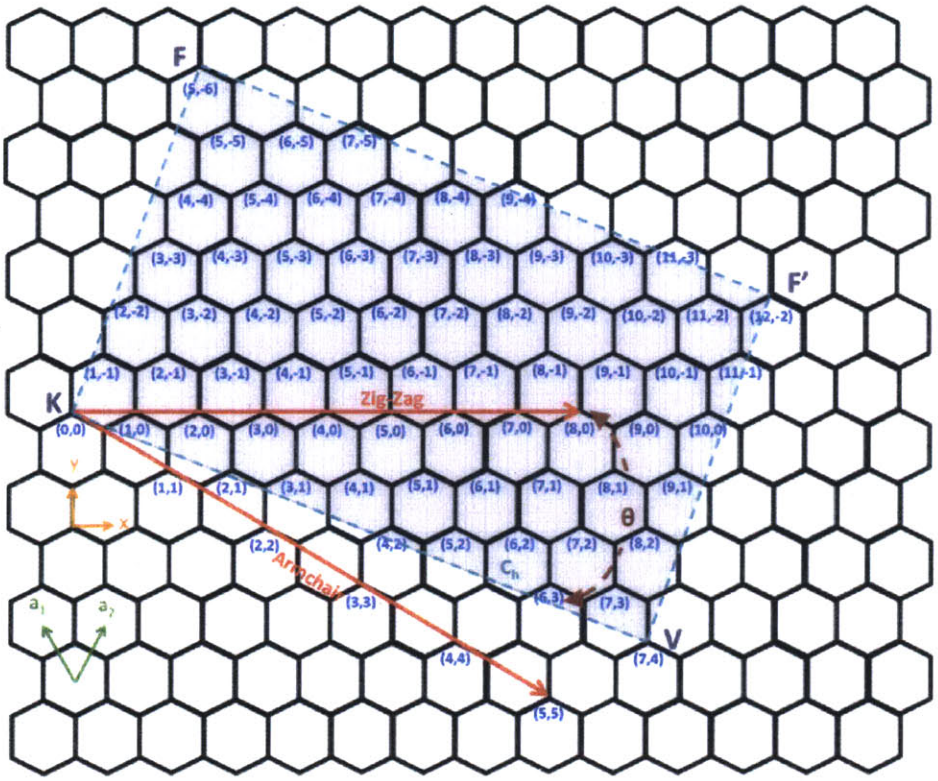

Figure 1.1. Labeled graphene sheet indicating the nanotube's structural and electronic properties. The chiral vector $\overrightarrow{KV} = \overrightarrow{C_h} = 7\overrightarrow{a_1} + 4\overrightarrow{a_2}$ of a (7,4) nanotube is defined on a honeycomb lattice of carbon atoms with unit vectors $\overrightarrow{a_1}$ and $\overrightarrow{a_2}$. The nanotube's diameter, chiral angle, translation vector, and electronic type (metallic or semiconductor) can be determined by the chiral indices.

Based on chirality, the nanotubes can be differentiated into the following three classes: armchair $[(n,n)$ where $n = m; \theta = 30°)$, zig-zag $[(n,0)$ where $m = 0$ and $n > 0; \theta = 0°]$, and chiral $[(n,m)$ where $0 < |m| < n; 0 < \theta < 30°)$. The nanotube's chirality and diameter directly influence its distinct electronic properties. Armchair CNTs are metallic, thus having zero band gap. Zig-zag CNTs are semiconductors where a band gap separates the valence (occupied states) and conduction band (unoccupied states). Chiral CNTs can either be metallic (if $n - m = 3x$, where x is an integer and $m \neq n$) or a semiconductor in all other cases. The nanotube's diameter (d_t) gives the chiral vector length expressed as

$$d_t = |\overrightarrow{C_h}| / \pi = \sqrt{3}\left[a_{C-C}\sqrt{(m^2 + mn + n^2)}/\pi\right] \quad (3)$$

where a_{C-C} is the C-C bond length (1.42 Å in graphite). It has been shown that d_t scales inversely to the semiconductive CNT's band gap.[1]

The structural properties discussed thus far only relates to the nanotube's circumferential direction. Along the nanotube's axis direction describes the translation vector ($\vec{T}$). In the hexagonal lattice, the translational vector $\vec{T}$ is perpendicular to $\overrightarrow{C_h}$ where $\overrightarrow{KF}$ is the shortest repeating distance along the nanotube's axis. The translation vector ($\vec{T}$) and translation vector magnitude ($|\vec{T}|$) can be expressed as

$$\vec{T} = t_1 \overrightarrow{a_1} + t_2 \overrightarrow{a_2} = (t_1, t_2) \quad (4)$$

$$|\vec{T}| = \frac{\sqrt{3} \times \overrightarrow{C_h}}{d_R} \quad (5)$$

where $t_1 = \frac{2m+n}{d_R}$, $t_2 = -\frac{2n+m}{d_R}$, and d_R is the greatest common divisor (gcd) of $(2n + m, 2m + n)$. $d_R = gcd$ if $n - m$ is not a multiple of $3(gcd)$ and $d_R = 3(gcd)$ if $n - m$ is a multiple of $3(\text{gcd})$. The final aspect of the nanotube in real space is the unit cell. The unit cell is made up of N honeycombs lattice where $N = \frac{2(m^2+n^2+nm)}{d_R}$.

CNT's structural properties can be described not only using the unit cell area but with the primitive cell area as well continually referencing the graphene honeycomb lattice (Figure 1.2). CNT primitive cell area is 1/N the unit cell, the same as graphene.[5] The primitive cell in reciprocal lattice space is known as the Brillouin zone (BZ). Figure 1.2B shows the first BZ of nanotubes with high-symmetry points Γ, K, M (center, corner, and center of the edge,

respectively). The real space basis vectors are expressed as $\overrightarrow{\boldsymbol{a_1}} = \left(\frac{\sqrt{3}a}{2}, \frac{a}{2}\right)$ and $\overrightarrow{\boldsymbol{a_2}} = \left(\frac{\sqrt{3}a}{2}, -\frac{a}{2}\right)$ where the real space bases vector length or lattice constant ($|\overrightarrow{\boldsymbol{a_1}}| = |\overrightarrow{\boldsymbol{a_2}}| = a = 1.42\text{Å} \times \sqrt{3} = 2.46\text{Å}$) forms an 60° angle. Configuring the direction of the reciprocal space basis vectors requires rotating the real space basis vectors 30°. The orientation of the graphene honeycomb lattice from Figure 1.2A to Figure 1.2B shows the unit cell to primitive cell rotation where the real basis vectors ($\overrightarrow{\boldsymbol{a_1}}$ and $\overrightarrow{\boldsymbol{a_2}}$) are now in reciprocal basis vectors ($\overrightarrow{\boldsymbol{b_1}}$ and $\overrightarrow{\boldsymbol{b_2}}$). The reciprocal lattice vectors is thus given by $\overrightarrow{\boldsymbol{b_1}} = \left(\frac{2\pi}{\sqrt{3}a}, \frac{2\pi}{a}\right)$ and $\overrightarrow{\boldsymbol{b_2}} = \left(\frac{2\pi}{\sqrt{3}a}, -\frac{2\pi}{a}\right)$ where the lattice constant is $4\pi/\sqrt{3}$ in reciprocal space.

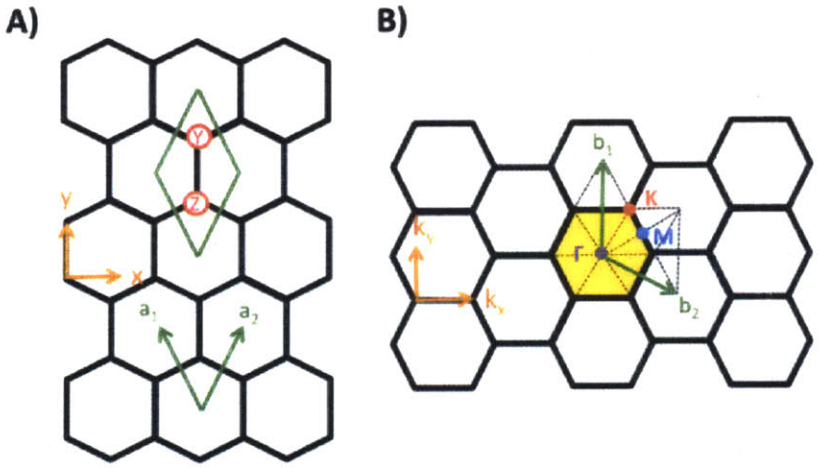

Figure 1.2. Graphene sheet in both real ($\overrightarrow{\boldsymbol{a_1}}$ and $\overrightarrow{\boldsymbol{a_2}}$) and reciprocal space ($\overrightarrow{\boldsymbol{b_1}}$ and $\overrightarrow{\boldsymbol{b_2}}$). A) The unit cell in real space where the honeycomb lattice contains two carbon atom sites Y and Z. B) The primitive cell in reciprocal space where the first Brillouin zone (BZ) is shaded in yellow. The high symmetry points are located at $\Gamma = (0,0)$, $K = \left(0, \frac{2\pi}{3a}\right)$, and $M = \left(\frac{2\pi}{\sqrt{3}a}, 0\right)$.

1.3 Electronic Properties

Pristine carbon nanotubes are made up of σ bonds located along the cylindrical wall forming hexagonal network with strong covalent bonds and π bonds pointed perpendicular to the nanotube's surface creating weak van-der-Waals interactions between tubes.[9] The π bonds are the most important aspect of the CNTs electronic properties because the bonding and anti-bonding π bands are close to the Fermi level.[9] The Fermi level is the chemical potential of electrons or highest occupied electron energy level at absolute zero temperature (0 K). The CNT's σ bonds are too far away from the Fermi level to influence the electronic transport in the visible energy range.[9] To calculate CNT's energy band structure, zone-folding combined with tight bonding technique yields accurate results for larger diameters nanotubes and electronic energies not far from the Fermi level. [9] The determination of the band structure of smaller diameter nanotubes will need additional parameters, such as curvature effects, to improve the accuracy of the calculations. The electronic band structure of graphene is generally used as a reference.

Figure 1.3 is a schematic diagram that shows the typical graphene electronic band structure of only valence (π) and conduction (π*) band. We are only approximating the energy dispersion based on the π and π* bands as a result of the fact that σ and σ* bands are not relatively close to the Fermi surface. Graphene's energy-dispersion ($E_k^{\pm}$) is graphed along the high symmetry points Γ- K-M and Γ- M where the Fermi level (E_F) is set at 0 V. An interesting feature shown in graphene's electronic band structure is that the π and π* band crosses at the K point of the BZ.[9] This presents an opportunity for the electrons to be excited from the π band to the π* band optically when located very close to the K point.[6] The optical transition has linear energy-dispersion relationship dependence, however this only occurs close to the K point (or E_F).

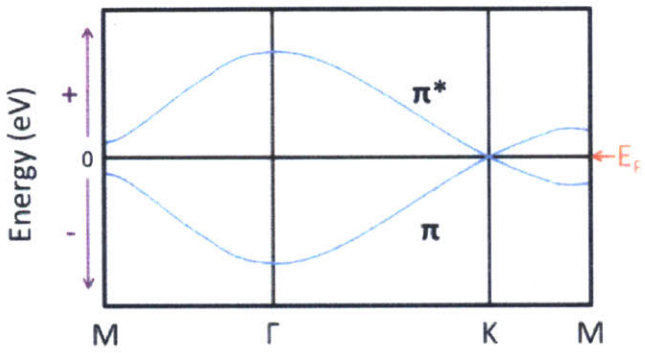

Figure 1.3. Graphene's electronic band structure approximation. Only the valence (π) and conductance (π^*) band is shown. The σ and σ^* bands are ignored due to not contributing many physical effects.

To calculate graphene's energy-dispersion relations, the tight-binding method requires that we first solve the time-independent Schrödinger's equation

$$H_k \Psi(\mathbf{k}) = E_k \Psi(\mathbf{k}) \tag{6}$$

where H_k is the Hamiltonian, E_k are the eigenvalues at wavevector $\mathbf{k}$, and $\Psi(\mathbf{k})$ are the eigenfunctions. $\Psi(\mathbf{k})$ is written as linear combinations of Bloch functions ($\phi_i(\boldsymbol{k})$).

$$\Psi(\mathbf{k}) = \sum_i c_i \, \phi_i(\boldsymbol{k}) \tag{7}$$

$\phi_i(\boldsymbol{k})$ expresses the electron in a periodic environment. Recall that the unit cell of graphene contains two carbon atoms (Figure 1.2A), therefore we can construct $\phi_i(\boldsymbol{k})$ for graphene sublattice Y and Z

$$\phi_Y = \frac{1}{\sqrt{N}} \sum_{\boldsymbol{R}_Y} e^{i\boldsymbol{k}\cdot\boldsymbol{R}_Y} \varphi(\boldsymbol{r} - \boldsymbol{R}_Y), \; \phi_Z = \frac{1}{\sqrt{N}} \sum_{\boldsymbol{R}_Z} e^{i\boldsymbol{k}\cdot\boldsymbol{R}_Z} \varphi(\boldsymbol{r} - \boldsymbol{R}_Z) \tag{8}$$

where N is the number of unit cells, $\boldsymbol{R}$ is the lattice vector and the sums run over all possible lattice vectors. To solve for the Schrödinger's equation (Equation 6), we multiply both sides by $\Psi(\mathbf{k})$.

$$\langle\Psi(\mathbf{k})|H_k|\Psi(\mathbf{k})\rangle = \langle\Psi(\phi_i\mathbf{k})|E_k|\Psi(\mathbf{k})\rangle \tag{9}$$

We find from simple subtraction that

$$\langle\Psi(\mathbf{k})|H_k|\Psi(\mathbf{k})\rangle - \langle\Psi(\mathbf{k})|E_k|\Psi(\mathbf{k})\rangle = 0 \tag{10}$$

$$\begin{bmatrix} H_{YY}(\boldsymbol{k}) - E(\boldsymbol{k})S_{YY}(\boldsymbol{k}) & H_{YZ}(\boldsymbol{k}) - E(\boldsymbol{k})S_{YZ}(\boldsymbol{k}) \\ H^*_{YZ}(\boldsymbol{k}) - E(\boldsymbol{k})S^*_{YZ}(\boldsymbol{k}) & H_{YY}(\boldsymbol{k}) - E(\boldsymbol{k})S_{YY}(\boldsymbol{k}) \end{bmatrix} = 0 \tag{11}$$

where H_{IJ} are matrix elements of the Hamiltonian and S_{IJ} are the overlaps between Bloch functions ($H_{IJ} = \langle\phi_I|H|\phi_J\rangle$, $S_{IJ} = \langle\phi_I|\phi_J\rangle$). Equation 11 can be simplified by neglecting the overlap between wavefunctions centered at different atoms ($S_{YY} = 1, S_{YZ} = 0$).

$$\begin{bmatrix} H_{YY}(\boldsymbol{k}) - E(\boldsymbol{k}) & H_{YZ}(\boldsymbol{k}) \\ H^*_{YZ}(\boldsymbol{k}) & H_{YY}(\boldsymbol{k}) - E(\boldsymbol{k}) \end{bmatrix} = 0 \tag{12}$$

The solution is determined by the determinant $det[H - ES] = 0$ vanishing to yield

$$E^{\pm}_{\boldsymbol{k}} = H_{YY}(\boldsymbol{k}) \mp |H_{YZ}(\boldsymbol{k})| \tag{13}$$

where $E^{+}_{\boldsymbol{k}}$ and $E^{-}_{\boldsymbol{k}}$ are the eigenvalues of the π and π^* band, respectively. This solution was found by Wallace in 1947 when he first derived the tight-binding band structure.[9] Since the π and π^* crosses at K point (at the Fermi level), therefore $E_F = H_{YY} - |H_{YZ}(\mathrm{K})| = H_{YY} + |H_{YZ}(\mathrm{K})| = 0$ or for nearest neighbors approximation

$$E^{\pm}_{\boldsymbol{k}} = \mp|H_{YZ}(\boldsymbol{k})| \tag{14}$$

where $H_{YZ}(\boldsymbol{k}) = \langle \phi_Y | H | \phi_Z \rangle = \frac{1}{N} \sum_{R_Y} \sum_{R_Z} e^{i\boldsymbol{k}\cdot(\boldsymbol{R_Z}-\boldsymbol{R_Y})} \langle \varphi_Y(\boldsymbol{r}-\boldsymbol{R_Y}) | H | \varphi_Z(\boldsymbol{r}-\boldsymbol{R_Z}) \rangle$. This tight-binding approximation is sufficient for CNTs when bands are very close to the K point.[9] The Hamiltonian ($H_{YZ}(\boldsymbol{k})$) for the two carbon atoms in the graphene unit cell can be expressed as

$$H_{YZ}(\boldsymbol{k}) = \begin{bmatrix} 0 & -\gamma_0 f(k) \\ -\gamma_0 f^{\dagger}(k) & 0 \end{bmatrix} \tag{15}$$

where $f(k) = e^{ik_x a/\sqrt{3}} + 2e^{-ik_x a/2\sqrt{3}} \cos(k_y a/2)$ and γ_0 is the nearest-neighbor C-C tight-binding overlap energy.[5] Note that only the π and π^* energy band is still only being considered. The energy-dispersion relations of two-dimensional graphite ($E_{g2D}^{\pm}$) can be determined by finding the eigenvalue solution $[det(H - EI) = 0]$.[5]

$$E_{g2D}^{\pm} = \pm\gamma_0 \sqrt{1 + 4cos\left(\frac{\sqrt{3}k_x a}{2}\right)\cos\left(\frac{k_y a}{2}\right) + 4cos^2\left(\frac{k_y a}{2}\right)} \tag{16}$$

Using tight-binding approximation, graphene's electronic band structure can be constructed. This information will be useful calculating the electronic properties of CNTs, however zone-folding is beneficial technique to be used in conjunction with tight-band approximation. CNT's one-dimensional BZ is much smaller than graphite's two-dimensional BZ, however the BZ is small and CNT's crystal structure is similar to graphene. Therefore, zone-folding of graphene's two-dimensional BZ is a suitable approximating technique.[6] Zone-folding or confinement approximation technique finds the nanotube's electronic band structure plotting CNT's allowed $\overrightarrow{\boldsymbol{K}}$ vector states along graphene's two-dimensional BZ

$$\overrightarrow{\boldsymbol{K_1}} = \frac{1}{N}\left(-t_2\overrightarrow{\boldsymbol{b_1}} + t_1\overrightarrow{\boldsymbol{b_2}}\right),\ \overrightarrow{\boldsymbol{K_2}} = \frac{1}{N}\left(m\overrightarrow{\boldsymbol{b_1}} - n\overrightarrow{\boldsymbol{b_2}}\right) \tag{17}$$

where $\overrightarrow{b_1}$ and $\overrightarrow{b_2}$ are reciprocal lattice vectors, $t_1 = \frac{2m+n}{d_R}$, $t_2 = -\frac{2n+m}{d_R}$, N is the number of honeycomb lattice in unit cell, n and m are integers. Figure 1.4 demonstrates zone-folding to characterize metallic and semiconducting CNTs. A series of parallel lines represent the CNT's allowed $\vec{K}$ vector states plotted onto the graphene's BZ where the parallel line's length, number, and orientation are depending on the nanotube's chirality (n, m). The separation and length of the cutting lines are given by $\overrightarrow{K_1}$ and $\overrightarrow{K_2}$, respectively.

$$|\overrightarrow{K_1}| = \frac{2}{d_t}, |\overrightarrow{K_2}| = \frac{2\pi}{|\vec{T}|} = \frac{2d_R}{\sqrt{3}d_t} \tag{18}$$

The $\overrightarrow{K_2}$ vector is found along the nanotube's axis ($\overrightarrow{C_h} \cdot \overrightarrow{K_2} = 0$, $\vec{T} \cdot \overrightarrow{K_2} = 2\pi$) and the $\overrightarrow{K_1}$ vector is found along the circumferential direction ($\overrightarrow{C_h} \cdot \overrightarrow{K_1} = 2\pi$, $\vec{T} \cdot \overrightarrow{K_1} = 0$). If the nanotube's allowed $\vec{K}$ vector states intersect at the graphene K point, then the nanotube is metallic where a non-zero density of states is located at the Fermi level (Figure 1.4A). However, there are no

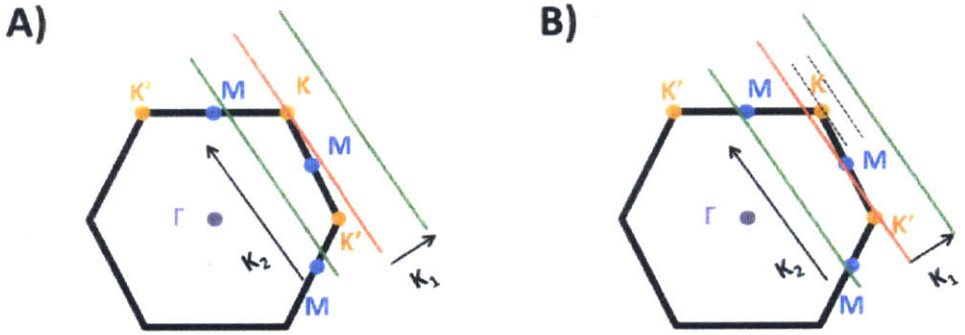

Figure 1.4. Zone-folding carbon nanotube (CNT) onto a graphene honeycomb lattice to determine the electronic property of A) metallic and B) semiconducting nanotubes. The red and green lines are cutting lines given by $\overrightarrow{K_1}$ and $\overrightarrow{K_2}$ allowed vectors of the CNT onto the graphene hexagonal lattice where the red line designates the splitting of density of states of the nanotube and the green lines are the neighboring allowed states.

allowed $\vec{K}$ vector states at the graphene K point for semiconducting CNTs where a moderate energy band gap is observed (Figure 1.4B). For semiconducting CNTs, the K point is located in a position one-third the distance between the two adjacent $\overrightarrow{K_1}$ lines. The general rule is that $3x = n - m$ are metallic nanotubes and $3x \neq n - m$ are semiconducting nanotubes where x is an integer.[5]

Using tight-binding approximation and zone-folding the SWCNT's one-dimensional energy-dispersion relations $[E_{\mu}^{\pm}(k)]$ is

$$E_{\mu}^{\pm}(k) = E_{g2D}^{\pm}\left(k\frac{\overrightarrow{K_2}}{|\overrightarrow{K_2}|} + \mu\overrightarrow{K_1}\right) \tag{19}$$

where $E_{g2D}^{\pm}$ is the energy dispersion relation of two-dimensional graphite, $-\pi/|\vec{T}| < k < \pi/|\vec{T}|$ is the one-dimensional wavevector along the nanotube axis, $\mu = 1, \ldots, N$, and N is the number of honeycomb lattice in the unit cell.[5] Electrons in the nanotube's lattice are under periodic boundary conditions along the circumferential direction, which will yield N discrete k values. The number of available electrons for a given energy level is known as the density of states (DOS) shown in Figure 1.5. The DOS is highly dependent on the system's electronic confinement shown in Figure 1.5A-D. The DOS have the following forms: zero-dimensional features are series of delta functions; one-dimensional features are series of inverse square root functions; two-dimensional features are series of step functions; and three-dimensional features with a parabolic function form. Since CNTs are one-dimensional materials, their DOS will take the form of $1/\sqrt{E}$ (Figure 1.5B). The sharp peaks observed are called van Hove singularities.[9] The red highlighted line in the DOS is located at the Fermi level (Figure 1.5E), thus indicating the presence of DOS at the Fermi level (K point) for metallic nanotubes. In Figure 1.5F, we

alternatively observe a band gap at the Fermi level instead for semiconducting CNTs. The one-dimensional DOS in units of states/C-atom/eV is calculated by

$$D(E) = \frac{|\vec{T}|}{2\pi N} \sum_{\pm} \sum_{\mu=1}^{N} \int \frac{1}{\left|\frac{dE_{\mu}^{\pm}(k)}{dk}\right|} \delta\left(E_{\mu}^{\pm}(\boldsymbol{k}) - E\right) dE \tag{20}$$

where the summation is taken for the N conduction (+) and valence (-) bands.[5]

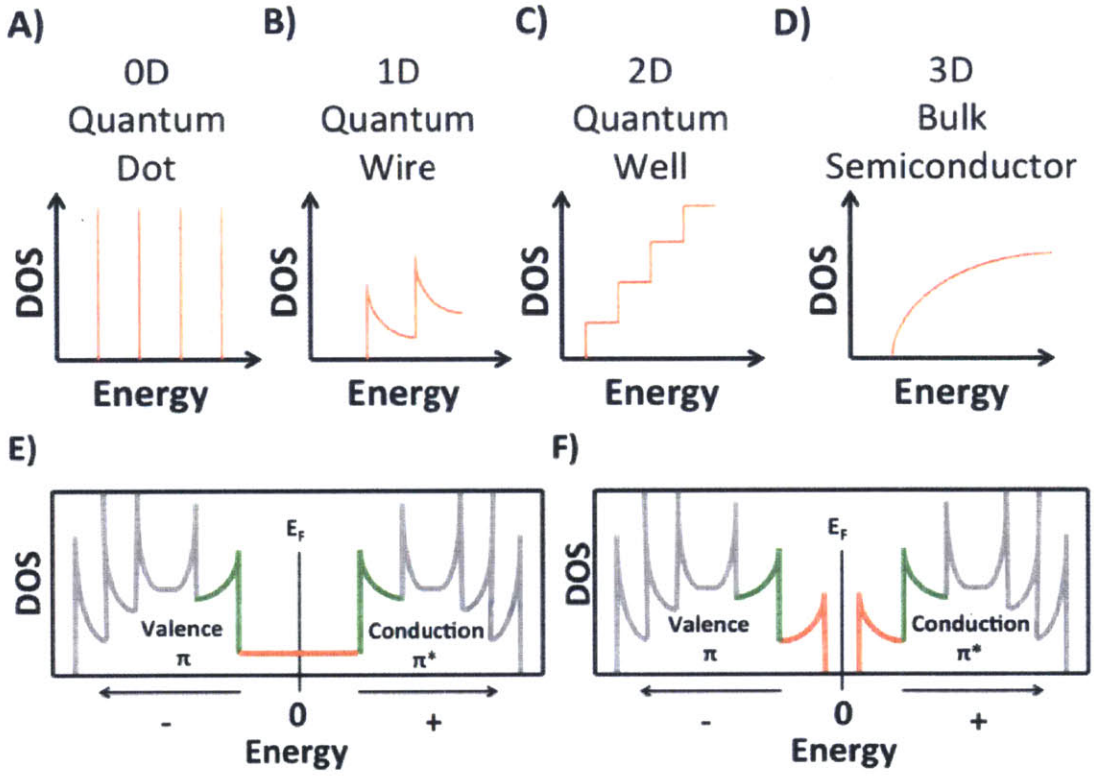

Figure 1.5. Density of states general structure of a A) zero-dimensional quantum dot, B) one-dimensional quantum wire, C) two-dimensional quantum well, D) three-dimensional bulk semiconductor, E) metallic carbon nanotube, and F) semiconducting carbon nanotube.

1.4 Spectroscopic characterization of Single-walled Carbon Nanotubes

1.4.1 Raman Spectroscopy

One of the most common spectroscopic equipment for characterizing SWCNTs is the Raman spectrometer due to its high sensitivity and nondestructive/noncontact nanotube characterization tool.[10] Figure 1.6 displays the different type of scattering. An elastic scattering of light is called Rayleigh scattering where the kinetic energy of the incident light scattering is unmodified during the interaction with other molecules. Raman scattering spectroscopy is the inelastic scattering of light where a monochromic laser in the visible or near infrared range is inelastically scattered and excites a vibration as determined by a shift in the laser photon energy. When the incident light is shifted to a lower frequency (lower energy), the scattered light is called Stokes-shift scattering. In this process, the energy transferred to the vibrational mode of the molecule is elevated to a higher vibrational energy state. Likewise, when the incident light shifted to a higher frequency (higher energy), the scattered light is a called anti-Stokes-shift scattering. In this process, the vibrationally excited molecule is transferred to a lower vibration state after scattering. There is a higher population of electrons in the lowest vibration state at room temperature; therefore the Raman scattering signal intensity is higher for Stokes-shift scattering at room temperature. The incident light excites a molecule from the ground vibration state to a virtual state. The virtual state is a very short-lived quantum state that does not correspond to a real energy level.

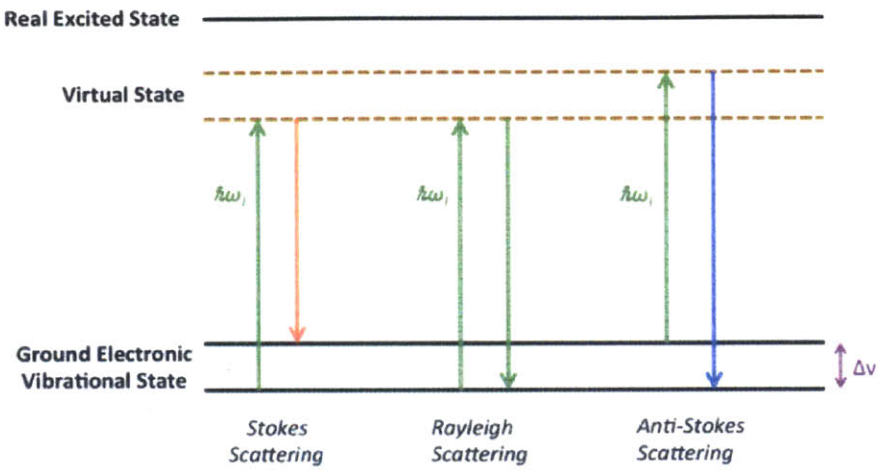

Figure 1.6. Schematic representation of the elastic (Rayleigh) and inelastic (Stokes and Anti-Stokes) scattering of light where the incident photon laser energy is $\hbar\omega_i$.

The Raman spectrometer high sensitivity towards CNTs are due to resonance where the applied laser wavelength matches the optical transition of certain nanotube structures generating high Raman scattering intensity. The closer the virtual state is to the real excited state, the higher the probability of scattering. The Raman intensity can be expressed as

$$I \sim |\boldsymbol{e}_s \cdot \Re \cdot \boldsymbol{e}_i| \tag{21}$$

where $\Re$ is the Raman tensor (symmetry matrix of corresponding phonon), and $\boldsymbol{e}_i$ and $\boldsymbol{e}_s$ are polarization vectors of the incident and scattering light, respectively.[11] Figure 1.7A shows a Raman spectrum of semiconducting SWCNT bundles. The spectrum has various Raman features such as radial-breathing mode, D-band, G-band, and G'-band of carbon nanotubes.

The radial-breathing-mode (RBM) is a unique phonon symmetric vibrational mode that appears only for carbon nanotubes in the Raman frequency range (ω_{RBM}) 100-500 cm^{-1}.[5] The RBM is a bond-stretching out-of-plane phonon mode where all carbons move coherently as depicted in Figure 1.7B. The RBM frequency is inversely proportional to the tube diameter

($\omega_{RBM} \propto {}^{1}/_{d_t}$) where this dependence is derived from the mass of all carbon atoms along the circumferential direction proportional to the nanotube diameter.[6] Thus, the Raman spectra determines the tube diameter where accuracy increases with decreasing diameter (1 Å accuracy for a 5.0 nm diameter).[10] However, larger-diameter tubes have broader RBM line widths resulting in decrease of accurateness.

The tangential mode (G-band) found between Raman frequency 1500-1600 cm^{-1} is associated with highest-frequency optical phonon modes at the Γ-point of BZ.[10] The G-band has two strong peaks, G_- (Figure 1.7C) and G_+ (Figure 1.7D), which relates to carbons along the circumferential (TO phonon) and axial (LO phonon) direction vibrations, respectively. The G-band peaks splitting depend on the nanotube curvature and the intensity depends on the chiral angle. Thus, the G-band is can identify the nanotube's electronic properties where semiconducting nanotubes G-band peaks have a Lorentzian line shape (Figure 1.7A) while metallic nanotubes G-band peaks are broader having a Breit-Wigner-Fano (BWF) line shape (asymmetric).[5] Semiconducting nanotube's circumferential mode has a lower Raman G_- frequency (ω_G^-) compared to the axial mode Raman frequency (ω_G^+) and the opposite is true for metallic nanotubes.

The disorder-induced D-band that is found near Raman frequency 1350 cm^{-1} provides the nanotube or graphite defect density (disorder of the hexagonal sp^2-hybridization lattice). The D-band originates from the phonons close to the K point of graphite. This scattering behavior occurs when an electron is excited into a virtual state, scatters by a phonon (or defect) with wavevector $\vec{q}$ and scatters back by a defect (or phonon) with wavevector $-\vec{q}$ to recombine with the virtual hole emitting a scattered photon.[10] A quantitative analysis of the nanotube defect

density is typically based on the D-band and G-band intensity ratio (I_D/I_G). The overtone of the D-band (G'-band) is found near the Raman frequency 2600 cm^{-1}.

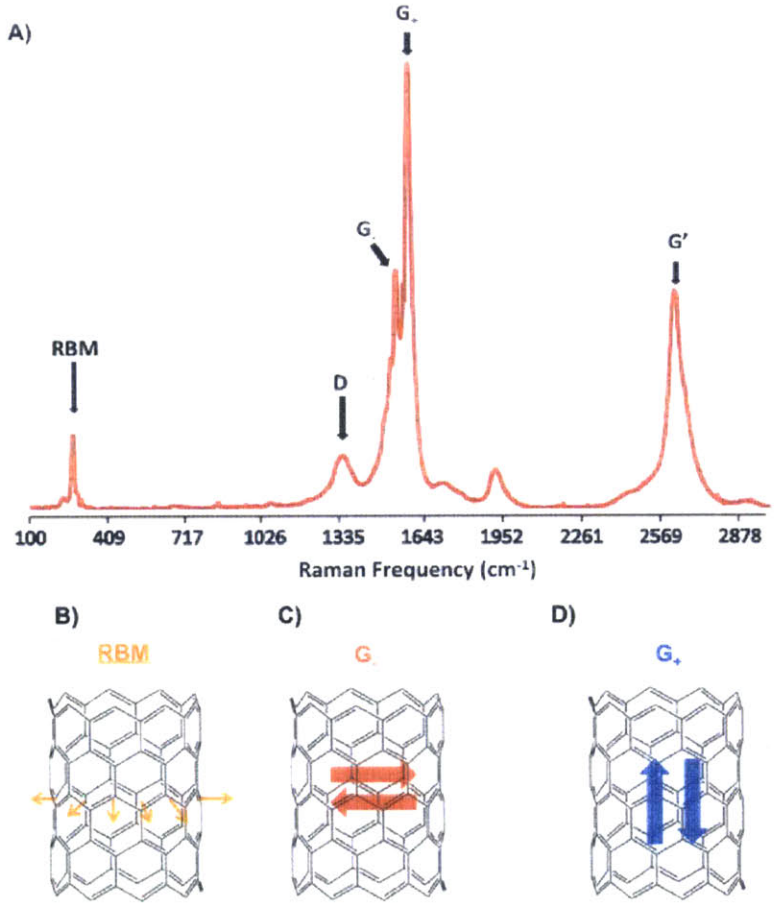

Figure 1.7. Raman scattering spectroscopy of carbon nanotubes. A) Raman spectrum of pristine semiconducting single-walled carbon nanotubes (SWCNTs) bundles using a 532 nm Raman laser. B) The vibrational observation found in the radial direction along the nanotube's axis producing the radial-breathing mode (RBM) Raman scattering. C) The vibrational observation found along the nanotube circumferential direction producing the G- Raman scattering. D) The vibrational observation found along the nanotube axis producing the G_+ Raman scattering.

1.4.2 Absorption Spectroscopy

Recall from the previous section that the DOS of carbon nanotubes are the shape of van Hove singularities (energy levels with significant high density of states), thus the optical transition occurs between the singularities near the Fermi level. If the energy of incoming light matches the transition (E_{ii}) between a singularity in the valence (V_i) and conduction (C_i) band, then there is a high probability of strong optical absorption. Figure 1.8 demonstrates the optical transitions between singularities with respect to the DOS for metallic (M_{ii}) and semiconducting (S_{ii}) nanotubes near the Fermi level (K point). Detecting the optical transition of SWCNTs reveals the nanotube's general structural and electronic properties. In 2002, Richard Smalley and his team discovered that the optical properties of nanotubes could be measured in transmission mode from a dispersed solution (via ultrasonication) of nanotubes aided with a surfactant physisorbed to stabilize the solution. [12] Prior to this discovery, nanotubes were not separated due to the strong van der Waals' attraction where the bundle perturbs the electronic structure of the nanotubes.

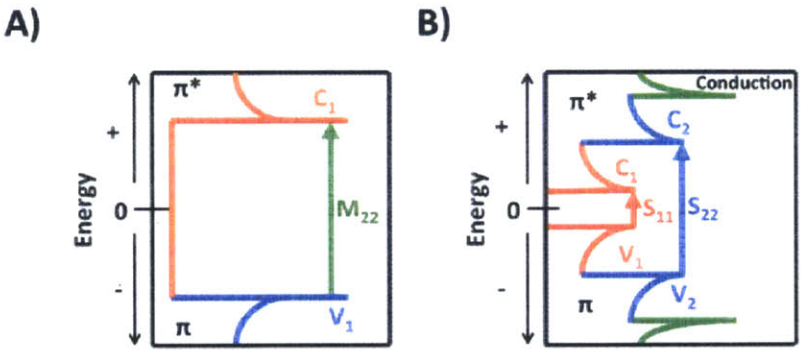

Figure 1.8. Schematic representation of A) metallic and B) semiconducting carbon nanotube's optical transitions at the van Hove singularities.

Figure 1.9 shows a typical UV/Vis/NIR spectrum of SWCNTs dispersed (via ultrasonication) in water with polyethylene glycol (PEG) and Triton-X 100. SWCNTs have the distinct wave-like feature that ranging between 390 nm-1600 nm where each peak corresponds to a specific chirality of the nanotube. This feature evaluates the SWCNT sample composition, dispersion efficiency, sample purity, quality of individualization, and chirality-based separation efficiency. Larger diameter nanotubes have a smaller band gap yielding a red-shifted peaks compared to smaller diameter nanotubes.[12] By ultracentrifugation, the bundles of the nanotubes can be removed to yield individualize nanotubes in the dispersion. Sharper and blue-shifting peaks in the spectrum evaluate the degree of debundling in the sample.[12] Finally, the number of peaks correlates to the chirality-based separation where the chiral purity of the nanotube yields increased absorption intensity at a particular wavelength.

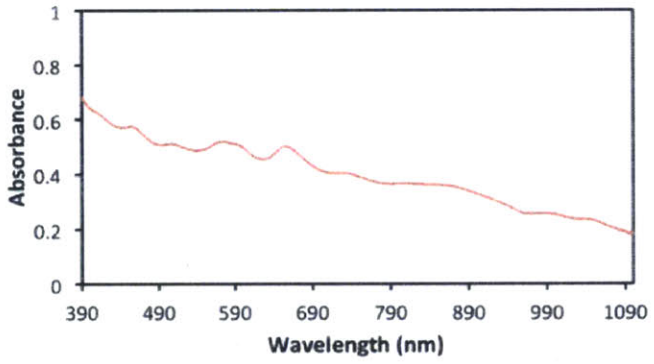

Figure 1.9. UV/Vis/NIR spectrum of 0.014 mg/ml SWCNTs dispersed in aqueous solution using PEG and Triton-X 100.

1.5 Carbon Nanotube Electron Transport Applications

Depending on chirality, SWCNTs can be either metallic or semiconductive. Metallic nanotubes have DOS at the Fermi level and the semiconducting nanotubes at the Fermi level have a band gap ($E_g \approx 0.5$-1 eV)[13] which scales inversely with tube diameter ($E_g \approx 0.84$ eV / d [nm]).[1] The theoretical intrinsic conductance of SWCNT is $h/4e^2 \sim 6.2k\Omega$ where there are four degeneracies (two for spin and two for orbital).[10] The nanotube's conductance can be investigated by depositing the nanotubes onto a silicon wafer substrate (with a thin SiO_2 layer) bridging the gap between two metal electrodes. Using the CNTs as the active element of a transistor is accomplished by applying a gate voltage (V_g) to the silicon where the SiO_2 layer (10-100nm) separates the nanotubes from the silicon. In the metallic nanotubes, the valence and conduction band crosses at the Fermi level where the nanotube's conductance is independent of the gate voltage. In contrast, varying V_g can change the magnitude of conduction for the semiconducting nanotubes. Negative V_g moves the Fermi level into the valence band resulting in an increase in conductivity. The Fermi level can also be tuned into the band gap by applying a positive V_g to produce near-zero conductance at room temperature (since $E_g \gg k_B T$).[10] This feature of manipulating the conductance of the nanotubes where we can have an ON/OFF switch establishes an opportunity in nanotechnology for sensory applications.

The electronic transport of electrons in carbon nanotubes is highly sensitive to environment changes. The presence of chemical species detected by the change of the nanotube's resistance results in portable, scalable, and easy to use chemiresistive sensors. Chemiresistors are fabricated by depositing the pristine semiconducting CNTs (conductive channel) between two electrodes where a small potential is supplied and the current is monitored. Applying an electric field creates a non-equilibrium electron distribution where the metal electrode's Fermi level is

adjusted asymmetrically to cause electrons to flow from one electrode to the other. Upon analyte exposure, the CNT film can exhibit changes in conductance by the following mechanism: *p*-doping/*n*-doping, electron scattering, hole pinning, and nanotube film swelling.

CNTs are p-type doped materials under O_2 at ambient conditions where the majority carriers are holes. The nanotubes can be de-doped by vacuum annealing at elevated temperatures to promote desorption of the molecular oxygen. Under ambient conditions, electron donating (e.g. NH_3)[14] or withdrawing (e.g. NO_2)[14] chemical species physically adsorbs onto the surface of the nanotube promoting charge transfer where the conductivity decreases or increases, respectively. The *n*-dopants fills the holes in the nanotube's valence band and the *p*-dopants inject more holes to cause reduction and enhancement in the conductivity of the originally *p*-doped carbon nanotubes. In the CNT-based chemiresistive sensors, electrons can scatter and holes can be pinned to produce a change in conductance due to impurities adsorbed onto the surface of the nanotube's sp^2-hybridization lattice. When the impurities are on the nanotube's walls, the electron feels the impurity potential averaged over the circumference wherein a larger nanotube diameter yields smaller scattering influence from the impurity.[13] The holes can be pinned by combining with electrons from the impurity (analyte). When an electric field is applied to the CNT-based device, electrons are known to tunnel through potential barriers of the device such as between the electrode-CNT and tube-to-tube contacts. Figure 1.10 illustrates tube-tube tunneling of electrons in one direction by applying a voltage. The tunneling resistance between two neighboring CNTs can be estimated as

$$R_{tunneling} \sim \frac{V}{AI} = \frac{h^2 d}{Ae^2\sqrt{2m\lambda}} e^{\left(\frac{4\pi d}{h}\sqrt{2m\lambda}\right)}$$

where I is the tunneling current density, V is the electrical potential difference, e the quantum of electrical charge, m the mass of electron, h is the Planck's constant, d is the distance between CNTs, λ the height of the barrier, and A is the cross-sectional area of tunnel.[15] d and λ are important parameters for nanotube sensory applications. When the chemical analyte penetrates through the CNT film, there is an increase in distance between the tube-tube and perhaps between the electrode-nanotube contacts. The swelling of the film increases distance between the tube-tube and the potential barrier for the electrons to tunnel resulting in an increase in resistance. The fabricate of selective CNT sensory films can be achieved by adding different selectors (small molecules, polymers, metals, metal salts, etc.) that has affinity towards certain analytes between the nanotubes to render the tunneling distance and potential barrier height more sensitive towards a certain analyte wherein a resistive change is observed.

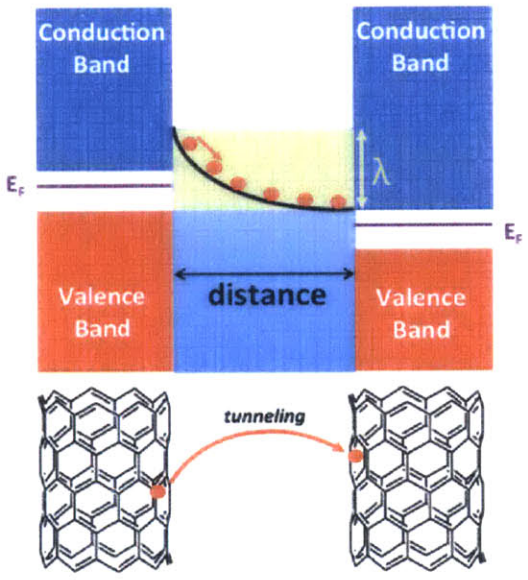

Figure 1.10. Tunneling between two neighboring carbon nanotubes with applied voltage. E_F is the Fermi Level and λ is the barrier height for tunneling.

1.6 Conclusion

Carbon nanotubes have unique electronic and spectroscopic properties that make the material useful in many applications. How the nanotubes are wrapped dictates the nanotube's electronic property is metallic (no energy band gap) or semiconducting (small energy band gap). Influencing the semiconducting nanotube's conductance using a gate voltage to rise and/or lower the Fermi level can make the material interesting for semiconducting sensory applications. Semiconducting SWCNTs-based chemiresistive sensors have become very popular due to the nanotube's one atom thick active layer, high conductivity, portability, scalability, and high conductive influences during environment changes.

1.7 References

(1) O'Connell, M. J. *Carbon Nanotubes: Properties and Applications*. (CRC Press, 2006).

(2) Iijima, S. Helical microtubules of graphitic carbon. *Nature* **354,** 56–58 (1991).

(3) Javey, A. The 2008 Kavli Prize in Nanoscience: Carbon Nanotubes. *ACS Nano* **2,** 1329–1335 (2008).

(4) Thomsen, C., Reich, S. & Maultzsch, J. *Carbon Nanotubes* 3–30 (Wiley-VCH Verlag GmbH, 2004).

(5) *Carbon Nanotubes*. **80,** (Springer Berlin Heidelberg, 2001).

(6) Dresselhaus, M. S., Dresselhaus, G., Saito, R. & Jorio, A. Raman spectroscopy of carbon nanotubes. *Phys. Rep.* **409,** 47–99 (2005).

(7) Birch, M. E., Ruda-Eberenz, T. A., Chai, M., Andrews, R. & Hatfield, R. L. Properties that Influence the Specific Surface Areas of Carbon Nanotubes and Nanofibers. *Ann. Occup. Hyg.* (2013). doi:10.1093/annhyg/met042

(8) Li, Y. (Grace), Lu, D. & Wong, C. P. *Electrical Conductive Adhesives with Nanotechnologies*. (Springer Science & Business Media, 2009).

(9) Thomsen, C., Reich, S. & Maultzsch, J. *Carbon Nanotubes* 31–65 (Wiley-VCH Verlag GmbH, 2004).

(10) *Carbon Nanotubes*. **111,** (Springer Berlin Heidelberg, 2008).

(11) Thomsen, C., Reich, S. & Maultzsch, J. *Carbon Nanotubes* 115–133 (Wiley-VCH Verlag GmbH, 2004).

(12) O'Connell, M. J. *et al.* Band Gap Fluorescence from Individual Single-Walled Carbon Nanotubes. *Science* **297,** 593–596 (2002).

(13) Thomsen, C., Reich, S. & Maultzsch, J. *Carbon Nanotubes* 85–100 (Wiley-VCH Verlag GmbH, 2004).

(14) Chang, H., Lee, J. D., Lee, S. M. & Lee, Y. H. Adsorption of NH3 and NO2 molecules on carbon nanotubes. *Appl. Phys. Lett.* **79,** 3863–3865 (2001).

(15) Hu, N., Karube, Y., Yan, C., Masuda, Z. & Fukunaga, H. Tunneling effect in a polymer/carbon nanotube nanocomposite strain sensor. *Acta Mater.* **56,** 2929–2936 (2008).

Chapter 2

Robust Cyclohexanone Selective Chemiresistors Based on Single-Walled Carbon Nanotubes

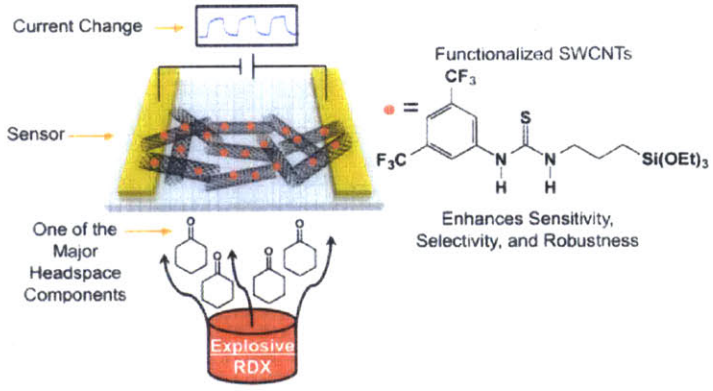

Adapted from: Frazier, K.M.; Swager, T.M. "Robust Cyclohexanone Selective Chemiresistors Based on Single-Walled Carbon Nanotubes," *Anal. Chem.*, **2013**, 85, 7154-7158.

2.1 Introduction

Detection of explosives and chemical and biological agents at trace levels as well as at stand-off distances has the potential to thwart terrorist activities.[1] Cyclotrimethylene trinitramine (RDX) was the second most produced explosive during World War II and is still widely used today.[1] However, vapors of RDX are difficult to detect due to its extremely low equilibrium vapor pressure of 6 ppt (parts per trillion) at 25 °C.[2] Current methods for detecting RDX, such as mass spectroscopy and gas chromatography, have high sensitivity and selectivity but are expensive, bulky, and require highly trained personnel for operation and data analysis.[1] An alternative approach to direct detection of RDX is the detection of cyclohexanone, a chemical used to recrystallize RDX.[3, 4] Cyclohexanone has a significantly higher equilibrium vapor pressure of 5000 ppm (parts per million) at 25 °C in comparison to RDX.[5] Previous studies have shown that cyclohexanone has a flux rate from land mines ranging from 1.1 to 98 g/(cm^2 s × 10^{13}) with varying soil types (soil and clay).[6]

Herein we describe a method that uses chemically functionalized single-walled carbon nanotubes (SWCNTs) to detect cyclohexanone with a theoretical detection limit of 5 ppm. This method uses highly conductive SWCNTs that experience resistive changes upon exposure to the analyte to yield a small, low-power, and simple sensor.[7, 8] Although SWCNTs are promising materials for vapor sensing, they currently have limitations. Pristine (unfunctionalized) SWCNTs-based sensors lack selectivity toward analytes that display low adsorbance affinity to the nanotube's graphene surfaces.[7] Additionally, the often weak adhesion of the SWCNT to the sensor's substrate can lead to structural changes during a sensor's lifecycle that affect performance.[7, 9] To impart selectivity, SWCNTs are often covalently or noncovalently functionalized.[8, 10-19] Covalent functionalization creates a robust structure but reduces the

electrical conductivity (lowers carrier mobility) of SWCNTs as a result of the introduction of defects in the π-system. Previous research in our lab has also developed covalently functionalized SWCNT-based sensors to detect cyclohexanone and investigated a number of related receptors.[20] Considering that most sensing schemes involve analyte/π-system interactions and therefore increase the resistance of the SWCNTs, beginning with a low resistance generally provides for higher sensitivity sensors. Alternatively, noncovalent functionalization can provide for minimal changes in the SWCNT's electronic properties, but during a sensor's lifecycle these compositions can undergo structural changes with multiple thermal and chemical treatments that change the sensory performance. As a result, there is a need for SWCNT-based sensors wherein the nanotube–receptor structure is fixed in place without the need for covalent functionalization of the sidewalls.

In this study, we noncovalently functionalize SWCNTs by dispersing the nanotubes in a medium of selectors (Figure 2.1a). The selectors are designed to recognize significant aspects of the analytes chemical structure/properties, and we find that trifunctional selector **1a** produces that best overall sensory properties. In addition to the hydrogen-bonding element, selector **1a** employs a bis(trifluoromethyl) aryl group, which has been found to π–π stack with aromatic molecules[21] and thereby provides a noncovalent interaction with SWCNTs. Selector **2a** uses pyrene, which is well-known to interact with the graphene surface of SWCNTs.[8, 17, 22] Additionally, the SWCNT network presented in this study is immobilized (fixed) through the polymerization of the alkoxyl silyl groups attached to the selectors to create materials suited for demanding solution sensing in high-sheer flows.

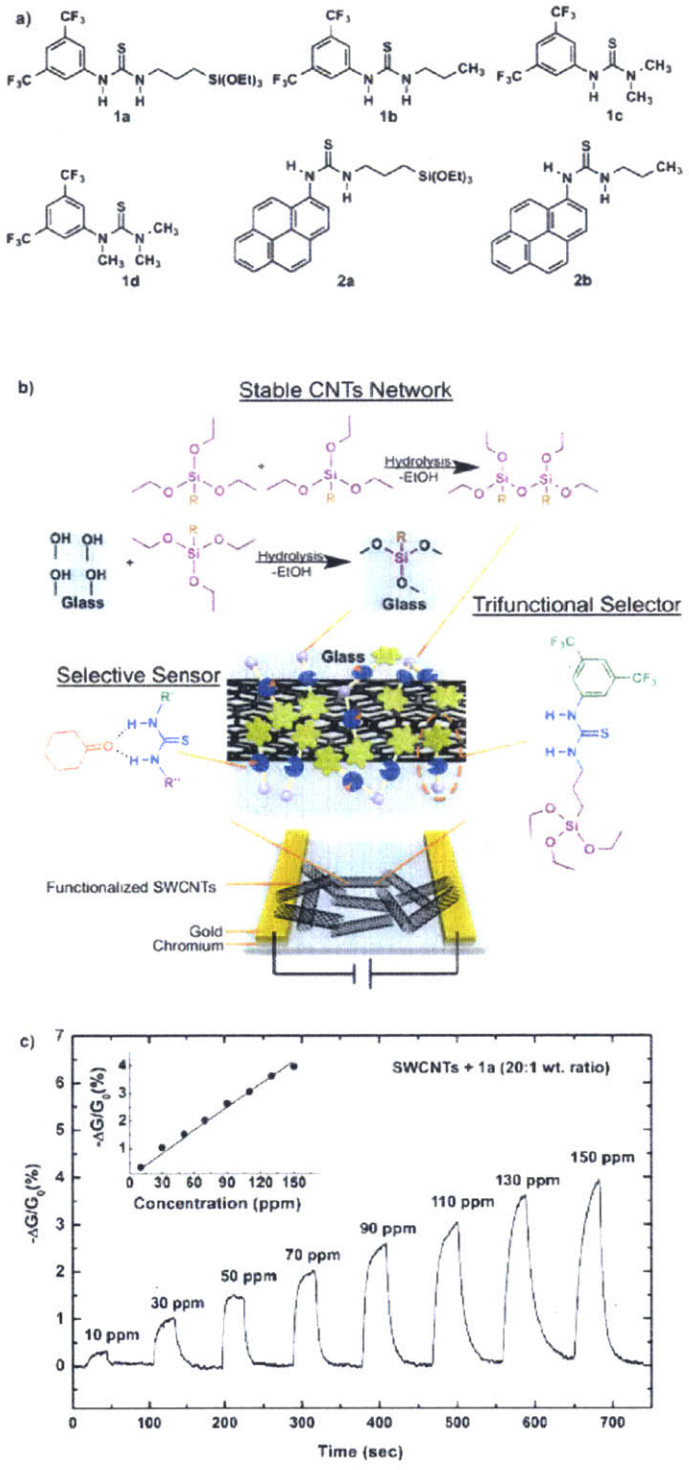

Figure 2.1. (a) Chemical structures of selectors presented in this study. (b) Schematic diagram of the sensing mechanism. (c) Normalized conductive change [$-\Delta G/G_0$ (%)] of the SWCNT-based sensor with trifunctional selector **1a** toward cyclohexanone at varying concentrations. The inset figure shows the magnitude of the normalized conductive change as a function of concentration of cyclohexanone.

2.2 Results and Discussion

To address the current limitations of SWCNT-based sensors, we have designed and synthesized trifunctional selectors that enhance the selectivity, sensitivity, and robustness of the resultant devices. Figure 2.1b shows the conceptual hypothesis behind the trifunctional selector. The preferred selector identified in this study has three important units: the first component is a bis(trifluoromethyl) aryl group, which promotes noncovalent functionalization of the SWCNTs with cofacial π–π interactions. The second component is a thiourea receptor that is known to bind to ketones via two-point hydrogen bonding and has been used to detect cyclohexanone previously.[20, 23] The third component is a triethoxysilane (TES) group that reacts to create a polymer network structure and also reacts with hydroxyl groups on the surface of glass[24] thereby immobilizing both the SWCNT and receptor to produce a highly stable device.

Sensory devices are produced by dispersing SWCNTs and a selector (Figure 2.1a) with ultrasonication in tetrahydrofuran (THF) and then drop casting the solution between two gold electrodes separated by 300 μm. The hydrolysis/polymerization of the TES groups appears to occur under ambient conditions,[25] and to demonstrate the simplicity of the method we did not introduce any special conditions to enhance this process. Our rationale is that only small amounts of TES are present and the high surface area of the composite structures promotes the hydrolytic reactions. Studies demonstrating insensitivity to humidity (vide infra) also suggest that the structures are fixed quickly upon fabrication. Sensing studies are performed by applying a small constant bias voltage (50 mV) using a potentiostat between the electrodes and the amount of material deposited was determined by reaching a target resistance between 26 and 250 kΩ. For controlled vapor delivery, the sensor is inserted into a Teflon enclosure and analyte vapors in a nitrogen carrier gas are flowed over the sample while the current is monitored.

Upon exposure to cyclohexanone, there is an instant increase in resistance for both pristine SWCNTs-based sensors and our functionalized SWCNTs-based sensors. For pristine SWCNTs-based sensors, the sensor response is likely the result of the cyclohexanone's dipole interacting with the cationic carriers (holes) that are present as a result of oxidative (air oxidation) doping. The reduction in the intra-SWCNT conductance is consistent with the pinning and/or scattering of the holes by the carbonyl dipole. It is also possible that absorption of the cyclohexanone increases the resistance between SWCNTs either by swelling the network to give wider tunneling barriers or through dipolar-induced changes of the energetics of key intertube conduction pathways that are possibly associated with defect sites. Considering the intrinsic sensitivity of SWCNTs to a wide range of molecules, it is important that a selector enhance the sensitivity to a select analyte or analyte class. In the simplest mechanism, the selector enhances the response by simply binding the analyte and effectively concentrating it in the SWCNT network. Alternatively the selector can have a more active role in modifying carrier transport. Specifically, the sulfur of the thiourea displays dipolar interactions with the nanotubes and binding of these groups to the SWCNTs networks increases the resistance. However, the hydrogen-bonded complex with cyclohexanone will give an enhanced collective dipole (Scheme 2.1) that will further pin or scatter carriers for increased sensitivity.

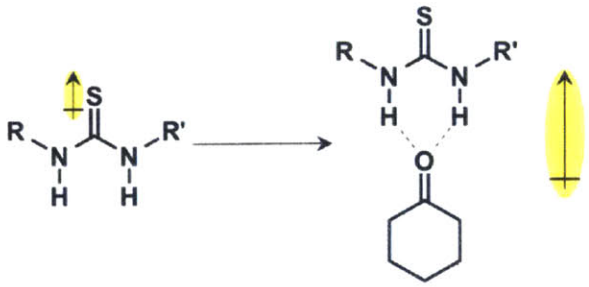

Scheme 2.1. Thiourea-selector's enhanced dipole interactions with cyclohexanone.

Figure 2.1c shows a plot of normalized conductance ($-\Delta G/G_0$) responses of SWCNT-based sensors with trifunctional selector **1a** to various concentrations of cyclohexanone. We applied minor baseline correction to all the data collected in this study to account for the linear current drift of the sensor. As shown, our sensors display real-time detection of cyclohexanone with reversible responses and fast recovery rates. The inset figure displayed a linear concentration-dependent change in resistance. Six sensors were capable of reproducible detection of 10 ppm of cyclohexanone and displayed an average theoretical limit of detection (LOD) of 5 ppm. The LOD calculations were based on established procedures described in the Appendix.[26]

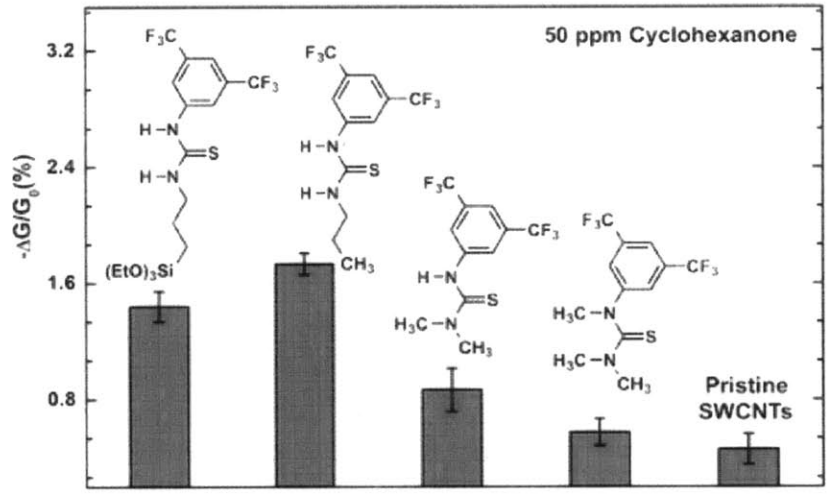

Figure 2.2. Normalized average conductive change [$-\Delta G/G_0$ (%)] of SWCNT-based sensors with different selectors to 50 ppm cyclohexanone. The vertical error bars represent the standard deviation from the average based on three sensors exposed to 50 ppm cyclohexanone four times for 30 s.

Other trifunctional selectors and control compounds investigated make use of pyrene moieties (**2a** and **2b**) that are well-known in the noncovalent functionalization of the SWCNTs

by π–π interactions.[8, 17, 22] These trifunctional selectors allow for stable dispersions of SWCNTs to be prepared in THF. As a result of the strong association of the pyrene to the SWCNTs, these sensors were subjected to aggressive treatments to determine the robustness. Three sensors were fabricated from 0.02 mg/mL of **2a**, and SWCNTs (2:1 wt ratio) were subjected to overnight treatments to best hydrolyze/polymerize the TES group (ambient conditions, ambient conditions after exposing to HCl vapor from the headspace of 12 M HCl solution, and heating at 80 °C under reduced pressure). These sensors were then sonicated (20 min) in methanol, and we found that only the heat-treated sensors survived. Most importantly, we found that the 80 °C pretreatment does not affect the device sensitivity (Figure A2.3a). The pyrene anchors in **2a** were highly effective in immobilizing the SWCNTs on the surface of the substrate such that it can withstand harsh conditions (e.g., ultrasonication) without detaching from the substrate (Figure A2.3b). Although the device stability with these trifunctional selectors **2a** is exceptional, the sensitivity and selectivity were poor, and the resultant devices displayed ketone responses that are equivalent to pristine SWCNTs. Therefore, we have focused on **1a** with the bis(trifluoromethyl) aryl group for the noncovalent attachment of the receptors to the SWCNTs. The role of (trifluoromethyl) aryls goes beyond promoting associations with the SWCNTs and also extends to the recognition process. Specifically, the inductive effects of the CF_3 groups cause the thiourea's protons to be more acidic, thereby rendering a more sensitive and selective device toward cyclohexanone.[27] The interactions between cyclohexanone and the thiourea moiety are shown in Figure 2.2. Each sensor was placed in a sensor array and simultaneously exposed to 1% cyclohexanone. Both selectors **1a** and **1b** (a homologue without a TES group) showed over 2-fold increase in sensitivity to cyclohexanone in comparison to pristine SWCNTs. Note that selector **1a** also exhibits approximately the same response as selector **1b**, therefore

suggesting that cyclohexanone does not interact strongly with TES. Selector **1a**'s slight decrease in response could be the result of the polymeric/surface chemistry limiting the interactions with the SWCNTs, and this can result in fewer selectors residing on or directly proximate to the π-surface of the SWCNTs. To prove that the primary interaction of cyclohexanone is through the hydrogen bonding with the thiourea receptor, we prepared methylated thiourea receptors. Monomethylated selector (**1c**) showed 39% decrease in the response, with respect to selector **1b**. Selector **1d**, in which both hydrogens of the thiourea are replaced with methyl groups, displays an additional 21% decrease in response and effectively produces a response that is equivalent to pristine SWCNTs. Upon the basis of these structure–activity relationships, it appears that cyclohexanone interacts with the thiourea receptor via hydrogen bonding. This binding in turn causes an increase in the resistance of the functionalized SWCNTs network.

Our investigations of the selectivity of sensors formed from SWCNTs with and without selector **1a** are summarized in Figure 2.3a. Each sensor was placed in an array and was exposed to 1% vapor concentration of various analytes (acetone, ethyl acetate, hexane, toluene, benzene, ethanol, and acetonitrile). We chose to test these particular interfering analytes because they can be commonly found in tobacco smoke, nail polish, alcoholic beverages, gasoline, lotion, perfume, etc. The pristine SWCNTs exhibited low sensitivity and selectivity to various analytes compared to functionalized SWCNTs. Functionalizing the SWCNTs selectively enhanced their sensitivity toward the analytes that are capable of hydrogen-bonding interactions with the thiourea receptor. In accord with our expectations, the sensor exhibited the highest sensitivity enhancement toward cyclohexanone. Note that cyclohexanone displays the lowest vapor concentration but produces the highest resistive change in comparison to other analytes. We find that sensors produced from **1a** and SWCNTs are particularly sensitive toward cyclohexanone.

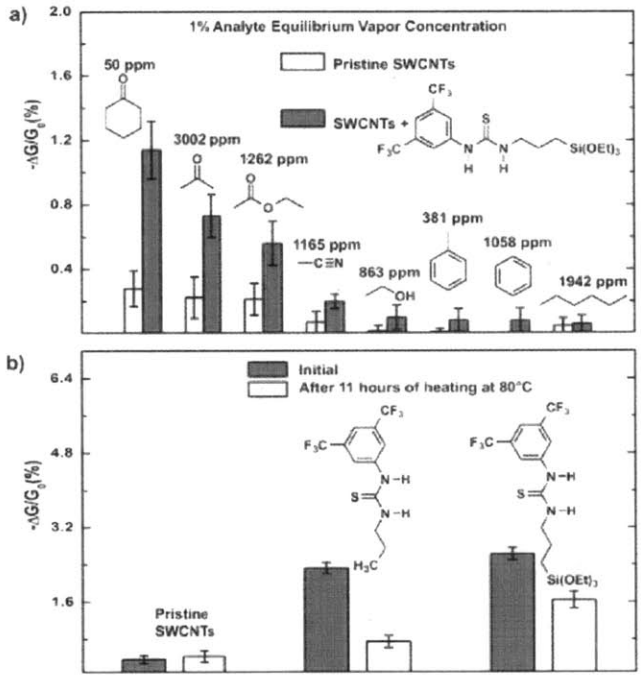

Figure 2.3. (a) Plot of normalized average conductive change [$-\Delta G/G_0$ (%)] of SWCNT-based sensors with or without trifunctional selector **1a**. The sensors were exposed to various analytes at 1% equilibrium vapor concentration. (b) The plot of normalized average conductive change [$-\Delta G/G_0$ (%)] of SWCNT-based sensors with different selectors to 50 ppm cyclohexanone before and after 11 h of heating at 80 °C under reduced vapor pressure.

We have also investigated the stability and sensitivity of our devices toward mechanical damage by sonication, heat, and humidity, because we anticipate that useful sensors will need to withstand extreme conditions (e.g., deserts, sweltering delivery trucks, containers, etc.). To evaluate the mechanical robustness of the devices, we submerged sensors into methanol and exposed them to prolonged ultrasonication (20 min). As mentioned earlier, the pyrene groups provided a strong anchor and survived these harsh conditions with pretreatment of heat. However, devices using selector **1a** did not withstand ultrasonication conditions even after catalytic efforts to hydrolyze/polymerize TES group by heating devices overnight at 80 °C under

reduced pressure. To assess the device's thermal resistance, each sensor was placed in an array and simultaneously exposed to a 1% vapor concentration of cyclohexanone. The sensors were then heated at 80 °C for 11 h under reduced pressure, allowed to cool, and re-exposed to 1% vapor concentration of cyclohexanone. We observed enhanced robustness with respect to heat from the SWCNT devices functionalized with TES (Figure 2.3b). After the long duration of heating, sensors with selector **1b** showed 60% decrease in sensitivity, whereas sensors with selector **1a** showed a 27% decrease in sensitivity and a response still at least 2-fold better than pristine SWCNTs. The surface linkages and networks formed from TES oligomerization likely prevent selector **1a** from phase separating from the SWCNT's surface or decomposing under high-temperature conditions. To examine the sensor's stability under humid conditions, the devices experienced prolonged exposure to relative humidity ranging from 0% to 80% (Figure A2.4a). At 80% relative humidity, six sensors with selector **1a** had an average resistive change of 20% ± 4%, while six pristine SWCNTs sensors had an average resistive change of 47% ± 8%. The trifunctional selector **1a** provides a long-standing SWCNT network that is less probable of SWCNT moving disrupting the SWCNT contacts thus increasing the SWCNT network's resistance. The sensors using selector **1a** that experienced a small change in resistance upon prolonged high-humidity conditions showed no significant decrease in sensitivity toward cyclohexanone average conductive changes after devices were exposed to 1% vapor concentration of cyclohexanone with relative humidity ranging from 0% to 80% (Figure 2.4b).

2.3 Conclusion

In summary, we have shown through experimentation that trifunctional selectors can be used to create robust SWCNT chemiresistors with useful response to the explosives signature

cyclohexanone. Sensors using selector **1a** displayed the best responses, and structure–property relationships suggest that the ability of these materials to detect cyclohexanone is the result of selective hydrogen bonding. The resultant robust sensors were able to withstand high temperature and humidity and displayed reversible and reproducible responses in less than 30 s to 10 ppm of cyclohexanone. The design strategies of the trifunctional selectors described establish the foundation for the design and fabrication of selective SWCNT-based gas and liquid sensors with exceptional stability and robustness.

2.4 *Experimental Section*

Glass slides were sonicated in acetone (30 min) and treated with an oxygen plasma (5 min) from Harrick Plasma. The glass slides were then placed into a thermal deposition machine (Angstrom Engineering) with a homemade stainless steal mask on top. Chromium adhesive layers (10 nm) and gold electrodes (75 nm) were deposited onto the surface of the glass with a gap (300 μm) between the metal electrodes. SWCNTs were purchased from Sigma-Aldrich (≥70% purity and 0.7–1.3 nm diameter). Before using SWCNTs, they were treated with concentrated hydrochloric acid and washed with deionized water. The SWCNTs were then dried (200 °C) under reduced pressure and stored in dry atmosphere. Solutions (0.02 mg/mL SWCNT and 0.4 mg/mL selector) of selector/SWCNT (20:1 wt ratio) in THF were produced by ultrasonication (5 min). Approximately 0.1 μL of the solution was drop cast between the gold electrodes until a resistance range (26–250 kΩ) was achieved. The sensor chips were allowed to dry (30 min at 40 °C) under reduced pressure before any sensing measurements. After drying, the devices were placed in a small Teflon enclosure and a small voltage (50 mV) was applied from a potentiostat (PalmSens:EMStatMUX16). The current passing through the sensors was

monitored while exposing it to various analytes (with dry nitrogen as the carrier gas) four consecutive times for 30 s with a recovery time of 1 min, and the sensors were examined in triplicate. The gas mixtures were produced by KIN-TEK gas generator system. In the sonication study, the devices were placed in a beaker full of methanol and experienced ultrasonication (20 min). Synthesis of selectors can be found in the Appendix. The selectors were confirmed using Bruker 400 nuclear magnetic resonance NMR and high-resolution mass spectrometry.

2.5 References

(1) Moore, D. S. *Rev. Sci. Instrum.* **2004**, 75, 2499– 2512.

(2) Kolla, P. Angew. Chem., *Int. Ed. Engl.* **1997**, 36, 800– 811.

(3) Lai, H.; Leung, A.; Magee, M.; Almirall, J. R. Anal. Bioanal. Chem. 2010, 396, 2997–3007.

(4) O'Reilly, W. F.; Jenkins, T. F.; Murrmann, R. P.; Leggett, D. C.; Barrierra, R.; Exploratory Analysis of Vapor Impurities from TNT, RDX and Composition B; Cold Regions Research and Engineering Lab, Hanover, NH; Defense Technical Information Center: Ft. Belvoir, VA,1973.

(5) Yaws, C. L. The Yaws Handbook of Vapor Pressure: Antoine Coefficients; Gulf Publishing Company: Houston, TX, 2007.

(6) Jenkins, T. F. Detection of Cyclohexanone in the Atmosphere above Emplaced Antitank Mines; U.S. Army Mobility Equipment Research and Development Center, Corps of Engineers, U.S. Army Cold Regions Research and Engineering Laboratory: Hanover, NH,1974.

(7) Zhang, T.; Mubeen, S.; Myung, N. V.; Deshusses, M. A. *Nanotechnology* **2008**, 19, 1–14.

(8) Schnorr, J. M.; Swager, T. M. *Chem. Mater.* **2011**, 23, 646– 657.

(9) Su, H.-C.; Chen, C.-H.; Chen, Y.-C.; Yao, D.-J.; Chen, H.; Chang, Y.-C.; Yew, T.-R. *Carbon* **2010**, 48, 805– 812.

(10) Cui, S.; Pu, H.; Lu, G.; Wen, Z.; Mattson, E. C.; Hirschmugl, C.; Gajdardziska-

Josifovska, M.; Weinert, M.; Chen, J. *ACS Appl. Mater. Interfaces* **2012**, 4, 4898– 4904.

(11) Shi, D.; Wei, L.; Wang, J.; Zhao, J.; Chen, C.; Xu, D.; Geng, H.; Zhang, Y. *Sens. Actuators, B* 2013, 177, 370– 375.

(12) Qi, P.; Vermesh, O.; Grecu, M.; Javey, A.; Wang, Q.; Dai, H.; Peng, S.; Cho, K. J. *Nano Lett.* **2003**, 3, 347– 351.

(13) Staii, C.; Johnson, A. T.; Chen, M.; Gelperin, A. Nano Lett. 2005, 5, 1774– 1778.

(14) Chen, L.; Xie, H.; Yu, W. Functionalization Methods of Carbon Nanotubes and Its Applications. In Carbon Nanotubes Applications on Electron Devices; Marulanda, J. M., Ed.;InTech: New York, 2011.

(15) Bekyarova, E.; Davis, M.; Burch, T.; Itkis, M. E.; Zhao, B.; Sunshine, S.; Haddon, R. C. J. *Phys. Chem. B* **2004**, 108, 19717– 19720.

(16) Kong, L.; Wang, J.; Luo, T.; Meng, F.; Chen, X.; Li, M.; Liu, *J. Analyst* **2010**, 135, 368– 374.

(17) Karousis, N.; Tagmatarchis, N.; Tasis, D. *Chem. Rev.* **2010**, 110, 5366– 5397.

(18) Dionisio, M.; Schnorr, J. M.; Michaelis, V. K.; Griffin, R. G.; Swager, T. M.; Dalcanale, E. J. *Am. Chem. Soc.* **2012**, 134, 6540– 6543.

(19) Wang, F.; Swager, T. M. *J. Am. Chem. Soc.* **2011**, 133, 11181– 11193.

(20) Schnorr, J. M.; van der Zwaag, D.; Walish, J. J.; Weizmann, Y.; Swager, T. M. *Adv. Funct. Mater.* **2013**, 23, 5285-5291.

(21) Liu, J.; Wendt, N. L.; Boarman, K. *J. Org. Lett.* **2005**, 7, 1007– 1010.

(22) Lerner, M. B.; Resczenski, J. M.; Amin, A.; Johnson, R. R.; Goldsmith, J. I.; Johnson, A. T. C. *J. Am. Chem. Soc.* **2012**, 134, 14318– 14321.

(23) Cox, J. R.; Müller, P.; Swager, T. M. *J. Am. Chem. Soc.* **2011**, 133, 12910– 12913.

(24) Haensch, C.; Hoeppener, S.; Schubert, *U. S. Chem. Soc. Rev.* **2010**, 39, 2323.

(25) Yang, Y.; Bittner, A. M.; Baldelli, S.; Kern, K. *Thin Solid Films* **2008**, 516, 3948–3956.

(26) Li, J.; Lu, Y.; Ye, Q.; Cinke, M.; Han, J.; Meyyappan, M. *Nano Lett.* **2003**, 3, 929– 933.

(27) Pihko, P. M. Hydrogen Bonding in Organic Synthesis; Wiley-VCH: Weinheim, Germany, 2009.

Chapter 2 Appendix

^{1}H-NMR, ^{19}F-NMR, and C-NMR Spectra And Additional Figures

Adapted from: Frazier, K.M.; Swager, T.M. "Robust Cyclohexanone Selective Chemiresistors Based on Single-Walled Carbon Nanotubes," *Anal. Chem.*, **2013**, 85, 7154-7158.

General Materials and Methods:

All chemicals and reagents were purchased from Sigma-Aldrich and used without further purification, unless noted otherwise.

Device Fabrication:

Glass slides (VWR Microscope Slides) were cleaned by ultra-sonication in acetone for 30 min and dried using a stream of nitrogen. The glass slides were then cleaned with an oxygen Plasma (Harrick Plasma) for 5 min. Using a home-made stainless steal mask, layers of chromium (10 nm) and gold (75 nm) were deposited onto the glass slides using a thermal deposition purchased from Angstrom Engineering. There was a 300 μm gap between the metal electrodes. Before using SWCNTs, they were treated with concentrated hydrochloric acid to remove metal impurities and washed with deionized water. The SWCNTs were then dried at 200 °C under reduced pressure and stored in dry atmosphere. A mixture of pristine SWCNTs and selector were added to tetrahydrofuran (THF) at a concentration of 0.02 mg/mL and 0.4 mg/mL , respectively. The solutions were prepared by ultrasonication for 5 min in a bath sonicator. Approximately 0.1 μL of the solution was dropcast between the gold electrodes until 26 kΩ-250 kΩ resistance range was achieved. The sensor chips were allowed to dry for 30 min at 40 °C under reduced pressure before any sensing measurements.

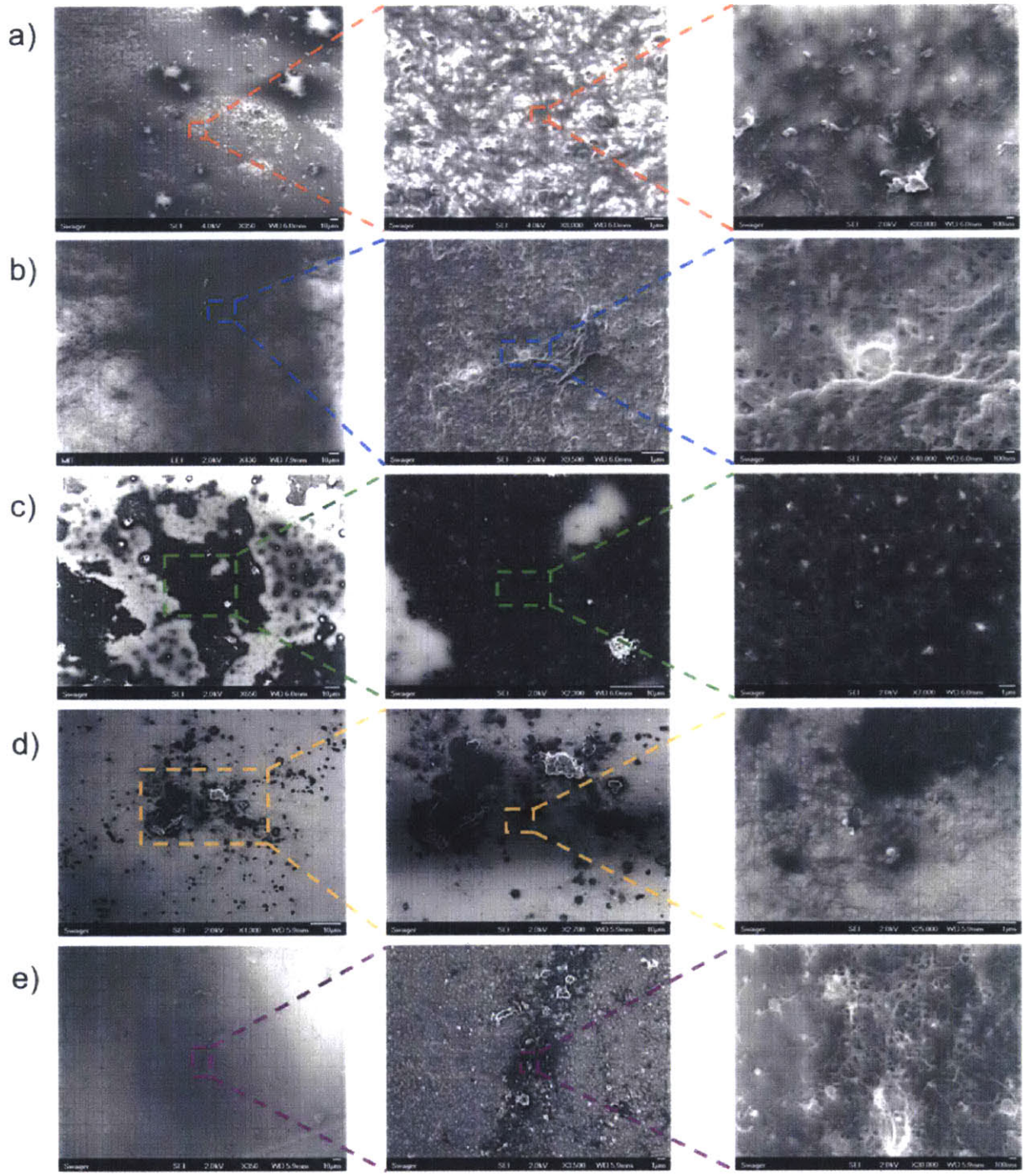

Figure A2.1. SEM images of SWCNTs-based sensors: a) SWCNT functionalized with selector **2a**. b) SWCNT functionalized with selector **2b**. c) SWCNT functionalized with selector **1a**. d) SWCNT functionalized with selector **1b**. e) Pristine SWCNT.

Sensing Measurement:

Figure S2 depicts our sensing setup. The sensor chip was placed in a small Teflon enclosure and 50 mV of potential was applied. The current through the sensor was monitored while exposing it to various analytes (with dry nitrogen as the carrier gas) four consecutive times for 30 s with a recovery time of 1 min and the sensors were examined in triplicate.

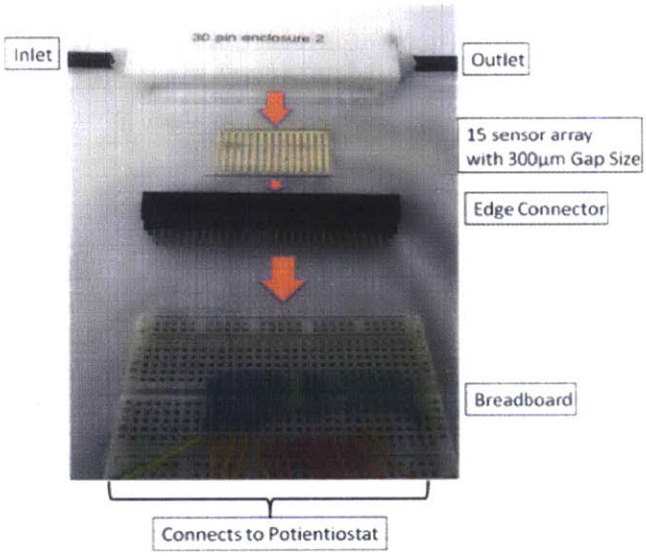

Figure A2.2. Diagram of sensing measurement setup.

$$\frac{(-\Delta G)}{G_0}(\%) = \frac{-(Final\ Current - Initial\ Current)}{Initial\ Current} \times 100$$

Equation A2.1

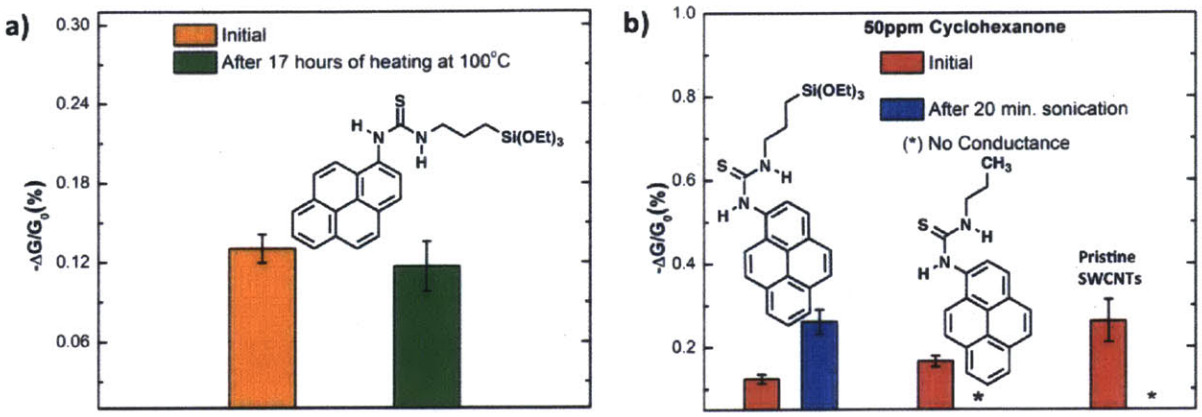

Figure A2.3. a) The plot of normalized average conductive change ($-\Delta G/G_0$ (%)) of three SWNCT-based sensors exposed four consecutive times to 50 ppm cyclohexanone for 30 sec and allowed to recover for 30 s before and after 17 h of heating at 100 °C under reduced pressure. b) The plot shows normalized average conductive change ($-\Delta G/G_0$ (%)) of three SWNCT-based sensors exposed four consecutive times to 50 ppm cyclohexanone for 30 s and allowed to recover for 30 s before and after sonication in methanol. An Asterisk (*) denotes devices that no longer display a detectable conductance after sonication.

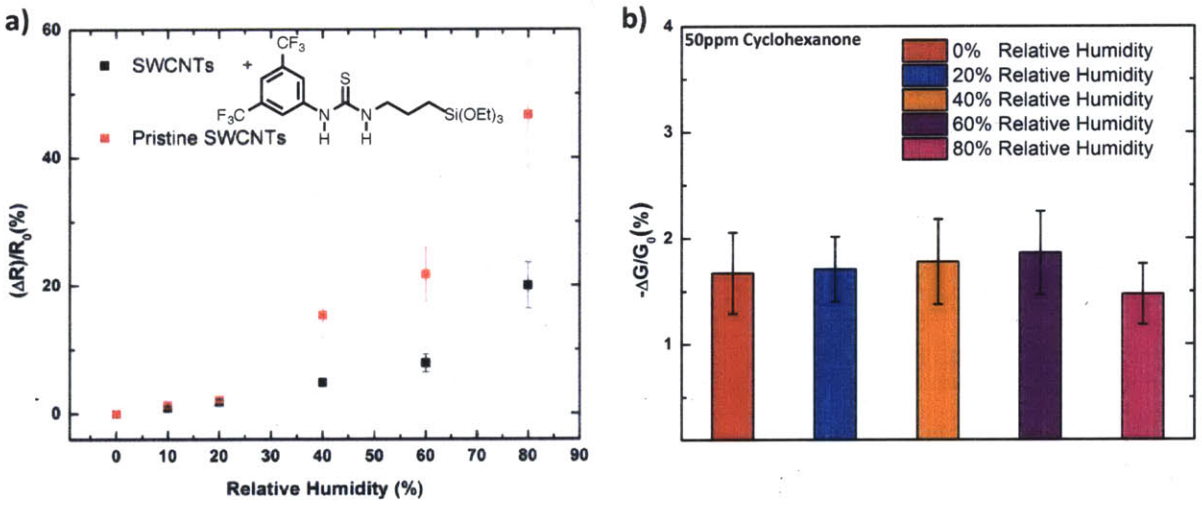

Figure A2.4. a) The plot shows normalized average resistive change ($-\Delta R/R_0$ (%)) of six SWNCT-based sensors with or without selector 1a after prolonged exposure to various humid conditions. b) The plot shows normalized average conductive change ($-\Delta G/G_0$ (%)) of six SWNCT-based sensors with selector 1a simultaneously exposed four consecutive times to 50 ppm cyclohexanone for 30 s and allowed to recover for 1 min at various humidity levels.

Calculation of Theoretical Limit of Detection (LOD) for Cyclohexanone with Functionalized SWCNTs-based Devices:

We calculated the noise of the sensor using the deviation in conductance in the baseline prior to exposing the sensor to cycohexanone using the root-mean-square (rms). We took 20 consecutive data points prior to exposure to the analyte, plotted the data, and fit it to a fifth-order polynomial. We then calculated V_{x^2} using Eq. A2.2. In this equation, y_i is the measured value of conductance ($-\Delta G/G_0$) and y is the corresponding value calculated from the fifth-order polynomial fit. We then used Eq. A2.3 to calculate rms_{noise} of the sensors, where N is the number of data points used for curve fitting (N = 20). The average rms_{noise} of six sensors was 0.000316 ± 0.000127. When the signal-to-noise ratio equaled 3, then the signal was considered to be a true signal. Therefore, Eq. A2.4 yielded the theoretical limit of detection (LOD) of the sensors. In this equation, *slope* is the slope of the linear regression fit on the sensor response ($-\Delta G / G_0$) vs concentration plot (shown in Figure A2.5).

$$V_{x^2} = \sum (y_i - y)^2 \qquad \textbf{Equation A2.2}$$

$$rms_{noise} = \sqrt{\frac{V_{x^2}}{N}} \qquad \textbf{Equation A2.3}$$

$$LOD = 3\frac{(rms_{noise})}{slope} \qquad \textbf{Equation A2.4}$$

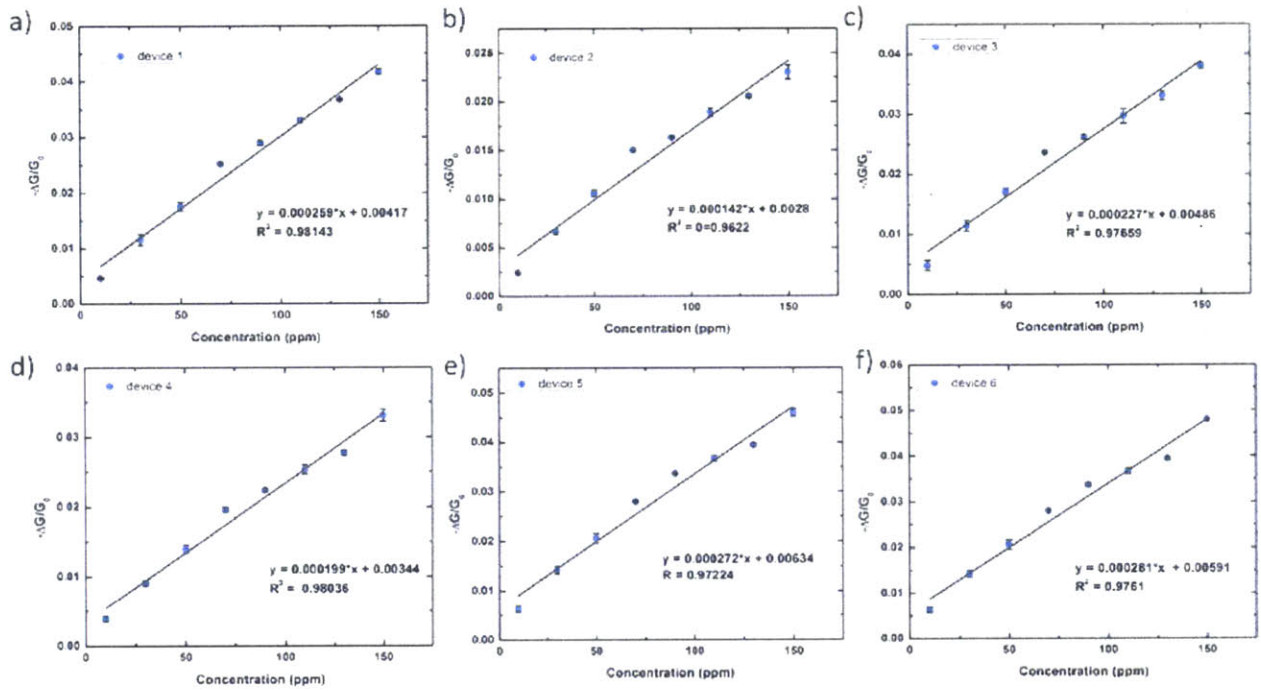

Figure A2.5. Calibration curve of sensors simultaneously exposed to various concentrations of cyclohexanone four consecutive times for 30 s and allowed to recover for 1 min.

Synthesis:

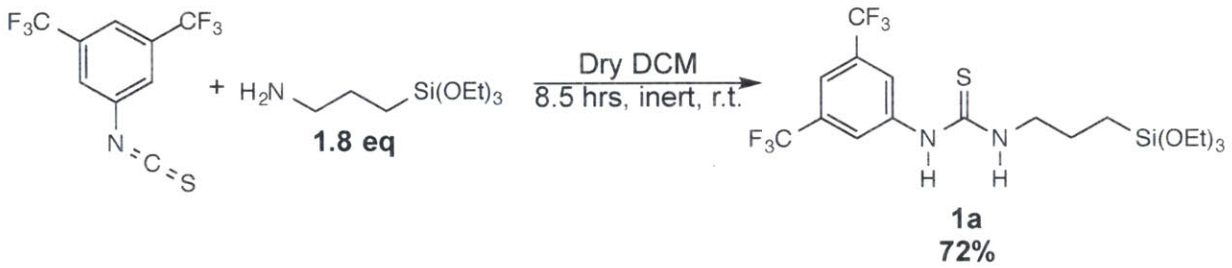

1-(3,5-bis(trifluoromethyl)phenyl)-3-(3-(triethoxysilyl)propyl)thiourea (1a):

3,5-Bis(trifluoromethyl)phenyl isothiocyante (0.68 mL , 2.05 mmol) was added dropwise to a stirring solution of (3-Aminopropyl)triethoxysilane (0.87 mL , 3.72 mmol) in dry dichloromethane (5 mL) at room temperature under inert atmosphere. The mixture was stirred for 8.5 h. The solvent was removed under reduced pressure. The crude was dissolved in 5 mL of acetonitrile and washed with 5 mL of hexane. The solution was dried under reduced pressure to

yield a yellow oil. Compound was stored under dry atmosphere. Yield: 1.3152 g (72%); ^{1}H NMR (401 MHz, DMSO-d_6, δ): 9.99 ppm (s, 1H), 8.25 ppm (s br, 3H, Ar H), 7.70 ppm (s, 1H), 3.79 - 3.74 ppm (q, J = 7 Hz, 6H), 3.48 ppm (s, 2H), 1.68 - 1.58 ppm (m, J = 7 Hz, 2H), 1.18 ppm (t, J = 7 Hz , 9H), 0.63 - 0.59 ppm (t, J = 8 Hz, 2H); ^{19}F NMR (401 MHz, DMSO-d_6, δ): -61.74 ppm (s); ^{13}C NMR (401 MHz, DMSO-d_6, δ): 180.45 ppm (s), 142 ppm (s), 130.62 - 129.66 ppm (q, J= 33 Hz), 127.32 ppm (s), 124.61 ppm (s), 121.90 ppm (s), 121.75 ppm (s br), 119.19 ppm (s), 115.80 ppm (s br), 57.73 ppm (s br), 57.67 ppm (s), 56.02 ppm (s), 46.44 ppm (s), 21.82 ppm (s), 18.52 ppm (s), 18.17 ppm (s), 7.38 ppm (s); HRMS calc. for $C_{18}H_{26}F_6N_2O_3SSi$ $[M+H]^+$: 493.15, found: 493.1262 $[M+H]^+$

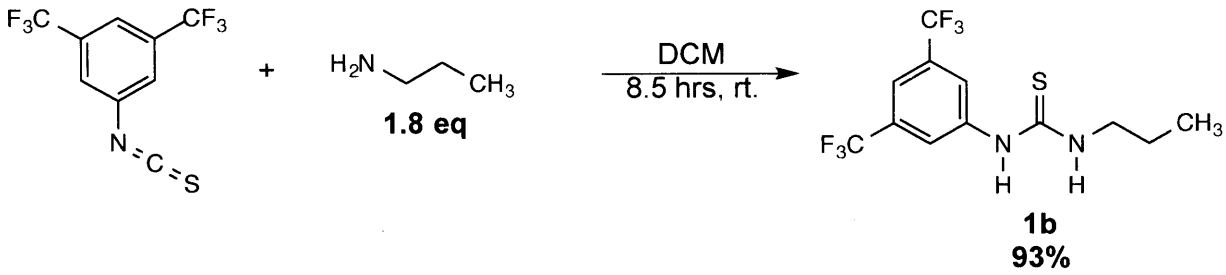

1-(3,5-bis(trifluoromethyl)phenyl)-3-propylthiourea (1b):

3,5-Bis(trifluoromethyl)phenyl isothiocyante (0.68 mL , 2.05 mmol) was added dropwise to a stirring solution of propylamine (0.31 mL , 3.77 mmol) in dichloromethane (5 mL) at room temperature. The mixture was stirred for 8.5 h. The solvent was removed under reduced pressure. The crude was washed with hexane and dried under reduced pressure to yield a white solid compound. Yield: 1.1416 g (93%); ^{1}H NMR (400 MHz, DMSO-d_6, δ): 10.01 ppm (s, 1H), 8.27 ppm (s br, 2 H), 8.22 ppm (s, 1H), 7.64 ppm (s, 1H, Ar H), 3.47 ppm (s br, 2H, Ar H), 1.63 - 1.54 ppm (m, J = 7 Hz, 2H), 0.93 - 0.89 ppm (t, J = 7 Hz, 3H); ^{19}F NMR (401 MHz, DMSO-d_6, δ): -62.02 ppm (s); ^{13}C NMR (400 MHz, DMSO-d_6, δ): 180.56 ppm (s), 142.14 ppm (s), 130.70 - 129.72 ppm (q, J = 33 Hz), 127.36 ppm (s), 124.65 ppm (s), 121.94 ppm (s), 121.68 ppm (s br),

119.23 ppm (s), 115.65 ppm (s br), 45.63 ppm (s), 21.56 ppm (s), 11.27 ppm (s); HRMS calc. for $C_{12}H_{12}F_6N_2S$ $[M+H]^+$: 331.06, found: 331.0673 $[M+H]^+$

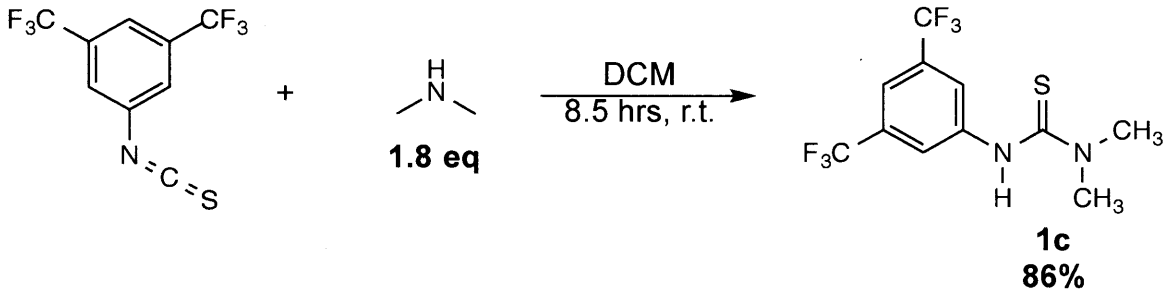

1c
86%

3-(3,5-bis(trifluoromethyl)phenyl)-1,1-dimethylthiourea (1c):

3,5-Bis(trifluoromethyl)phenyl isothiocyante (0.68 mL , 2.05 mmol) was added dropwise to a stirring solution of 40wt% dimethyl amine solution (0.47 mL , 3.71 mmol) in dichloromethane (5 mL) at room temperature. The mixture was stirred for 8.5 h. The solvent was removed under reduced pressure. The compound was washed with hexane and dried under reduced pressure to yield a white solid compound. Yield: 1.0134 g (86%); ^{1}H NMR (400 MHz, DMSO-d_6, δ): 9.51 ppm (s, 1H), 8.16 ppm (s, 2H, Ar H), 7.71 ppm (s, 1H, Ar H), 3.34 ppm (s, 3H); ^{19}F NMR (401 MHz, DMSO-d_6, δ): -61.86 ppm (s); ^{13}C NMR (400 MHz, DMSO-d_6, δ): 181.06 ppm (s), 143.66 ppm (s), 130.56 - 129.58 ppm (q, J = 33 Hz), 127.83 ppm (s), 125.12 ppm (s), 124.88 - 124.85 ppm (d, J = 3 Hz), 122.41 ppm (s), 119.70 ppm (s), 116.76-116.61 ppm (m, J = 4 Hz), 41.47 ppm (s br); HRMS calc. for $C_{11}H_{10}F_6N_2S$ $[M+H]^+$: 317.05, found: 317.0525 $[M+H]^+$

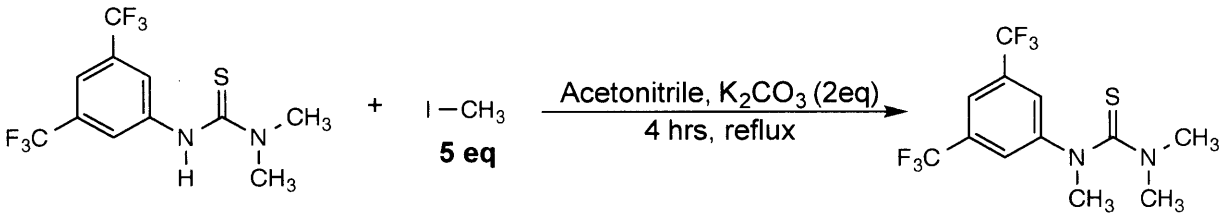

1d
14%

1-(3,5-bis(trifluoromethyl)phenyl)-1,3,3-trimethylthiourea (1d):

Add iodomethane (0.97 mL , 15.58 mmol) to a suspension of Selector 1b (1.0360g , 3.28 mmol) and potassium carbonate (0.8677g , 6.28 mmol) in acetonitrile (10 mL). The mixture was stirred and refluxed for 4 h. After the mixture was cooled to room temperature, the solution was filtered and solvent was removed under reduced pressure. The crude was washed with warm ethyl acetate and ethanol then dried under reduced pressure to yield a white solid compound. Yield: 0.1541 g (14%); ^{1}H NMR (400 MHz, DMSO-d_6, δ): 8.04 ppm (s, 2H, Ar H), 7.93 ppm (s, 1H Ar H), 3.35 ppm (s br, 6H), 2.32 ppm (s br, 3H); ^{19}F NMR (400 MHz, DMSO-d_6, δ): -61.46 ppm (s); ^{13}C NMR (400 MHz, DMSO-d_6, δ): 168.53 ppm (s), 141.17 ppm (s), 131.27 - 130.28 ppm (q, J = 33 Hz), 126.76 ppm (s), 124.04 ppm (s), 123.68 ppm (s br), 121.33 ppm (s), 118.53 ppm (s br), 99.26 ppm (s), 43.05 ppm (s), 16.35 ppm (s); HRMS calc. for $C_{12}H_{12}F_6N_2S$ $[M+H]^+$: 331.06, found: 331.0672 $[M+H]^+$

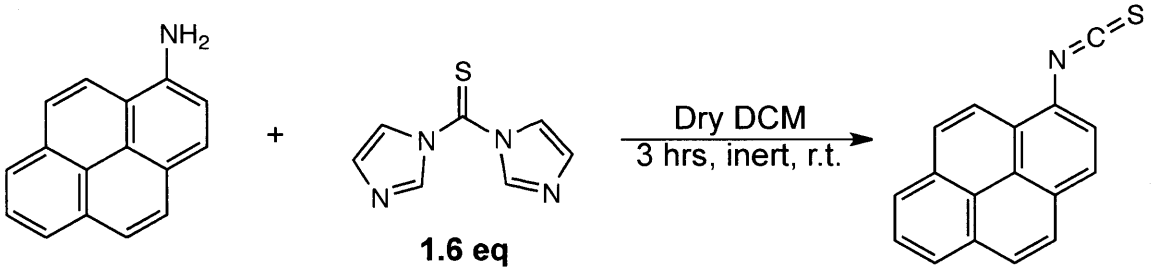

49%

1-isothiocyanatopyrene: A solution of 1-aminopyrene (0.2495g , 1.15 mmol) in dry dichloromethane (3 mL) was added dropwise over a span of 30 min to a solution of 1,1'-thiocarbonyldiimidazole (0.3192g , 1.79 mmol) in dry dichloromethane (8 mL) in an ice/water bath. The solution was warmed to room temperature and stirred for 3 h. The solvent was removed under reduced pressure. Warm hexane (6 x 10mL) was used to extract compound. The hexane solution was concentrated, passed the through a short silica gel column and eluted with hexane. Hexane was removed under reduced pressure and product was recrystallized in acetonitrile to yield a yellow solid compound. Yield: 0.1458g (49%); ^{1}H NMR (400 MHz, DMSO-d_6, δ): 8.22-8.19 ppm (m, 3H Ar H), 8.11 - 7.96 ppm (m, 5H, Ar H), 7.86 - 7.80 ppm (d, J = 8 Hz, 1H, Ar H); ^{13}C NMR (400 MHz, DMSO-d_6, δ): 130.91 ppm (s), 130.64 ppm (s), 129.93 ppm (s), 128.76 - 127.90 ppm (d, J = 86 Hz), 126.69 ppm (s), 126.59 ppm (s), 126.45 ppm (s), 125. 81 - 125.70 ppm (d, J = 12 Hz), 124.77 ppm (s), 124.66 ppm (s), 123.77 ppm (s), 123.53 ppm (s), 121.32 ppm (s); HRMS calc. for $C_{17}H_9NS$ [M^+]: 259.05, found: 259.0441 [M^+]

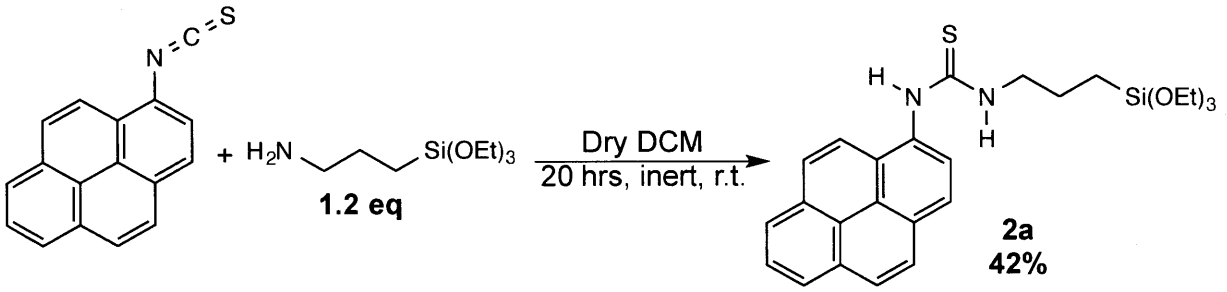

1-(pyren-1-yl)-3-(3-(triethoxysilyl)propyl)thiourea (2a):

1-isothiocyanatopyrene (47.3 mg , 0.18 mmol) was added dropwise to a stirring solution propylamine (43 μL , 0.21 mmol) in dichloromethane (1.25 mL) at room temperature. The mixture was stirred for 20 h. The solvent was removed under reduced pressure. The compound

was washed with hexane and extracted with ethyl acetate. Solution was dried under reduced pressure to yield a yellow solid compound. Yield: 36.5 mg (42%); ^{1}H NMR (400 MHz, DMSO-d_6, δ): 9.94 ppm (s, 1H), 8.33 - 8.01 ppm (m, 9H, Ar H), 7.59 ppm (s, 1H), 3.74 - 3.69 ppm (q, J = 6 Hz, 6H), 3.48-3.43 ppm (q, J = 7 Hz, 2H), 1.59 ppm (s br, 2H), 1.14-1.11 ppm (t, J = 7 Hz, 9H), 0.53 ppm (s br, 2H); ^{13}C NMR (400 MHz, DMSO-d_6, δ): 181.73 ppm (s), 132.19 ppm (s), 130.67 ppm (s), 130.48 ppm (s), 129.36 ppm (s), 127.49 ppm (s), 127.18 ppm (s), 127.08 ppm (s), 126.60 ppm (s), 126.41 ppm (s), 126.06 ppm (s), 125.39 ppm (s), 125.16 ppm (s), 124.61 ppm (s), 123.85 ppm (s), 122.38 ppm (s), 57.68 ppm (s), 46.81 ppm (s), 22.16 ppm (s), 18.19 ppm (s), 7.25 ppm (s); HRMS calc. for $C_{26}H_{32}N_2O_3SSi$ $[M+H]^+$: 481.19, found: 481.1978 $[M+H]^+$

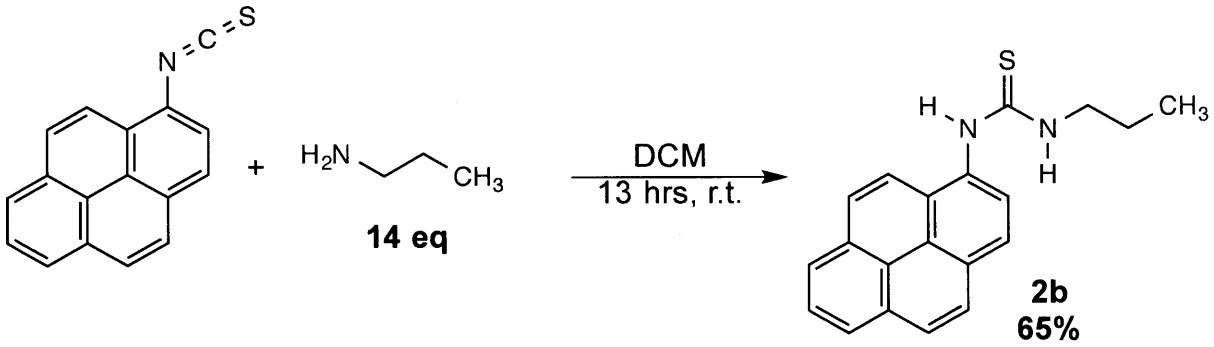

1-propyl-3-(pyren-1-yl)thiourea (2b):

1-isothiocyanatopyrene (42.8 mg , 0.17 mmol) was added dropwise to a stirring solution propylamine (200 μL , 2.43 mmol) in dichloromethane (2 mL) at room temperature. The mixture was stirred for 13 h. The solvent was removed under reduced pressure. The compound was washed with hexane and extract with ethyl acetate. The solution was dried under reduced pressure to yield a brown solid compound. Yield: 34.3 mg (65%); ^{1}H NMR (400 MHz, DMSO-

d_6, δ): 9.95 ppm (s, 1H), 8.32 - 8.03 ppm (m, 9H, Ar H), 7.70 ppm (s, 1H), 3.47 - 3.42 ppm (q, J = 7 Hz, 2H), 1.55 ppm (s br, 2H), 0.86 ppm (s br, 3H); ^{13}C NMR (400 MHz, DMSO-d_6, δ): 182.31 ppm (s), 132.87 ppm (s), 131.15 ppm (s), 130.97 ppm (s), 129.72 ppm (s), 127.92 ppm (s), 127.66 ppm (s), 127.49 ppm (s), 126.88 ppm (s), 126.49 ppm (s), 125.82 ppm (s), 125.61 ppm (s), 125.06 ppm (s), 124.33 ppm (s), 122.92 ppm (s), 46.43 ppm (s), 22.42 ppm (s), 11.83 ppm (s); HRMS calc. for $C_{20}H_{18}N_2S$ $[M+H]^+$: 319.12, found: 319.1241$[M+H]^+$

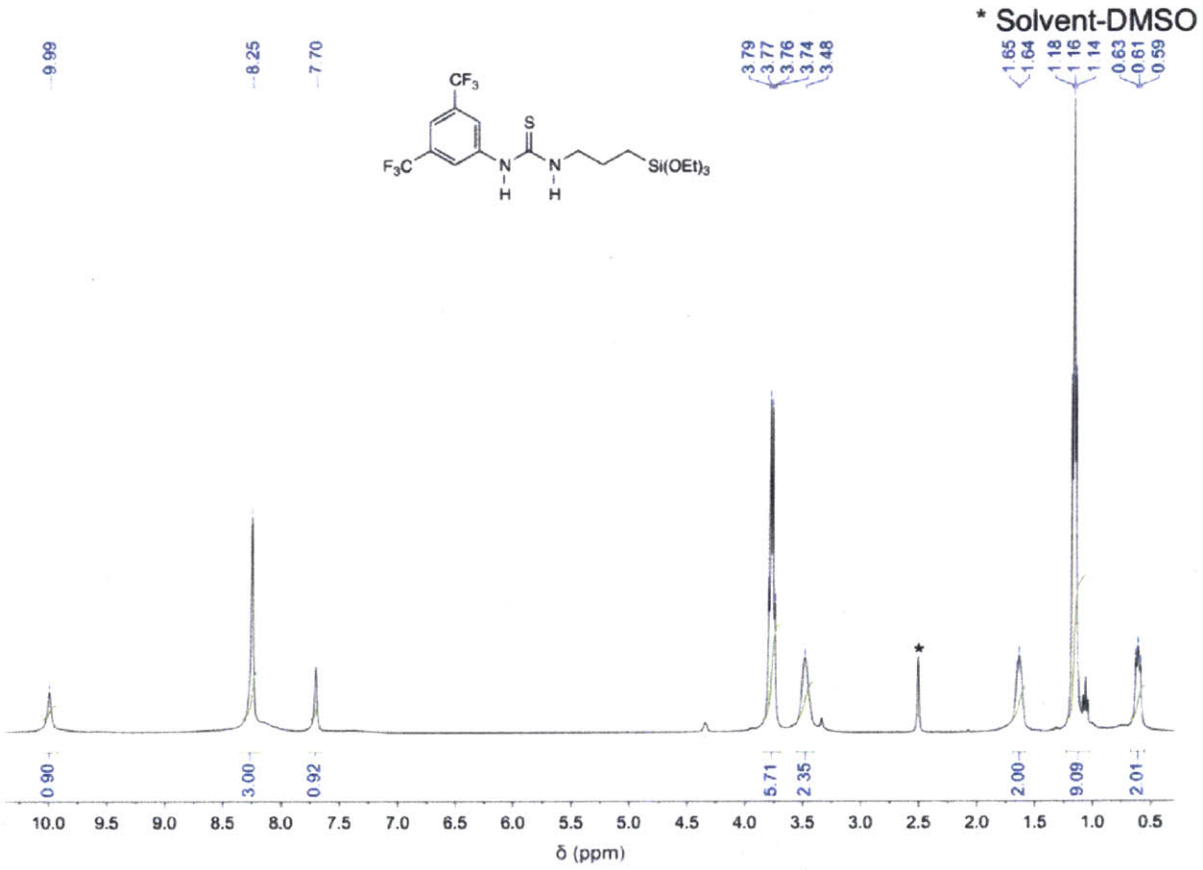

Figure A2.6. ^{1}H NMR spectrum of 1-(3,5-bis(trifluoromethyl)phenyl)-3-(3-(triethoxysilyl)propyl)thiourea (d^6-DMSO).

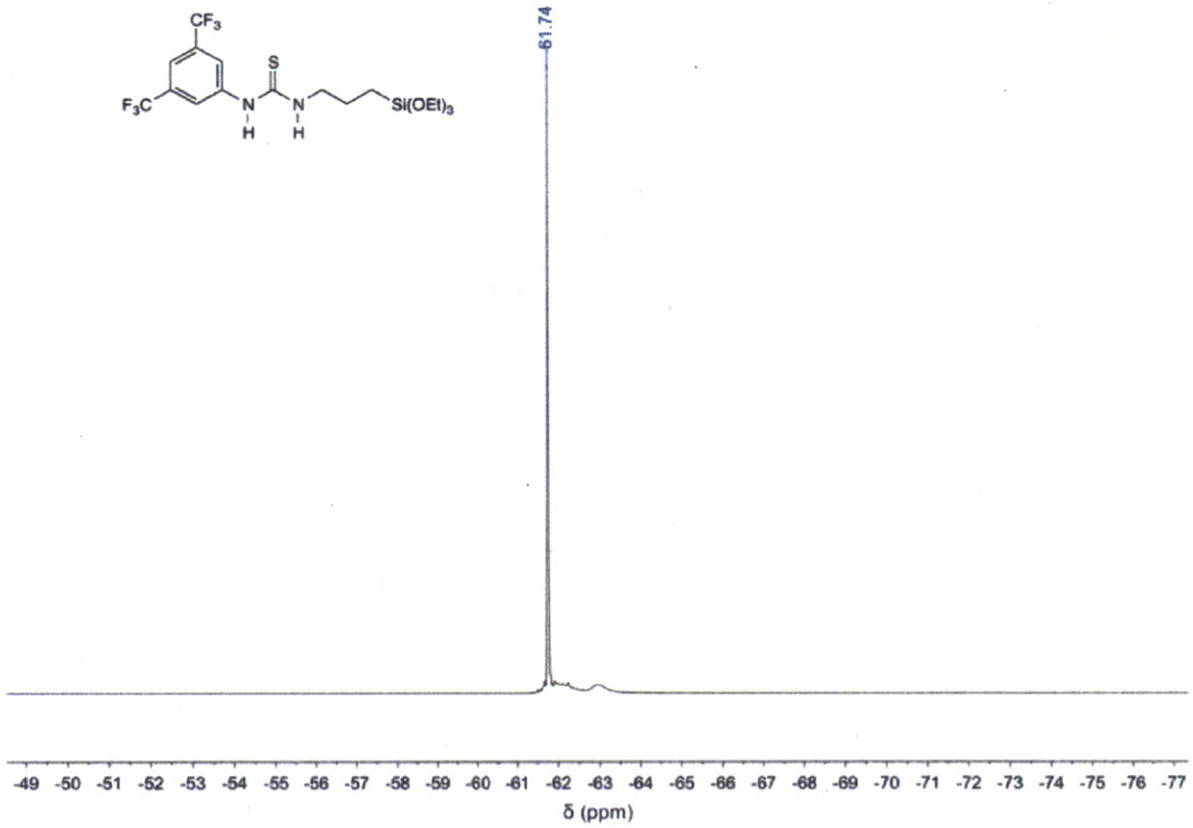

Figure A2.7. ^{19}F NMR spectrum of 1-(3,5-bis(trifluoromethyl)phenyl)-3-(3-(triethoxysilyl)propyl)thiourea (d^6-DMSO).

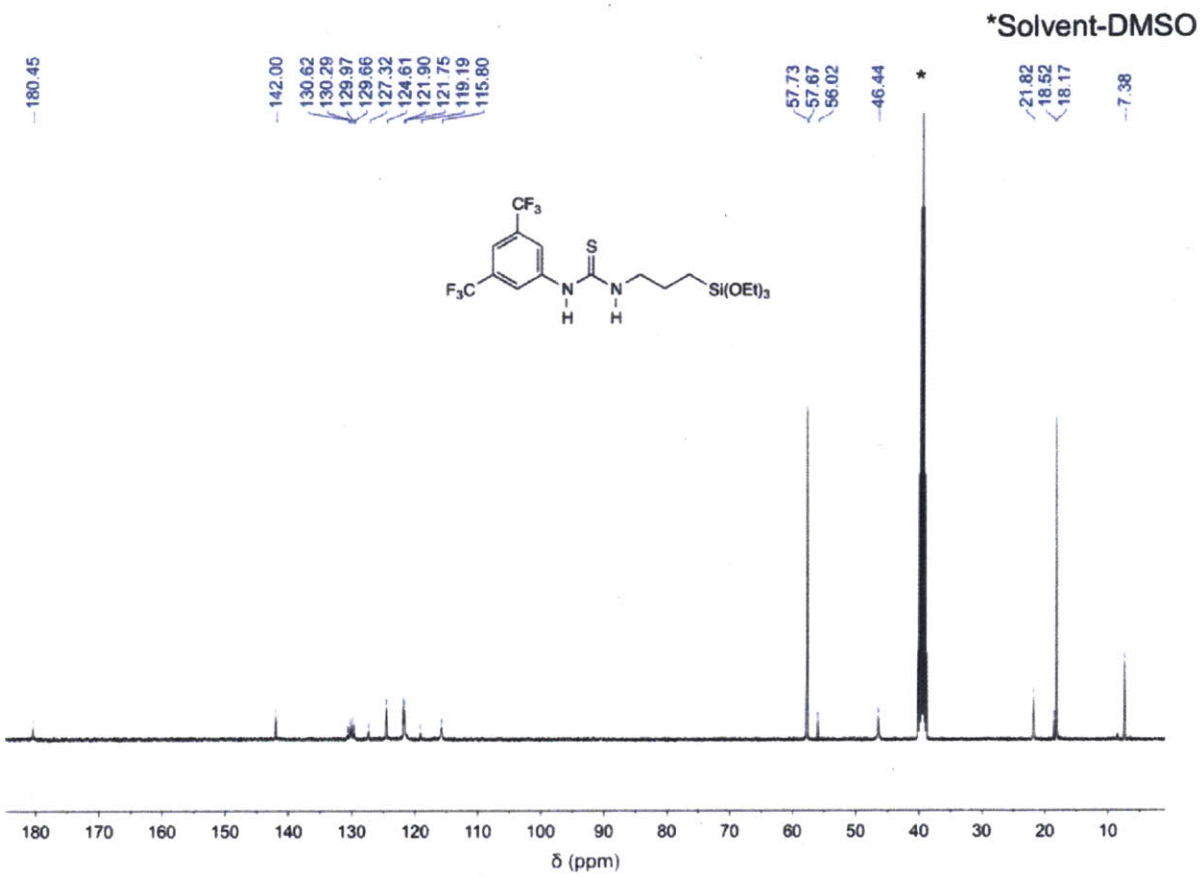

Figure A2.8. ^{13}C NMR spectrum of 1-(3,5-bis(trifluoromethyl)phenyl)-3-(3-(triethoxysilyl)propyl)thiourea (d^6-DMSO).

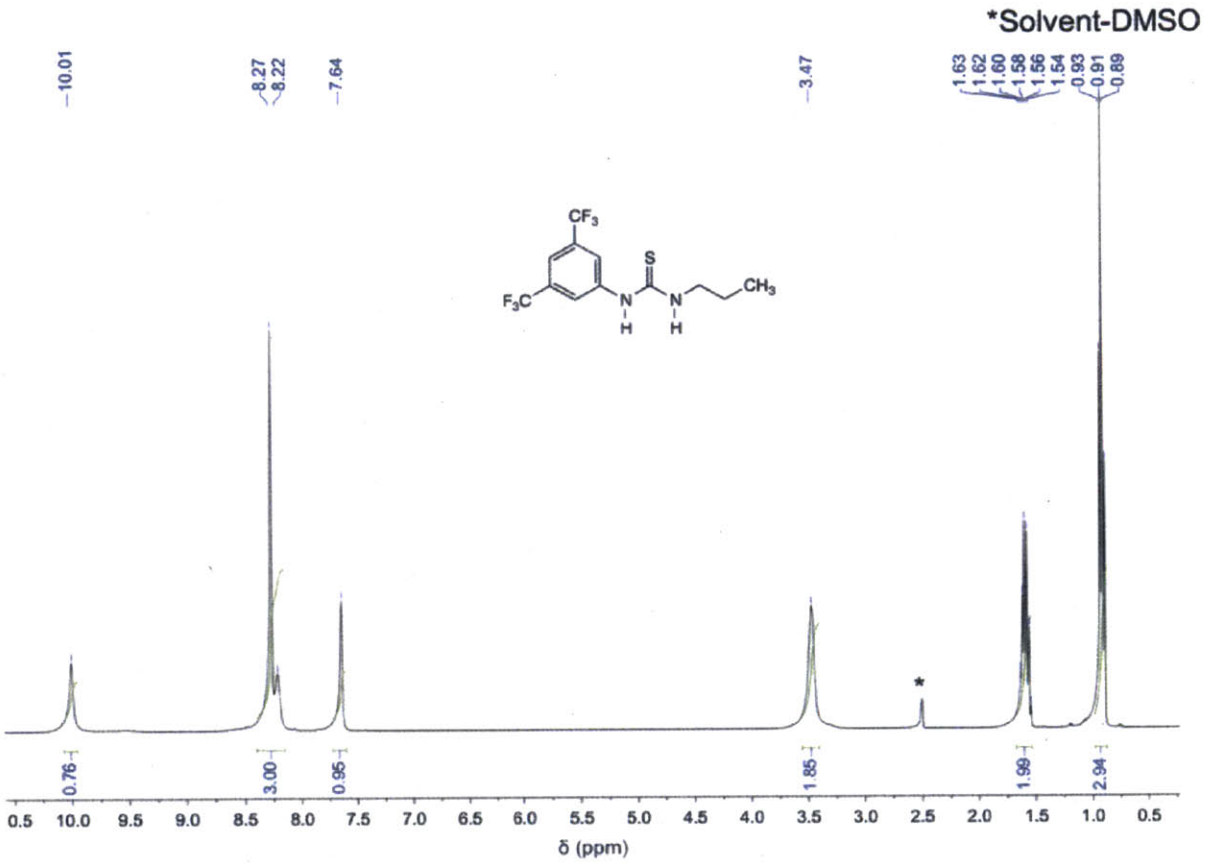

Figure A2.9. ^{1}H NMR spectrum of 1-(3,5-bis(trifluoromethyl)phenyl)-3-propylthiourea (d^6-DMSO).

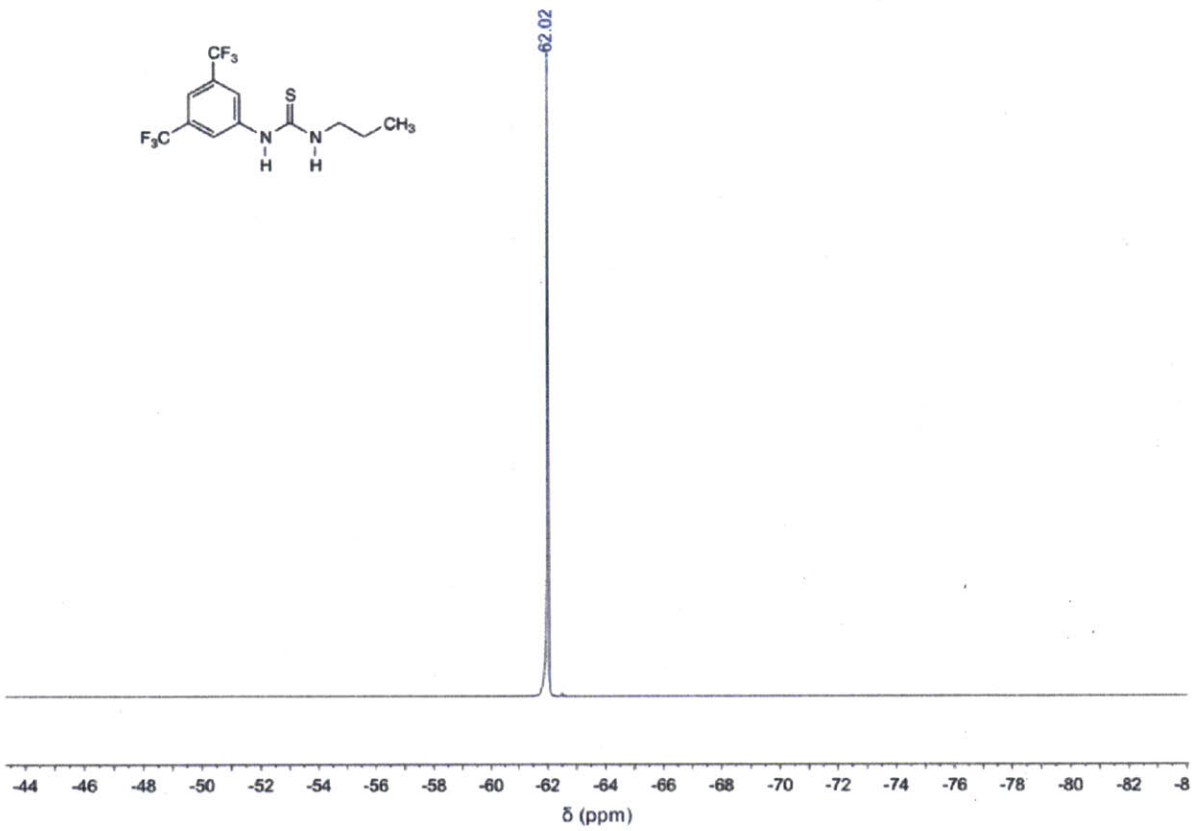

Figure A2.10. ^{19}F NMR spectrum of 1-(3,5-bis(trifluoromethyl)phenyl)-3-propylthiourea (d^6-DMSO).

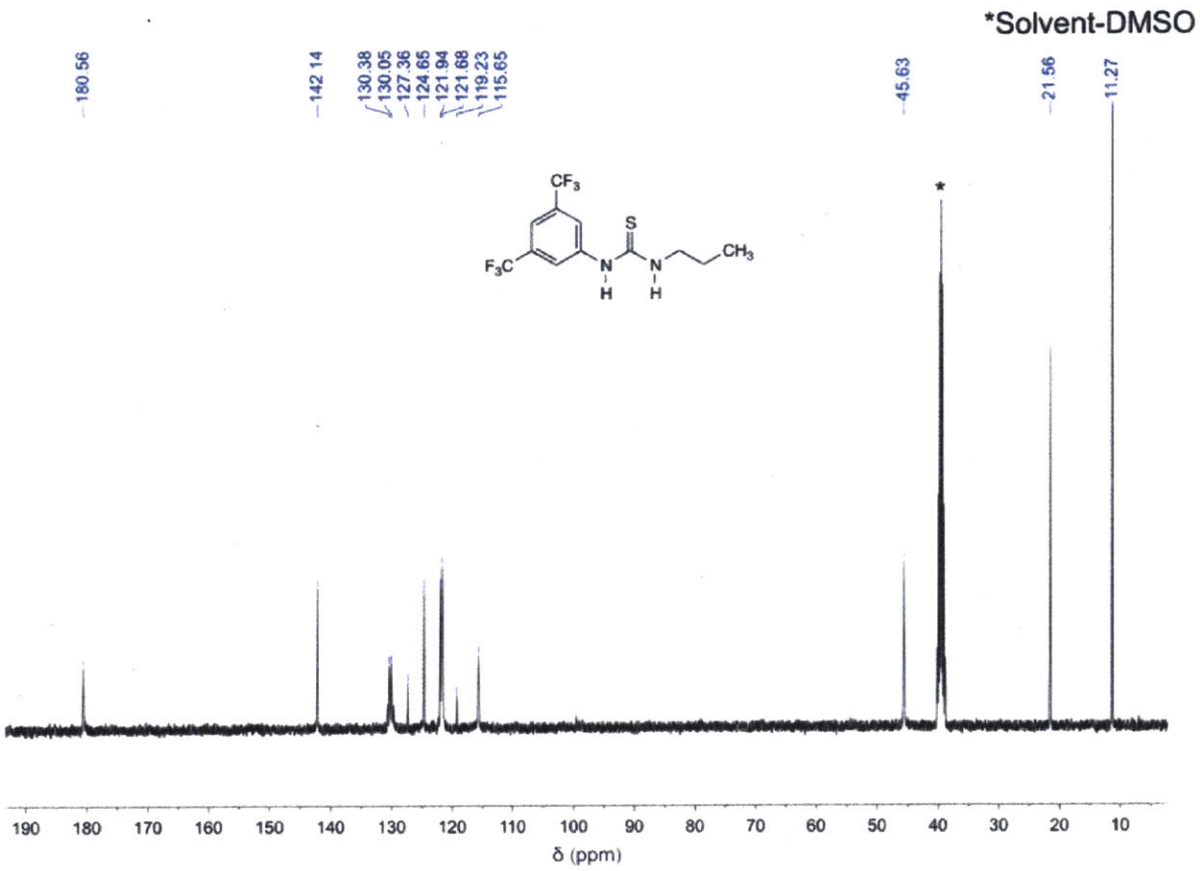

Figure A2.11. ^{13}C NMR spectrum of 1-(3,5-bis(trifluoromethyl)phenyl)-3-propylthiourea (d^6-DMSO).

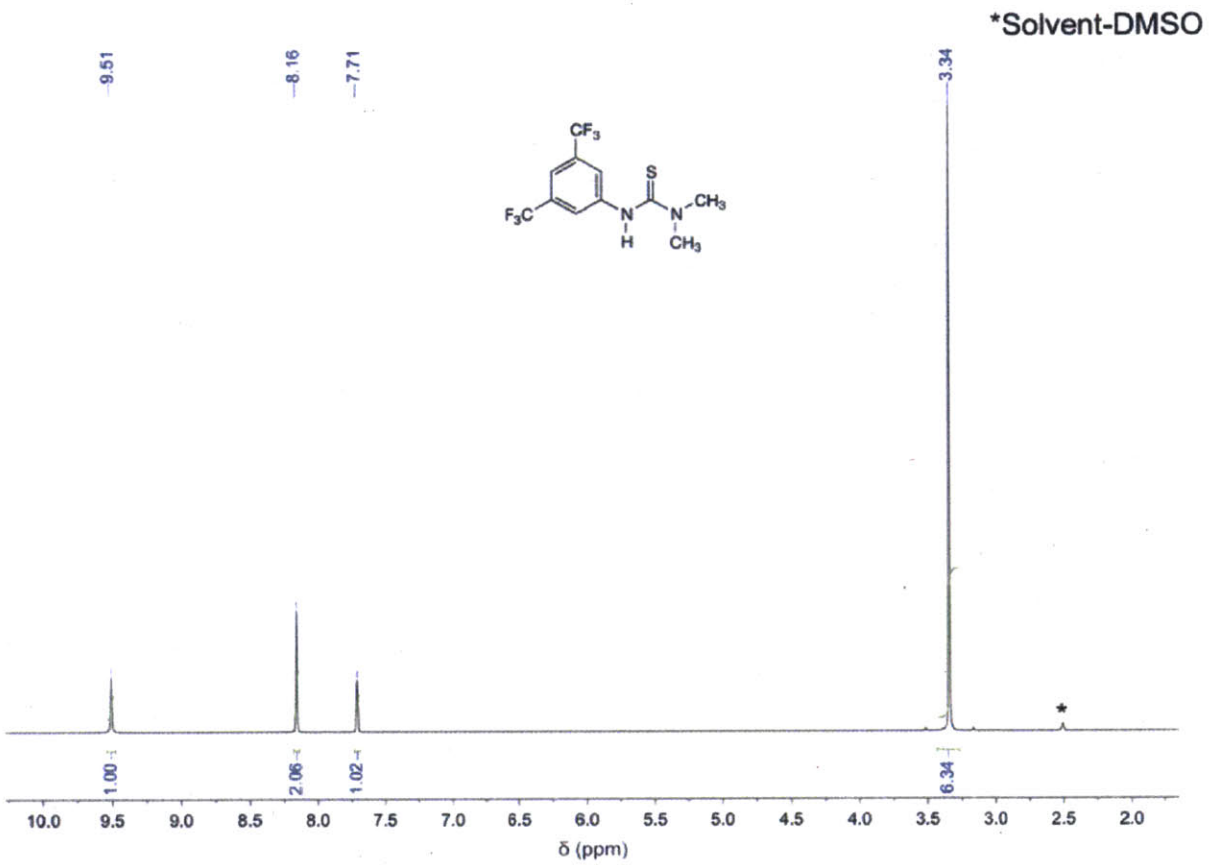

Figure A2.12. ^{1}H NMR spectrum of 3-(3,5-bis(trifluoromethyl)phenyl)-1,1-dimethylthiourea (d^{6}-DMSO).

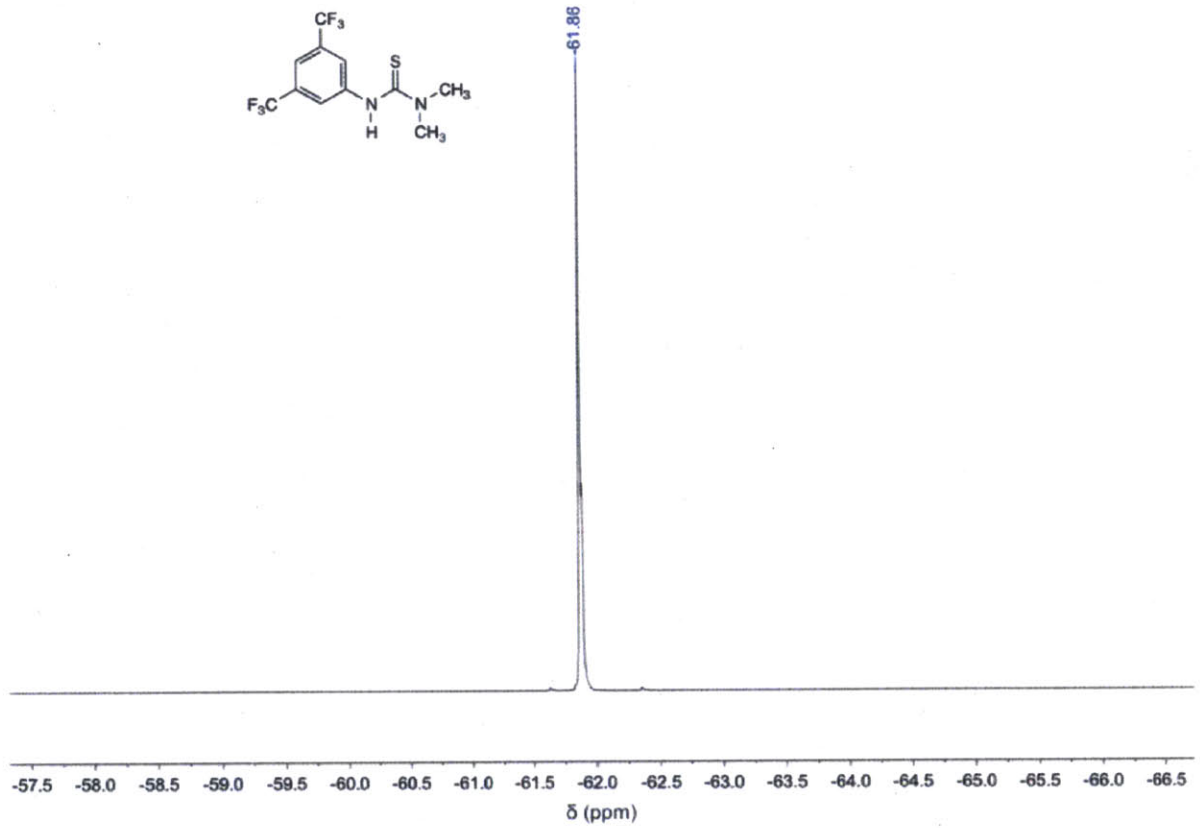

Figure A2.13. ^{19}F NMR spectrum of 3-(3,5-bis(trifluoromethyl)phenyl)-1,1-dimethylthiourea (d^6-DMSO).

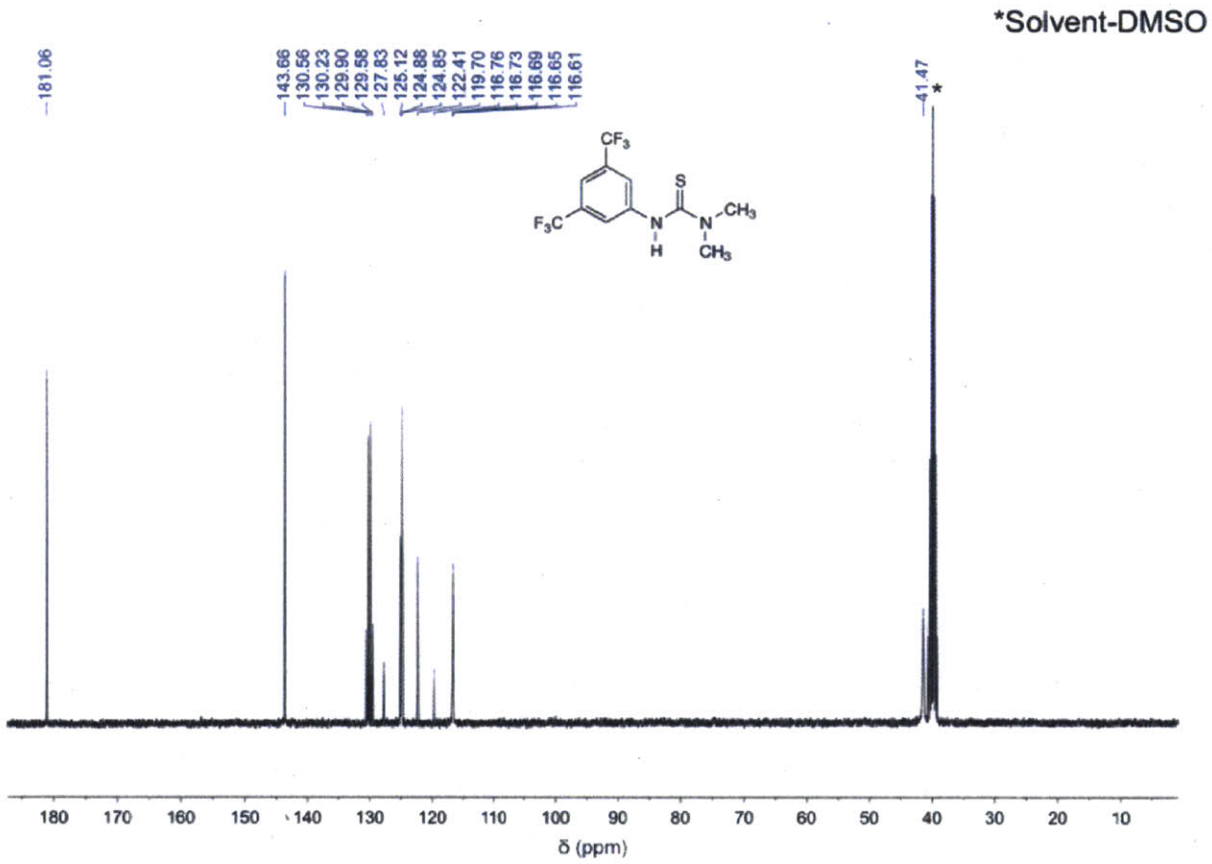

Figure A2.14. ^{13}C NMR spectrum of 3-(3,5-bis(trifluoromethyl)phenyl)-1,1-dimethylthiourea (d^6-DMSO).

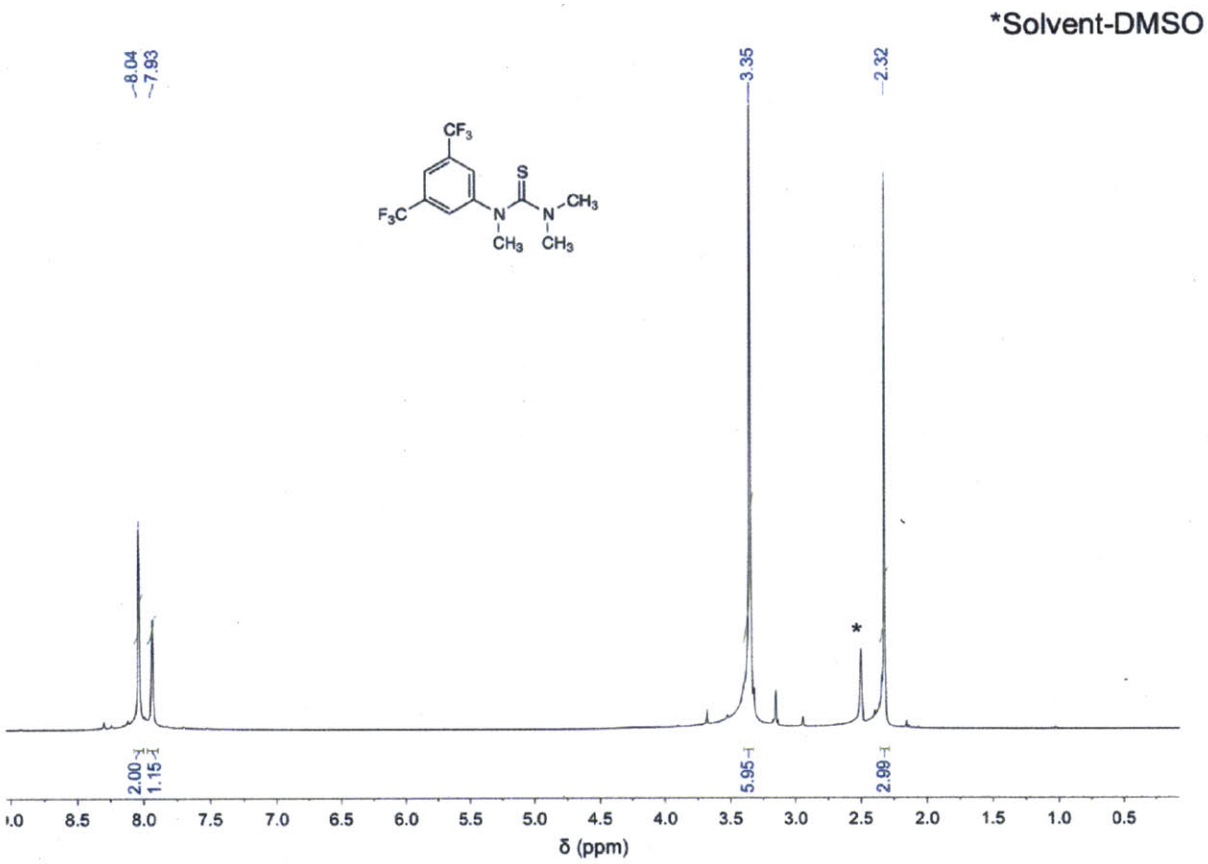

Figure A2.15. ^{1}H NMR spectrum of 1-(3,5-bis(trifluoromethyl)phenyl)-1,3,3-trimethylthiourea (d^{6}-DMSO).

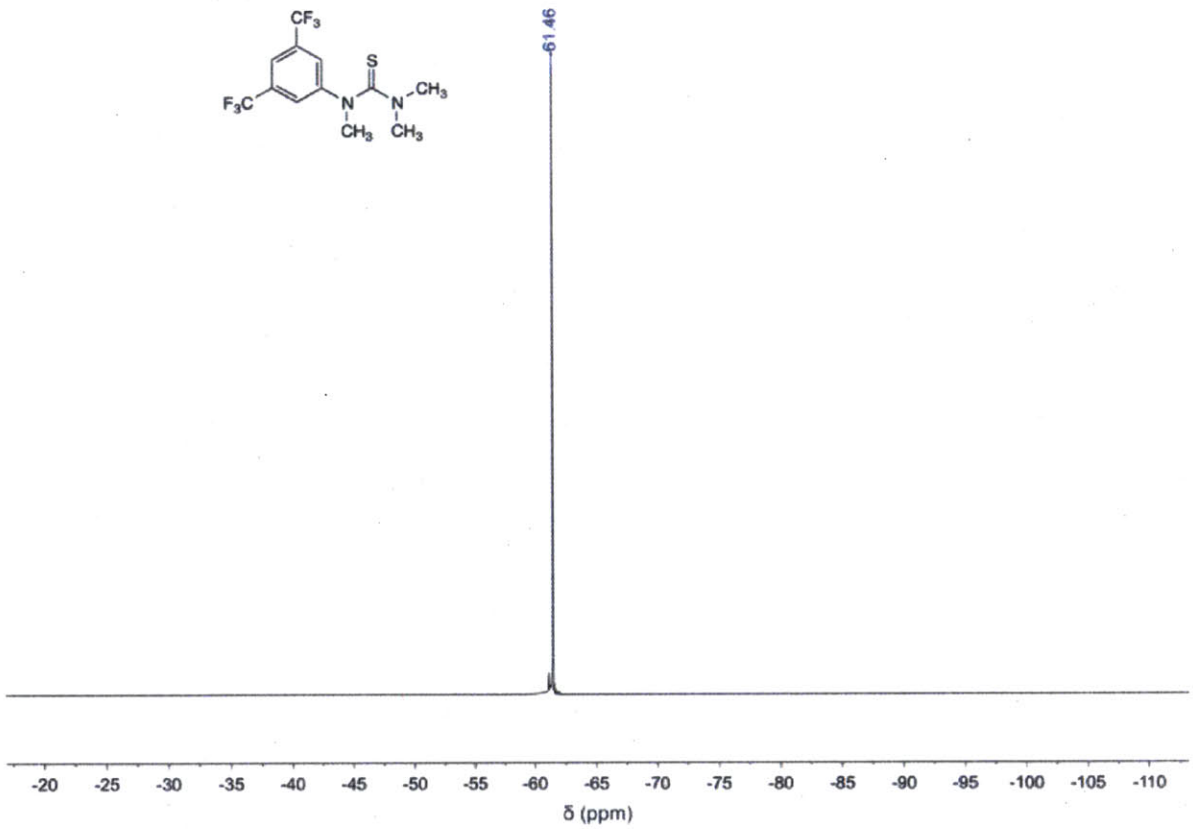

Figure A2.16. ^{19}F NMR spectrum of 1-(3,5-bis(trifluoromethyl)phenyl)-1,3,3-trimethylthiourea (d^6-DMSO).

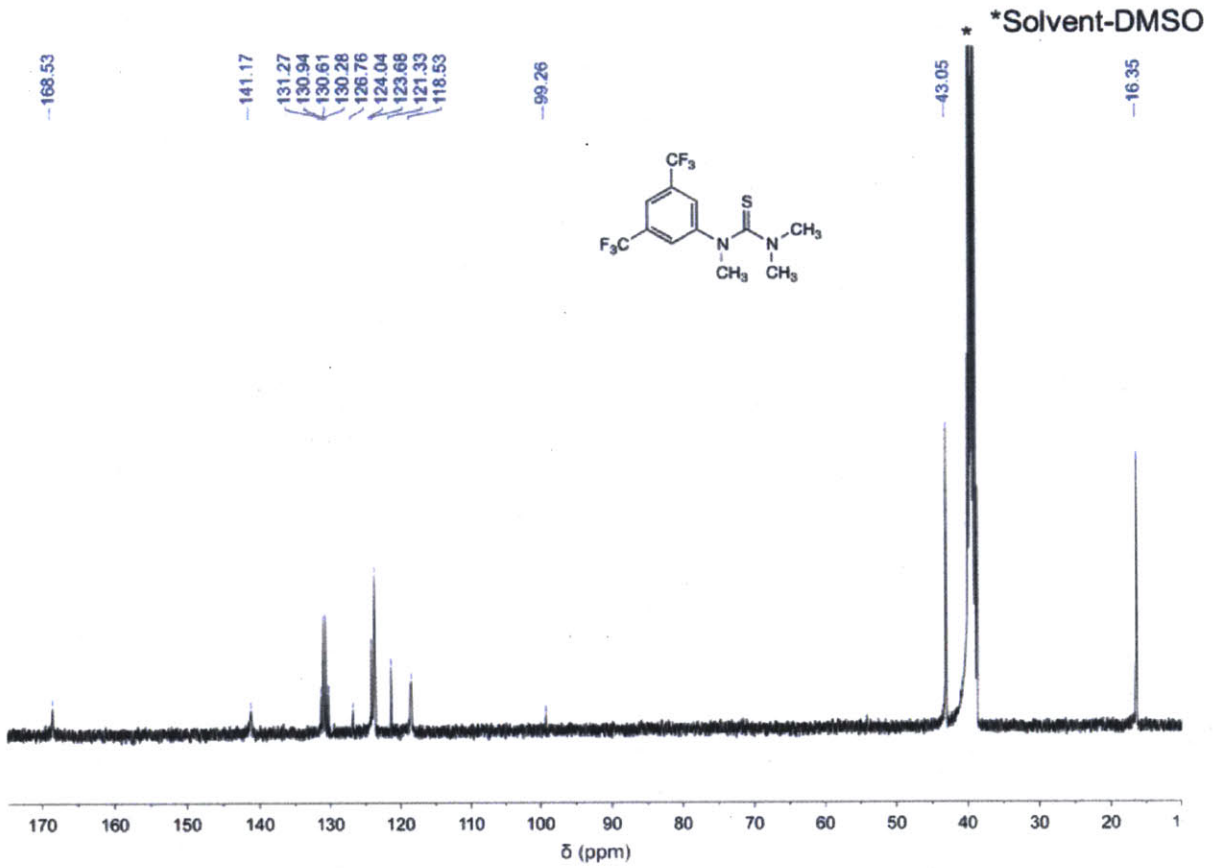

Figure A2.17. ^{13}C NMR spectrum of 1-(3,5-bis(trifluoromethyl)phenyl)-1,3,3-trimethylthiourea (d^6-DMSO).

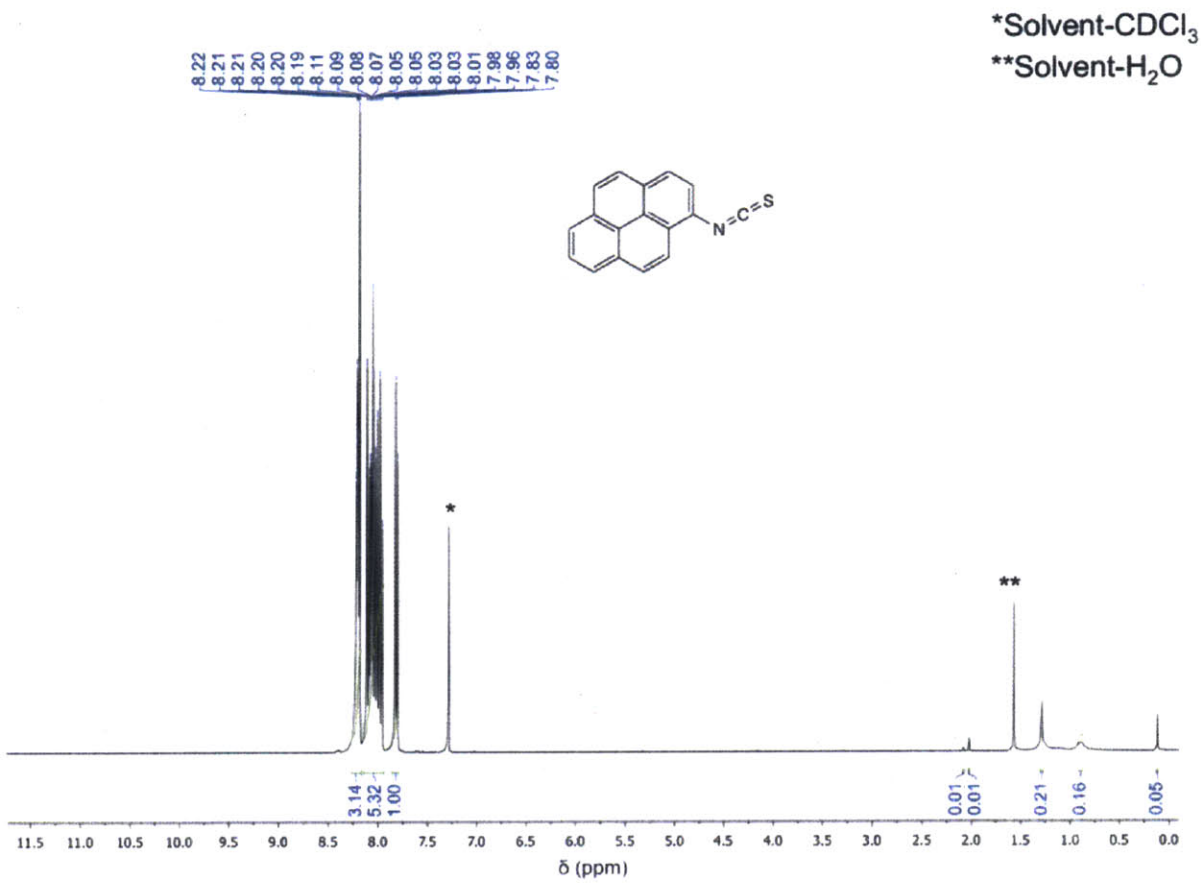

Figure A2.18. ^{1}H NMR spectrum of 1-isothiocyanatopyrene (d^6-$CDCl_3$).

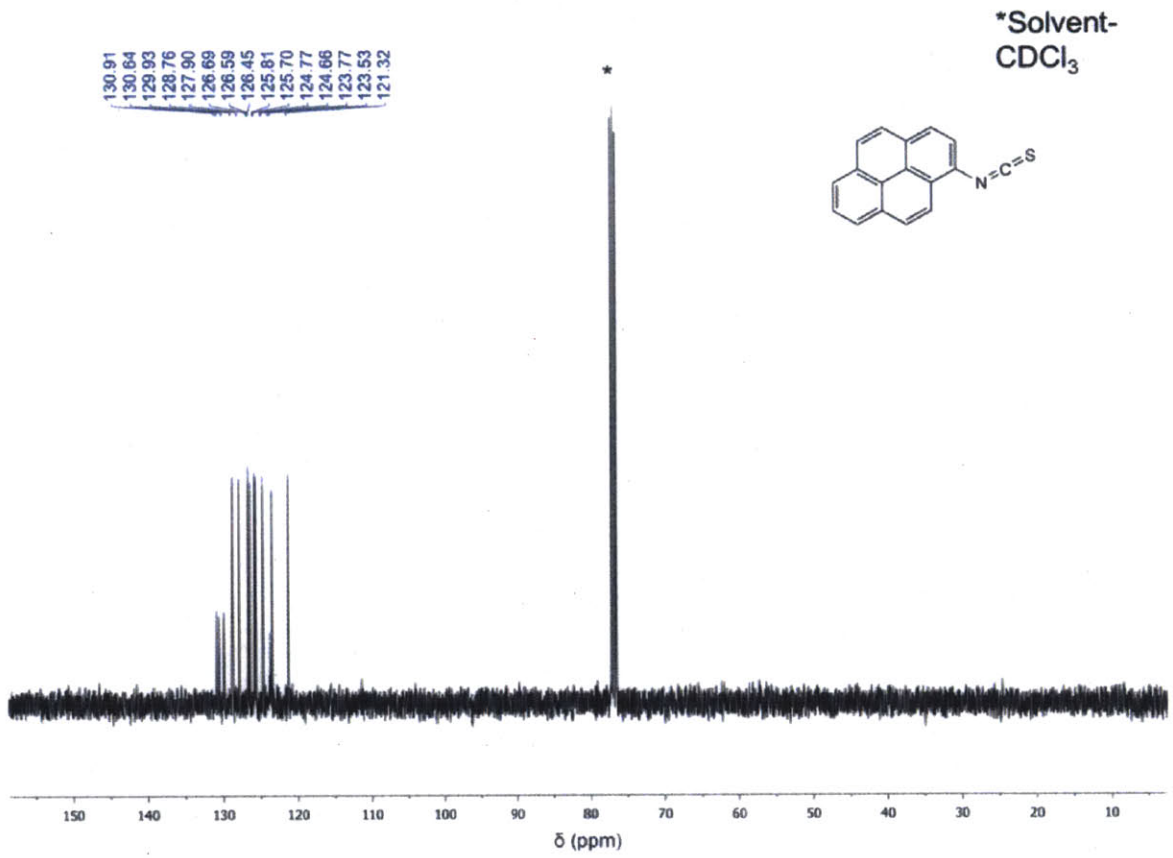

Figure A2.19. ^{13}C NMR spectrum of 1-isothiocyanatopyrene (d^6-$CDCl_3$).

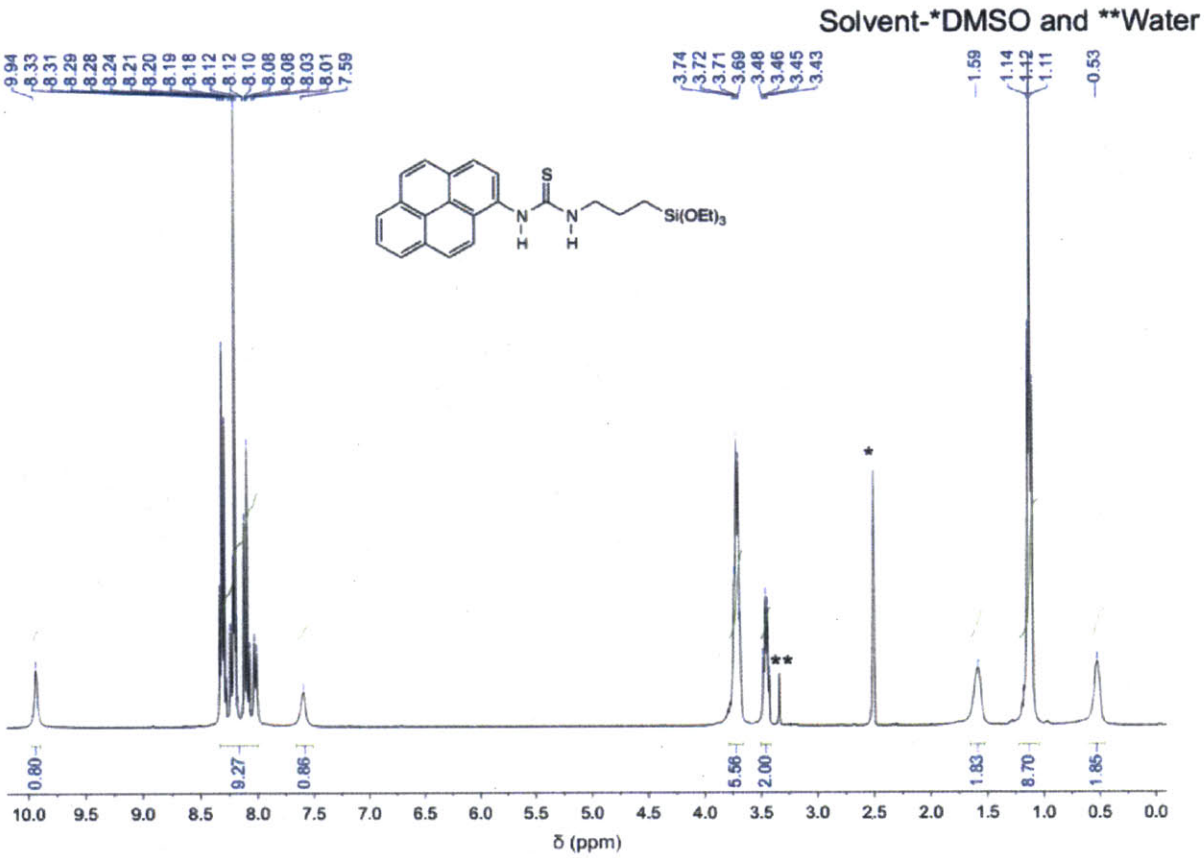

Figure A2.20. ^{1}H NMR spectrum of 1-(pyren-1-yl)-3-(3-(triethoxysilyl)propyl)thiourea (d^6-DMSO).

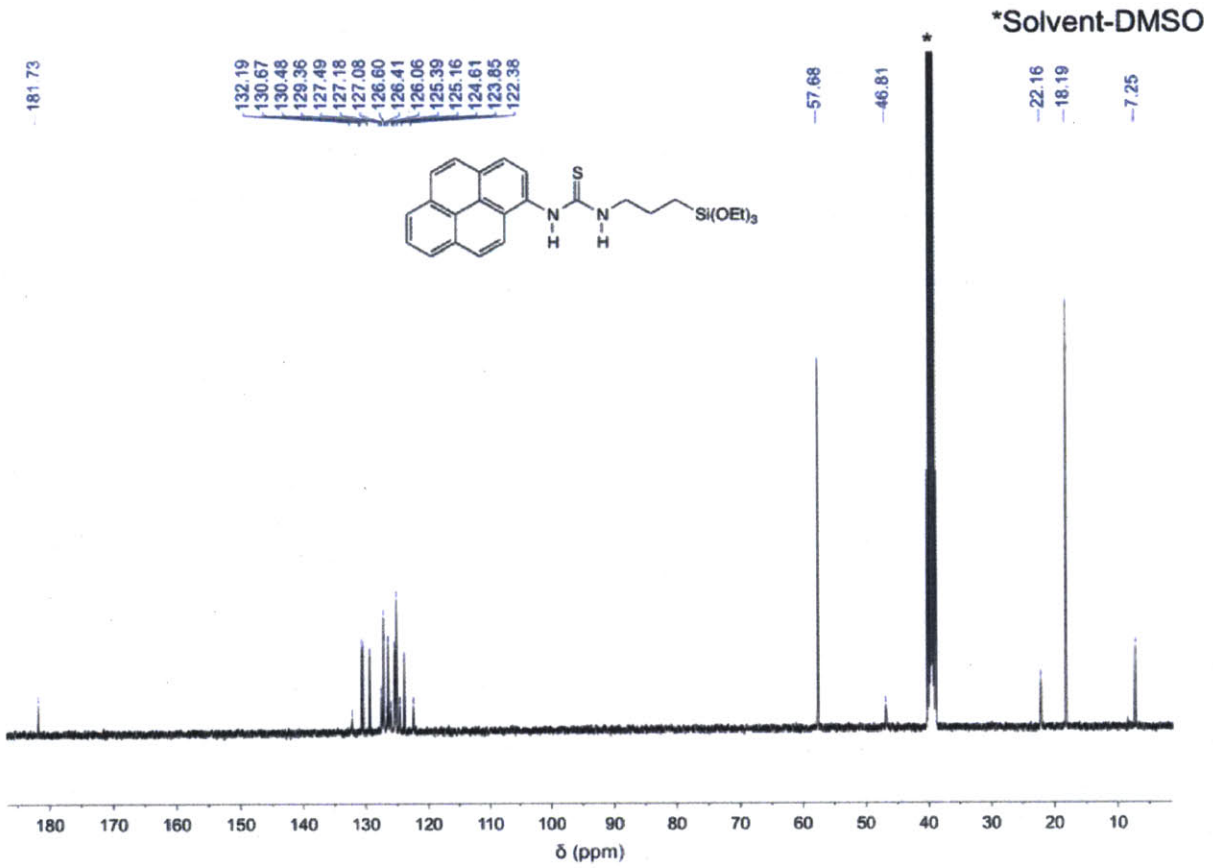

Figure A2.21. ^{13}C NMR spectrum of 1-(pyren-1-yl)-3-(3-(triethoxysilyl)propyl)thiourea (d^6-DMSO).

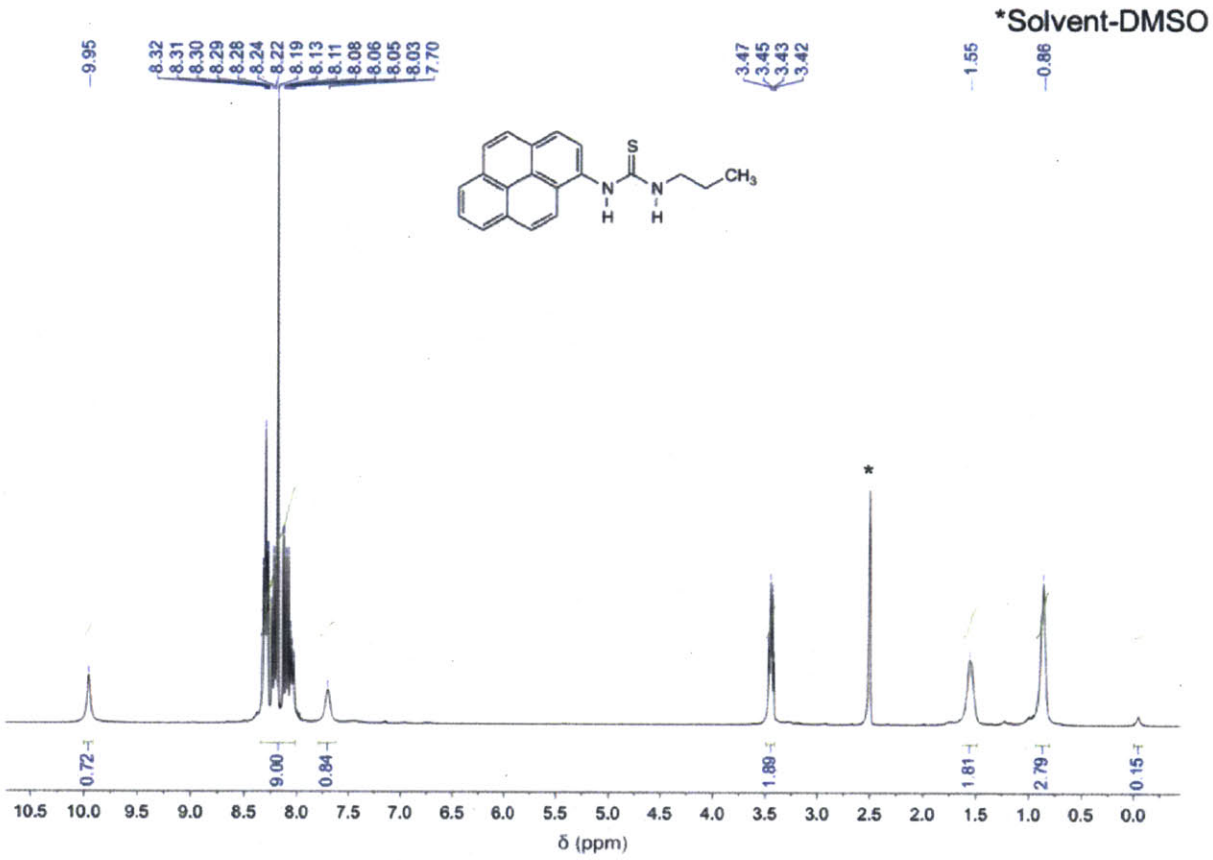

Figure A2.22. ^{1}H NMR spectrum of 1-propyl-3-(pyren-1-yl)thiourea (d^6-DMSO).

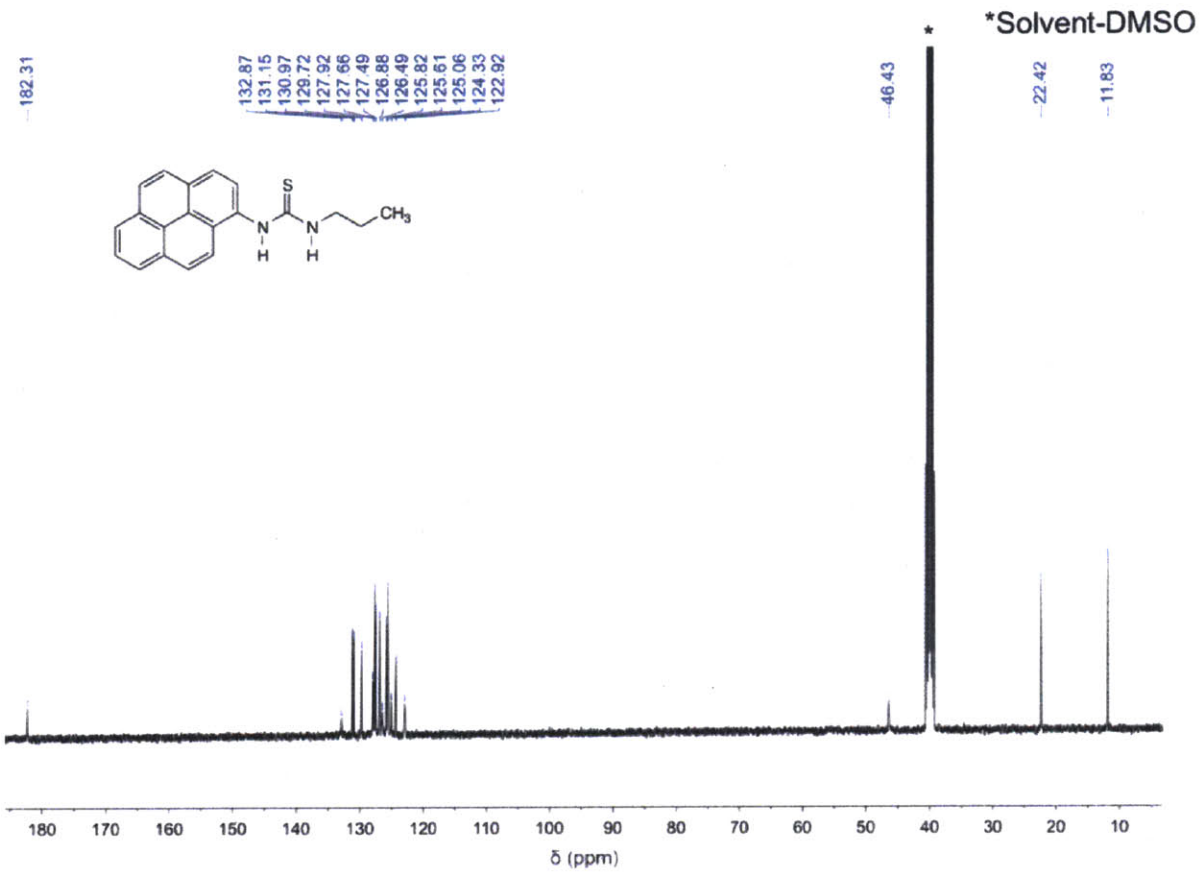

Figure A2.23. ^{13}C NMR spectrum of 1-propyl-3-(pyren-1-yl)thiourea (d^6-DMSO).

Chapter 3

Fully-drawn carbon-based chemical sensors on organic and inorganic surfaces

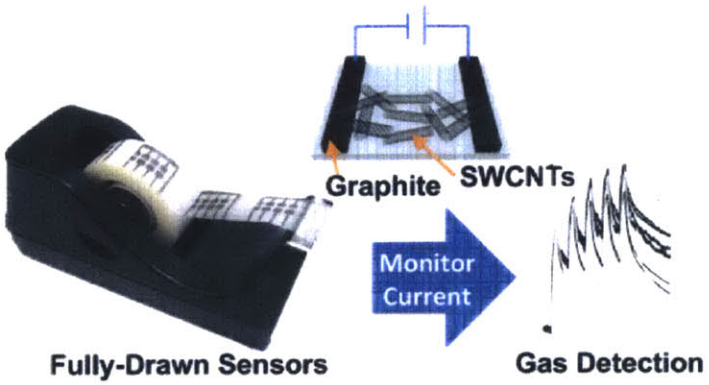

Adapted from: Frazier, K.M.; Mirica, K.A.; Walish, J.J.; Swager, T.M. "Fully-drawn carbon-based chemical sensors on organic and inorganic surfaces," *Lab Chip*, **2014**, 14, 4059-4066.

Dr. Katherine Mirica fabricated devices as User-1 in Figure A3.14 and provided thoughtful discussions and feedback for the development of this chapter. Dr. Joseph Walish is responsible for laser-etching the substrates and the data in Table A3.2.

3.1 Introduction

Chemical sensors that identify and monitor volatile organic compounds (VOCs) have an important role in assessing public security, food and water quality, industrial environment, and health.[1-7] For example, it would be useful to detect residual volatile organic compounds (VOCs) in consumer goods such as food,[8, 9] shelter,[9, 10] clothing,[11] and medicine[9] and to protect workers from occupational exposure. Presently, the monitoring and determination of the chemical components of gas samples is typically done using gas chromatography-mass spectrometry (GC-MS).[10–13] This technique, although highly sensitive and selective, has the disadvantages of limited portability, high cost, and requirement of highly trained users.

Carbon nanotubes (CNTs), are useful materials in chemical sensing as a result of the sensitivity of their electrical conductance to the presence of chemical analytes.[3, 5, 14] A productive route to enhancing the selectivity and sensitivity of these materials to specific analytes is covalent or non-covalent functionalization with polymers, metals, or small molecules.[15–25] Straightforward integration of these materials into devices on various substrates can yield simple, portable, and low-power sensors and arrays capable of detecting and differentiating a wide variety of vapors at parts-per-million (ppm) concentrations.[16, 17, 19, 20, 22, 23, 26–32]

The fabrication of sensing devices by printing,[33–38] dip coating,[36, 38, 39] drop casting,[40] photolithography,[41] or drawing[34–39, 42–44] has advantages of being simple and low-cost without the need for highly specialized facilities. Drawing is particularly attractive because it directly deposits carbon-based solid composite materials that require no solution-phase processing.[33, 34, 36, 38, 42, 43] Recently, we[42, 43] and others[33, 34, 38] have developed methods for the

fabrication of carbon-based sensors on the surface of paper by drawing. Taken together, these methods are capable of producing functional chemiresistors,[34, 38, 42, 43] electrochemical sensors,[36, 38] strain and pressure sensors,[34] and simple electrodes[35, 36, 38, 39, 44] from commercially available starting materials within minutes. Although the abrasive deposition of solid sensing materials on the surface of cellulose paper has made the fabrication of chemical sensors from carbon nanomaterials simple, solvent-free, and easily accessible, there are limitations to this method. The location, size, thickness, and distribution of the resulting conductive carbon "film" is difficult to control and limited by the features of the substrate (*e.g.*, surface roughness and distribution of cellulose fibers on the surface of paper).

Herein we describe a rapid, scalable, portable, and cost-effective approach for the on-demand fabrication of fully-drawn chemical sensing arrays on a variety of different substrates (*e.g.*, paper, plastic, and undoped silicon wafer). This approach is entirely solvent-free, requires only small amounts of sensory materials, and is capable of producing highly-sensitive chemical sensors. We demonstrate this approach in the context of sensing and differentiating a variety of nitrogen-containing vapors at ppm concentrations. Our demonstration employs solid composites of single-walled carbon nanotubes (SWCNTs) with small molecules as the sensing material and graphite as electrodes. We utilize a previously established method[43] to generate sensing materials, or PENCILs (Process Enhanced NanoCarbon for Integrated Logic), by the mechanical mixing of SWCNTs with commercially available small molecules (solid or liquid). We then utilize DRAFT (Deposition of Resistors with Abrasion Fabrication Technique) to deposit these materials on a variety of substrates. Sequential deposition by mechanical abrasion of sensing materials and commercial graphite pencils on selected etched (weighing paper and PMMA) and

non-etched (silicon wafer and adhesive tape) substrates yields precisely fabricated fully-drawn chemiresistive sensing arrays (Figure 3.1).

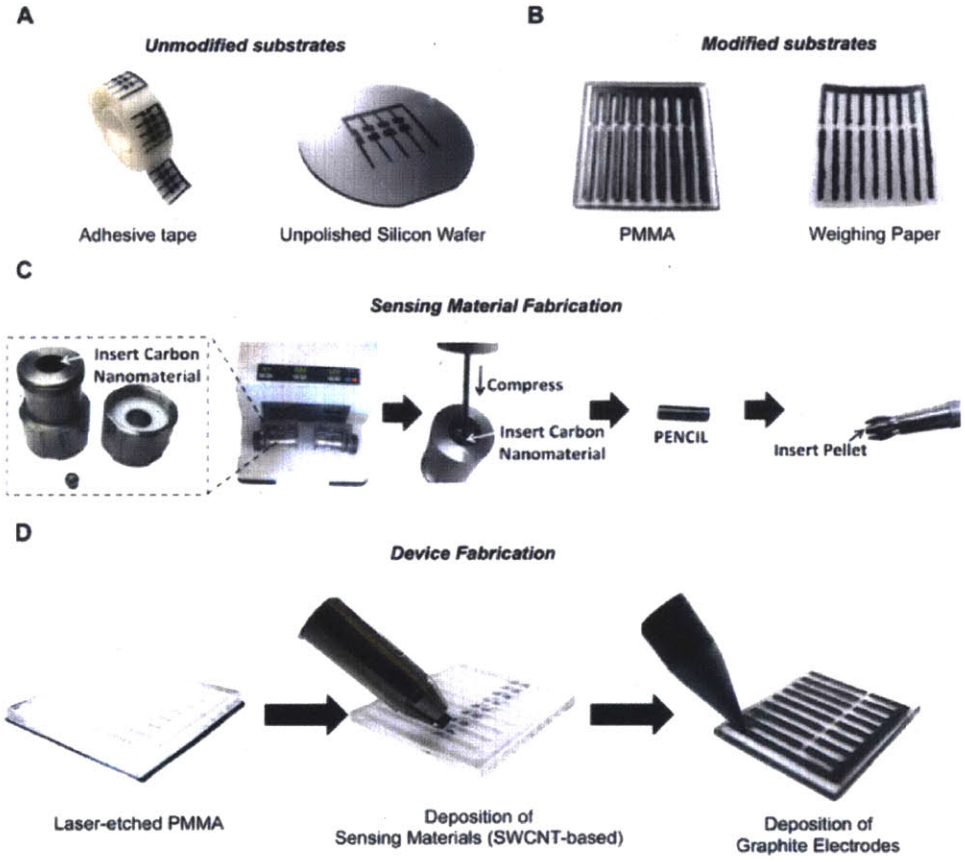

Figure 3.1. Fabrication of chemiresistive chemical sensors by drawing. Sensing materials (SWCNT-based) and graphite as electrodes were both deposited by mechanical abrasion to yield fully-drawn, chemiresistive gas-sensors on various A) unmodified substrates such as adhesive tape and unpolished silicon wafer, and B) laser-etched substrates such as PMMA and weighing paper. C) Fabrication of the sensing material consists of mechanically mixing and compressing SWCNT composites into a pellet. D) Stepwise fabrication of fully-drawn chemiresistive sensors on PMMA.

3.2 Results and Discussion

3.2.1 Partially-drawn sensors: mechanical abrasion of only chemiresistive materials

The successful stepwise fabrication of fully-drawn chemiresistive sensors consist of two separate deposition steps: deposition of sensing materials (SWCNTs) and deposition of electrodes (graphite). In order to measure the performance of each deposition step separately, we fabricated partially-drawn sensors where we evaluated compatibility of various substrates with DRAFT, and then selected four substrates to demonstrate the performance and versatility of the fully-drawn sensors.

Partially-drawn sensors were made by depositing sensing materials by mechanical abrasion (SWCNT:selector) between and on top of gold electrodes on six different substrates: weighing paper, glass, silicon, alumina, polymethyl methacrylate (PMMA), and adhesive tape. To evaluate the sensory performance of each device, we used pyridine (an industrial hazard[9]) as a model analyte. To increase the response of the SWCNTs to pyridine vapor we chose to make SWCNT composites with triethyl citrate (TEC), which is a commercial, nontoxic, colorless, and odorless liquid used as a food additive and plasticizer.[45] Mechanical mixing and compression of SWCNTs with TEC can coat and disperse SWCNTs within a solid composite of a PENCIL and enable hydrogen-bonding interactions between the hydroxyl groups of TEC and the lone pair of pyridine, thus enhancing the sensitivity of the SWCNT/TEC composite towards pyridine. These PENCILs are stable under ambient conditions and can be used to produce devices over the course of at least two months without any decrease in sensory performance (Figure A3.7).

To establish compatibility of substrates with DRAFT we fabricated devices by abrading a composite of SWCNTs and TEC (2:1 wt. ratio) onto six different substrates equipped with gold electrodes (1 mm gap size). The resulting devices generated significant changes in conductance

when exposed to 50 ppm pyridine vapor under a constant bias (50 mV). Figure 3.2A displays normalized conductance traces of devices exposed five consecutive times to 50 ppm pyridine for 30 s with 60 s recovery time on six different substrates. The functionalized CNT chemiresistors have a semi-reversible response towards pyridine for all devices. The first exposure provided the largest response consistently. By exempting the first exposure we lower the coefficients-of-variance of our sensors in response to 50 ppm pyridine between 2–16% (Table A2.1).

To investigate the dynamic sensing range of the substrates, devices were exposed to various concentrations of pyridine (1–550 ppm) for five consecutive cycles of 30 s exposures with 60 s recovery times (Figure 3.2B & C). The first exposure to pyridine was excluded from the device's average normalized conductance response as a result of its irreversibility and large variability (~10% coefficient-of-variance at 50 ppm pyridine on weighing paper). The sensors from each substrate can successfully detect pyridine at its permissible exposure limit (1 ppm: American Conference of Governmental Industrial Hygienists [ACGIH]) and discriminate it from higher values (*e.g.*, 20 ppm) (Fig. A3.16). Five of the six substrates examined demonstrated a similar magnitude (at 50 ppm pyridine: $\Delta G/G_0 =$ 5.2–8.3%) of the conductive response towards pyridine. The sixth substrate, glass, was characterized by the poorest sensing performance (at least 2 times lower) across the range of concentrations examined.

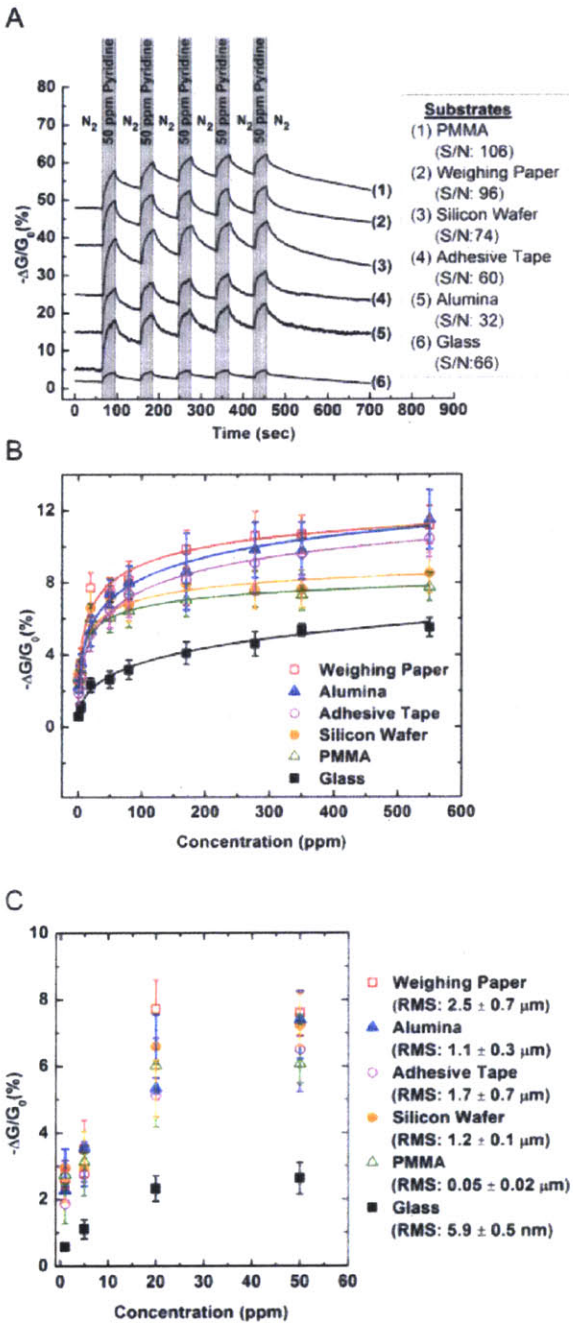

Figure 3.2. Mechanical deposition of sensing materials on six different substrates. A) Comparison of changes in conductance of sensing materials deposited on six different substrates in response to five consecutive exposures to 50 ppm pyridine. B–C) The average normalized conductance response (first exposure exempt) of at least six sensors on each substrate upon five consecutive exposures to various concentrations of pyridine for 30 s with 60 s recovery time.

We used profilometry to investigate the surface morphology of the six substrates. From these data we were able to calculate the root-mean-square (RMS) surface roughness of weighing paper (RMS = 2.5 ± 0.7 μm), alumina (RMS = 1.1 ± 0.3 μm), adhesive tape (RMS = 1.7± 0.7 μm), unpolished side of the undoped silicon wafer (RMS = 1.2 ± 0.1 μm), PMMA (RMS = 0.05 ± 0.02 μm), and glass (RMS = 5.9 ± 0.5 nm). The abrasion of the SWCNT/TEC PENCIL on glass was both challenging and produced non-uniform and poorly distributed films of nanotubes as a result of the hardness and smoothness of the substrate. In order to facilitate the deposition of PENCILs by abrasion on smooth surfaces, we modified substrates (PMMA and glass) by laser or chemical etching. However, the laser-etched glass did not facilitate improved deposition of materials by DRAFT as a result of surface artifacts and cracks on the surface of the glass that we introduced by the etching process (Figure A3.4).

3.2.2 Graphite electrodes by mechanical abrasion

After investigating DRAFT on various substrates, we endeavoured to produce electrodes by abrasion to yield a fully-drawn CNT-based chemiresistive array. To facilitate the successful design of a fully-drawn chemiresistor, it is imperative that the electrodes of the sensor are substantially more conductive and largely inert to the chemical analytes. To explore this requirement, we compared the response of pristine SWCNTs to the response of a commercial 9B graphite pencil when both were abraded between gold electrodes on the surface of weighing paper (3 sensors each) and exposed to various analytes. The resistive range of the sensors was 1–2 kΩ. The sensing response of graphite was 5 times smaller in response to 277 ppm pyridine than the response of pristine SWCNTs (Figure A3.12). This study suggests that SWCNTs are much

more sensitive materials than graphite towards a wide range of chemical analytes, a difference that should be amplified even further when the sheet resistance of graphite electrodes within a chemiresistor architecture is substantially lower than that of SWCNT-based sensing materials.

3.2.3 Fabrication of fully-drawn chemical sensors

Fully-drawn sensors have the advantage of being easily fabricated on-demand or replaced. We demonstrate the fabrication and characterize sensing performance of fully-drawn chemical sensors on four different substrates (Figure 3.3). We implement a two-step fabrication process to generate fully-drawn working devices (Figure 3.3A–B) on the unmodified surface of adhesive tape and an unpolished undoped highly resistive (resistance >10000 Ω cm) silicon wafer. The first step involves drawing a line of sensing material (SWCNT:TEC) approximately 3 mm in length having a resistance of 400–600 kΩ. The second step then generates carbon-based electrodes by abrasion of a graphite pencil on top of the sensing material leaving a 1 mm gap between the electrodes. A stainless steel mask was used as a stencil to guide the deposition of graphite-based electrodes and to protect 1 mm of the CNT-based sensing material from contamination by graphite.

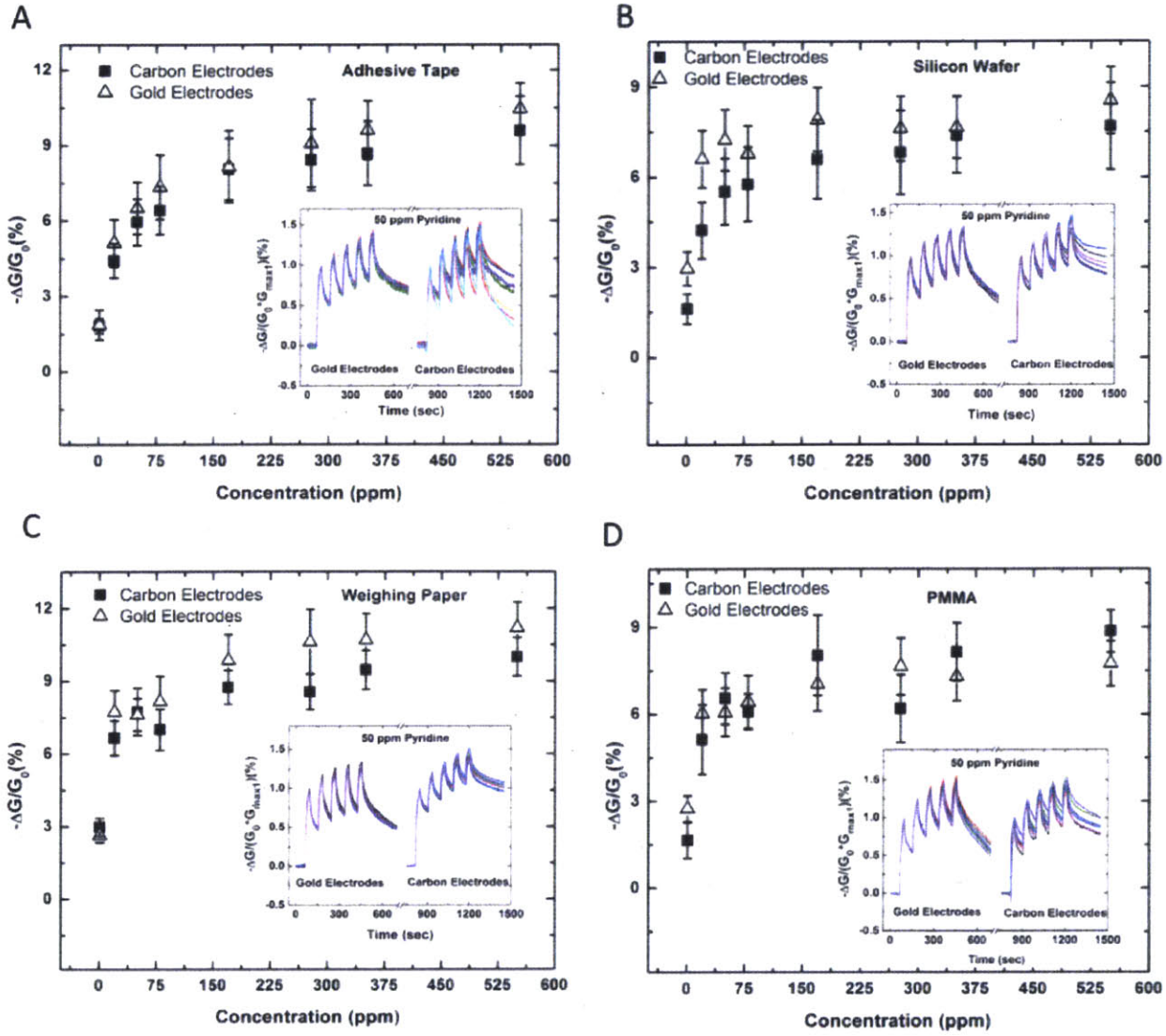

Figure 3.3. Comparison of device performance between fully-drawn sensors (SWCNT: TEC (1 : 2 wt. ratio) deposited by DRAFT and carbon-based electrodes deposited by mechanical abrasion) verses partially-drawn sensors (SWCNT : TEC (1 : 2 wt. ratio) deposited by DRAFT and gold electrodes deposited by thermal evaporation). A–D) Average normalized conductive response (first exposure exempt) of at least four fully-drawn sensors (black squares) and partially drawn sensors (white triangles) simultaneously exposed to various concentrations of pyridine for 30 s with 60 s recovery time. Inset: normalized conductance over time of seven fully-drawn and seven partially-drawn devices.

This two-step fabrication method is however limited to surfaces that facilitate efficient abrasion of graphite pencils to generate conductive electrodes (conductive line of 2.2 cm must have a resistance values < 9 kΩ). Graphite does not abrade efficiently on smooth surfaces (*e.g.*, weighing paper and PMMA) and yields electrodes with unacceptably high sheet resistance (Figure A3.13). This limitation can be overcome by introducing an additional step into the fabrication procedure by increasing surface roughness of the substrate through chemical or laser etching. This additional step has an added advantage of localizing the abrasion of graphite into pre-defined regions on the chip. Using this strategy, we demonstrate the ability to precisely fabricate fully-drawn working devices on laser-etched surfaces of weighing paper and PMMA (Figure 3.3C–D). We believe that this method is transferable to many substrates.

3.2.4 Comparing performance of fully-drawn and partially-drawn sensors

Figure 3.3 successfully demonstrates that the average normalized conductive response of the resulting chemiresistors with carbon-based electrodes is comparable to the standard gold electrode upon exposures to several concentrations of pyridine on various substrates. The plot (Figure 3.3) displays the average normalized conductive responses (first exposure exempt) of at least four devices with either gold electrodes or carbon-based electrodes simultaneously exposed five consecutive times to various concentrations of pyridine for 30 s with 60 s recovery times. The inset displays the normalized conductance trace (additionally normalized to the first exposure) over time of seven devices with either gold electrodes or carbon-based electrodes simultaneously exposed five consecutive times to 50 ppm pyridine for 30 s with 60 s recovery time. Device-to-device variation was investigated between fully-drawn and partially-drawn sensors on 4 substrates (weighing paper, PMMA, silicon, and adhesive tape) using SWCNT:TEC

as sensing material and graphite or gold as electrodes. At least 7 devices were exposed 5 consecutive times to 50 ppm pyridine 30 s with 60 s recovery times. The fully-drawn sensors yields slightly higher (1–5%) coefficient-of-variance in response to pyridine compared to the

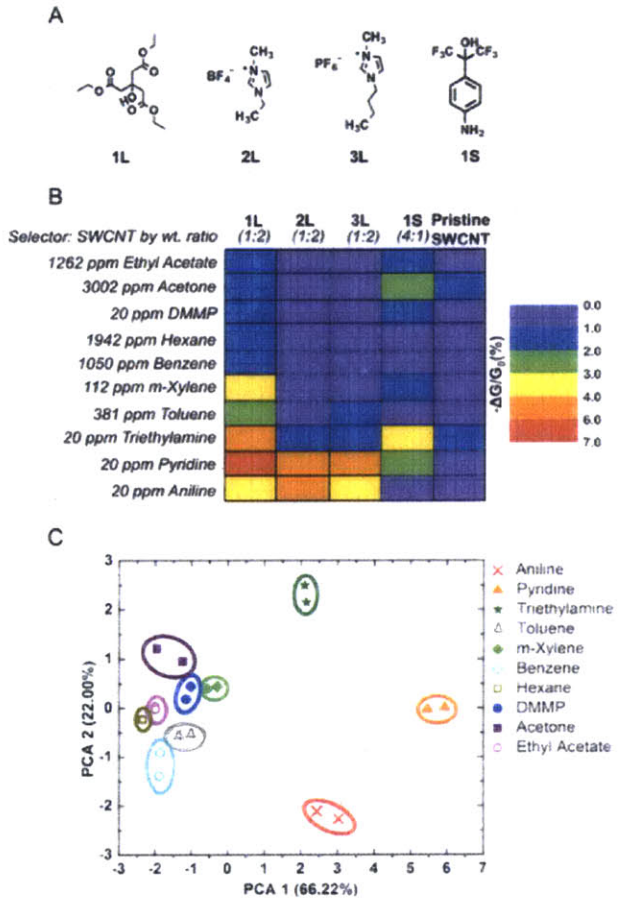

Figure 3.4. Fully-drawn sensor array. A) Schematic diagram of the selector's chemical structure used in the sensor array. L represents selectors that are liquids (Bp > 200 °C) and S represents selectors that are solids at room temperature prior to mixing with SWCNTs. The selectors were mixed with pristine SWCNTs mechanically and compressed into a pellet to make PENCILs. B) Average normalized conductive response (first exposure exempt) to simultaneous exposure to various gas analytes at ppm concentrations 5 consecutive times for 30 s with a 60 s recovery time. The PENCILs were deposited by DRAFT on weighing paper and the carbon-based electrodes (with 1 mm gap size) were deposited by abrasion using graphite pencil on the etched surface of weighing paper. C) Principal Component Analysis (PCA) plot discriminates between various gas analytes from the average conductive responses (first exposure exempt) of the sensor array.

partially drawn sensors (weighing paper: fully-drawn sensor [12%] and partially-drawn sensor [9%]) excluding the first exposure to pyridine (Tables A3.1 & A3.4).

3.2.5 Fully-drawn sensing arrays

The fabrication of fully-drawn chemical sensors is a general concept that can be extended to chemical sensing arrays. To illustrate this concept, we generated different sensing materials by mechanical mixing of SWCNTs with a solid selector, two different ionic liquids, or a plasticizer to draw a SWCNT-based chemiresistive array (Figure 3.4). The chemical structures of the selectors used are shown in Figure 3.4A. Selector **1L** was discussed earlier for pyridine sensing. Selector **2L** and **3L** are ionic liquids that have been previously used in conjunction with graphene and a quartz crystal microbalance to detect benzene.[46] Selector **1S** is a solid selector with a functional group handle (hexafluoroisopropanol) that has been previously used to detect Dimethyl methylphosphonate (DMMP) vapor *via* hydrogen-bond acids.[47-50] These selector:SWCNT composites were abrasion deposited over an etched pattern on the weighing paper. Graphite was then abraded on top of the etched pattern on the weighing paper leaving gap size of 1 mm between the electrodes. The chemiresistive array was then exposed to a variety of gas analytes that can be classified as biomarkers,[12, 51] nerve agents,[23, 50] industrial hazards,[9] quality of food markers,[9, 51, 52] and gasoline.[13] To investigate the selectivity of the devices that were fully-drawn and placed into array, we exposed the devices five consecutive times to various analytes for 30 s with a 60 s recovery time. The color scale mapping of the average normalized change of conductance (first exposure exempt) of fully-drawn devices is presented in Figure 3.4B. Each selector had enhancements in sensitivity and selectivity towards certain analytes compared to pristine SWCNTs. As predicted, selector **1S** caused the SWCNTs to

be more sensitive towards DMMP, however the enhancement was modest (1.3 times higher sensitivity). We speculate that in this formulation the hexafluoroisopropanol group is engaged in intermolecular hydrogen bonding with the aniline moiety thereby reducing the binding of DMMP. The ionic liquid selectors **2L** and **3L** did not show enhancements towards benzene possibly due to the change in morphology from graphene (flat) to carbon nanotubes (cylindrical) or change in sensing method from monitoring mass change (quartz crystal microbalance) to current change (chemiresistor). However, **2L** and **3L** did provide high selectivity towards amines and low sensitivity towards other analytes. The lone pair of electrons from the amines can interact with the ionic liquid to possibly cause charge separation thus enhancing the SWCNTs sensitivity and selectivity. Selector **1L** displayed the highest sensitivity towards pyridine. The average normalized conductive response (first exposure exempted) of the fully-drawn CNT-based chemiresistive array towards various analytes was analyzed using Principle Component Analysis (PCA) (Figure 3.4C). The four-component array can successfully discriminate nitrogen-containing compounds from one another (pyridine, aniline, and triethylamine) and from other VOCs at low ppm concentration levels. Aniline and triethylamine are additional amines that are of interest since aniline has been reported as a possible biomarker for patients with lung cancer and triethylamine has been reported as a possible biomarker for patients with renal failure.[51] This array lays the groundwork for detecting and differentiating amines of interest in occupational safety.

3.3 Conclusion

Abrasion over pre-patterned substrates successfully expands the scope of DRAFT in throughput, precision, and surface compatibility. Etching substrates (*e.g.*, laser or chemical)

enhanced the ability to control the location and other structural aspects of conductive carbon structures deposited on a variety of surfaces using DRAFT. This general strategy enabled the fabrication of fully-drawn chemiresistors on weighing paper, PMMA, adhesive tape, and an undoped silicon wafer by mechanical abrasion. Fully-drawn arrays on weighing paper were capable of detecting and discriminating low ppm concentrations of N-containing vapors (pyridine, aniline, and triethylamine). This fabrication methodology does not require specialized facilities (*e.g.*, clean room, thermal evaporator) and can be performed entirely on a desktop (with appropriate ventilation and safety precautions for handling nanomaterials). The method lays the groundwork for expanding the capabilities of the fabrication of functional sensors, circuits, and tags by drawing on a variety of surfaces. This method can also be used towards a more efficient and rapid parallel fabrication of multiple devices by abrading surfaces of carbon materials against pre-pattered substrates. We believe this type of strategy can facilitate controlled deposition of sensing materials and electrodes onto pre-defined regions on various surfaces.

3.4 Experimental Section

3.4.1 Fabrication of PENCILs

Triethyl citrate (cat. no. 109290) and 1-ethyl-3-methylimidazolium tetrafluoroborate (cat. no. 39736) were purchased from Sigma Aldrich. 2-(4-Aminophenyl)-1,1,1,3,3,3-hexafluoro-2-propanol (cat. no. B24048) and 1-*n*-butyl-3-methylimidazolium hexafluorophosphate (cat. no. L19086) were purchased from Alfa Aesar. Purified SWCNTs (>95% SWCNTs) were provided by Nano-C, Inc (Westwood, MA). All chemicals and reagents were used without further purification, unless noted otherwise. SWCNTs, selector, and 7 mm diameter stainless steel

grinding ball were added into a 5 ml stainless steel ball milling vial. The vial was placed into a mixing mill (MM400, Retsch GmbH, Haan, Germany) where the carbon material was mechanically mixed at 30 Hz for 5 min under ambient conditions. The SWCNTs:selector mixture was then placed into a custom-made stainless steel pellet mold with 2 mm internal diameter where the SWCNT composites were compressed (Carver Press, model # 3912) for 1 min to make PENCILs.

3.4.2 Fabrication of partially-drawn sensors

Glass slides (cat. no. 16004-422, VWR International) were cleaned by ultra-sonication in acetone for 30 min and dried using a stream of nitrogen. The glass slides were then cleaned with an UV Ozone Cleaner (Model no. 2, Jelight Company, Irvine, CA, http://www.jelight.com) for 10 min. PMMA (cat. no. 8560K172, 1/16" thick, McMaster-Carr) substrates were cleaned by ultra-sonication in soapy water for 15 min followed by sonication in methanol for another 15 min and dried using a stream of nitrogen. Alumina (cat. no. 8462K21, 0.025" thick, McMaster-Carr) substrates were cleaned by ultra-sonication for 15 min in soapy water and another 15 min in acetone and dried using a stream of nitrogen. Silicon wafer (cat. no. SIUc50D05C1-HHR, MTI Corporation), weighing paper (cat. no. 12578-165, VWR International), and adhesive tape (item 487908, model 52380P12, Invisible tape, Staples) was used without any further modification.

Using a stainless steel mask (purchased from Stencils Unlimited, Lake Oswego, OR, http://www.stencilsunlimited.com), layers of chromium (10 nm) and gold (75 nm) were deposited onto the substrate using thermal evaporation (Angstrom Engineering, Kitchener, Ontario, Canada). There was a 1 mm gap between the metal electrodes. The PENCILs were

inserted into a holder (item no. DA, Alvin Tech DA) and deposited using DRAFT between and on top of the metal electrodes until 100–500 kΩ resistance range was achieved on each substrate (as measured across the electrode gap with a multimeter); except for unpolished side of the silicon wafer, where 6–8 kΩ resistance range was achieved.

3.4.3 Laser-etching procedure

A Universal Laser Systems model VLS4.60 equipped with a 60 Watt laser was used for all laser-etching operations. The power, speed, and pulses-per-inch settings were adjusted to provide suitable etching on each substrate type. A listing of exact parameters can be found in Table A3.2.

3.4.4 Fabrication of fully-drawn sensors

The substrates were cleaned as stated previously. PENCILs were inserted into a holder (Alvin Tech DA) and deposited by DRAFT onto a substrate to generate a conductive line approximately 3 mm in length until 400–600 kΩ resistance range was achieved. Carbon-based electrodes with 1 mm gap size were deposited on top of the SWCNTs composites by abrasion using a graphite pencil (Faber-Castell PITT Graphite Pure Woodless 2900 9B) purchased from Artist and Craftsmen (Cambridge, MA). A stainless steel mask protected approximately 1 mm of the sensing material from contamination by graphite. The graphitic layers were deposited until a certain range of sheet resistance was obtained (Table A3.3).

3.4.5 Investigation of the sensory performance of devices

The sensor chip was placed in a 2 × 30 pin edge connector and enclosed in a home-made Teflon enclosure equipped with an inlet, an outlet, and an internal channel for gas flow.

Measurements of current were performed under a constant applied voltage of 50 mV using a PalmSense EmStat-MUX equipped with a 16-channel multiplexer (Palm Instruments BV, The Netherlands). The current through the sensor was monitored while exposing it to various analytes (delivered using Kin-Tech gas generator: precision gas standards generator model 491M-B, La Marque, TX) with dry nitrogen as the carrier gas five consecutive times for 30 s with a recovery time of 60 s.

3.5 *References*

(1) J. A. Griffith and T. S. Bayer, *Sens. Actuators, B*, 2014, **190**, 818–821.

(2) J. Zhou, K. Xu, P. Zhou, O. Zheng, Z. Lin, L. Guo, B. Qiu and G. Chen, *Biosens. Bioelectron.*, 2014, **51**, 386–390.

(3) J. Kong, N. R. Franklin, C. Zhou, M. G. Chapline, S. Peng, K. Cho and H. Dai, *Science*, 2000, **287**, 622–625.

(4) K. J. Albert, N. S. Lewis, C. L. Schauer, G. A. Sotzing, S. E. Stitzel, T. P. Vaid and D. R. Walt, *Chem. Rev.*, 2000, **100**, 2595–2626.

(5) Y. Liu, X. Dong and P. Chen, *Chem. Soc. Rev.*, 2012, **41**, 2283–2307.

(6) M.-I. Mohammed and M. P. Y. Desmulliez, *Lab Chip*, 2011, **11**, 569–595.

(7) C. Escobedo, *Lab Chip*, 2013, **13**, 2445–2463.

(8) J. W. Gardner, T. C. Pearce, S. Friel, P. N. Bartlett and N. Blair, *Sens. Actuators, B*, 1994, **18**, 240–243.

(9) C. Elosua, C. Bariain, I. R. Matias, A. Rodriguez, E. Colacio, A. Salinas-Castillo, A. Segura-Carretero and A. Fernandez-Gutiérrez, *Sensors*, 2008, **8**, 847–859.

(10) H. Wang, L. Nie, J. Li, Y. Wang, G. Wang, J. Wang and Z. Hao, *Chin. Sci. Bull.*, 2013, **58**, 724–730.

(11) J. S. Schreiber, S. House, E. Prohonic, G. Smead, C. Hudson, M. Styk and J. Lauber, *Risk Anal.*, 1993, **13**, 335–344.

(12) L. Dong, X. Shen and C. Deng, *Anal. Chim. Acta*, 2006, **569**, 91–96.

(13) L.-W. Jia, M.-Q. Shen, J. Wang and M.-Q. Lin, *J. Hazard. Mater.*, 2005, **123**, 29–34.

(14) J. Y. Kim, J. Lee, S. Hong and T. D. Chung, *Chem. Commun.*, 2011, **47**, 2892–2894.

(15) S. Daniel, T. P. Rao, K. S. Rao, S. U. Rani, G. R. K. Naidu, H.-Y. Lee and T. Kawai, *Sens. Actuators, B*, 2007, **122**, 672–682.

(16) J. M. Schnorr and T. M. Swager, *Chem. Mater.*, 2011, **23**, 646–657.

(17) K. Balasubramanian and M. Burghard, *Small*, 2005, **1**, 180–192.

(18) C. Dyke and J. Tour, in *Carbon Nanotubes*, CRC Press, 2006, pp. 275–294.

(19) K. M. Frazier and T. M. Swager, *Anal. Chem.*, 2013, **85**, 7154–7158.

(20) J. Kong, M. G. Chapline and H. Dai, *Adv. Mater.*, 2001, **13**, 1384–1386.

(21) R. J. Chen, Y. Zhang, D. Wang and H. Dai, *J. Am. Chem. Soc.*, 2001, **123**, 3838–3839.

(22) F. Wang and T. M. Swager, *J. Am. Chem. Soc.*, 2011, **133**, 11181–11193.

(23) F. Wang, H. Gu and T. M. Swager, *J. Am. Chem. Soc.*, 2008, **130**, 5392–5393.

(24) L. Hu, D. S. Hecht and G. Grüner, *Chem. Rev.*, 2010, **110**, 5790–5844.

(25) J. M. Lobez, S.-J. Han, A. Afzali and J. B. Hannon, *ACS Nano*, 2014.

(26) J. M. Schnorr, D. van der Zwaag, J. J. Walish, Y. Weizmann and T. M. Swager, *Adv. Funct. Mater.*, 2013, **23**, 5285–5291.

(27) J. Li, Y. Lu, Q. Ye, M. Cinke, J. Han and M. Meyyappan, *Nano Lett.*, 2003, **3**, 929–933.

(28) Q. Cao and J. A. Rogers, *Adv. Mater.*, 2009, **21**, 29–53.

(29) P. Qi, O. Vermesh, M. Grecu, A. Javey, Q. Wang, H. Dai, S. Peng and K. J. Cho, *Nano Lett.*, 2003, **3**, 347–351.

(30) D. R. Kauffman and A. Star, *Angew. Chem., Int. Ed.*, 2008, **47**, 6550–6570.

(31) K. G. Ong, K. Zeng and C. A. Grimes, *IEEE Sens. J.*, 2002, **2**, 82–88.

(32) P. Bondavalli, P. Legagneux and D. Pribat, *Sens. Actuators, B*, 2009, **140**, 304–318.

(33) N. Dossi, R. Toniolo, A. Pizzariello, F. Impellizzieri, E. Piccin and G. Bontempelli, *Electrophoresis*, 2013, **34**, 2085–2091.

(34) C.-W. Lin, Z. Zhao, J. Kim and J. Huang, *Sci. Rep.*, 2014, **4**, 1–6.

(35) K. ul Hasan, O. Nur and M. Willander, *Appl. Phys. Lett.*, 2012, **100**, 211104.

(36) E. W. Nery and L. T. Kubota, *Anal. Bioanal. Chem.*, 2013, **405**, 7573–7595.

(37) N. Kurra, D. Dutta and G. U. Kulkarni, *Phys. Chem. Chem. Phys.*, 2013, **15**, 8367–8372.

(38) N. Kurra and G. U. Kulkarni, *Lab Chip*, 2013, **13**, 2866–2873.

(39) A. J. Gimenez, J. M. Yáñez-Limón and J. M. Seminario, *J. Phys. Chem. C*, 2011, **115**, 282–287.

(40) G. Aragay, H. Montón, J. Pons, M. Font-Bardía and A. Merkoçi, *J. Mater. Chem.*, 2012, **22**, 5978–5983.

(41) A. W. Martinez, S. T. Phillips, Z. Nie, C.-M. Cheng, E. Carrilho, B. J. Wiley and G. M. Whitesides, *Lab Chip*, 2010, **10**, 2499–2504.

(42) K. A. Mirica, J. G. Weis, J. M. Schnorr, B. Esser and T. M. Swager, *Angew. Chem., Int. Ed.*, 2012, **51**, 10740–10745.

(43) K. A. Mirica, J. M. Azzarelli, J. G. Weis, J. M. Schnorr and T. M. Swager, *Proc. Natl. Acad. Sci. U. S. A.*, 2013, E3265–E3270.

(44) B. Yao, L. Yuan, X. Xiao, J. Zhang, Y. Qi, J. Zhou, J. Zhou, B. Hu and W. Chen, *Nano Energy*, 2013, **2**, 1071–1078.

(45) H.-M. Park, M. Misra, L. T. Drzal and A. K. Mohanty, *Biomacromolecules*, 2004, **5**, 2281–2288.

(46) Q. Ji, I. Honma, S.-M. Paek, M. Akada, J. P. Hill, A. Vinu and K. Ariga, *Angew. Chem.*, 2010, **122**, 9931–9933.

(47) L. S. Fifield and J. W. Grate, *Carbon*, 2010, **48**, 2085–2088.

(48) P. Xu, X. Li, H. Yu, M. Liu and J. Li, *J. Micromech. Microeng.*, 2010, **20**, 115003.

(49) Y. Yang, Y. Chen, P. Xu and X. Li, *Microelectron. Eng.*, 2010, **87**, 2317–2322.

(50) H. Li, Q. Zheng, J. Luo, Z. Cheng and J. Xu, *Sens. Actuators, B*, 2013, **187**, 604–610.

(51) B.-P. Jiang, D.-S. Guo and Y. Liu, *J. Org. Chem.*, 2011, **76**, 6101–6107.

(52) N. Funazaki, A. Hemmi, S. Ito, Y. Asano, Y. Yano, N. Miura and N. Yamazoe, *Sens. Actuators, B*, 1995, **25**, 797–800.

Chapter 3 Appendix

Additional Figures

Adapted from: Frazier, K.M.; Mirica, K.A.; Walish, J.J.; Swager, T.M. "Fully-drawn carbon-based chemical sensors on organic and inorganic surfaces," *Lab Chip*, **2014**, 14, 4059-4066.

Dr. Katherine Mirica fabricated devices as User-1 in Figure A3.14 and provided thoughtful discussions and feedback for the development of this chapter. Dr. Joseph Walish is responsible for laser-etching the substrates and the data in Table A3.2.

Sensing data acquisition was done using PSTrace software provided by Palm Instruments. Matlab (R2012a, Mathworks) and Microsoft Excel (2010) were used to calculate normalized sensing responses and principal component analysis.

Chemical-Etching Procedure:

A thick layer of etching cream (Cat. No. 15-0200, Armour Products) was applied to cover the desired surface of the glass and allowed to remain for 5 min. All traces of the Armour Etch Cream were washed with tap water and dried using a stream of nitrogen.

Profilometry:

Surface roughness of weighing paper, glass, PMMA, alumina, adhesive tape, and silicon wafer was measured using a Dektak 6M Stylus Profiler (Veeco Inc.) with a stylus radius of 2.5 μm over a distance of 1400 μm with duration of scan of 30 s and applied force corresponding to a mass of 1 mg. The average measurement of surface roughness and the standard deviation were calculated from four scans over different regions between four gold electrode gaps of the same substrate.

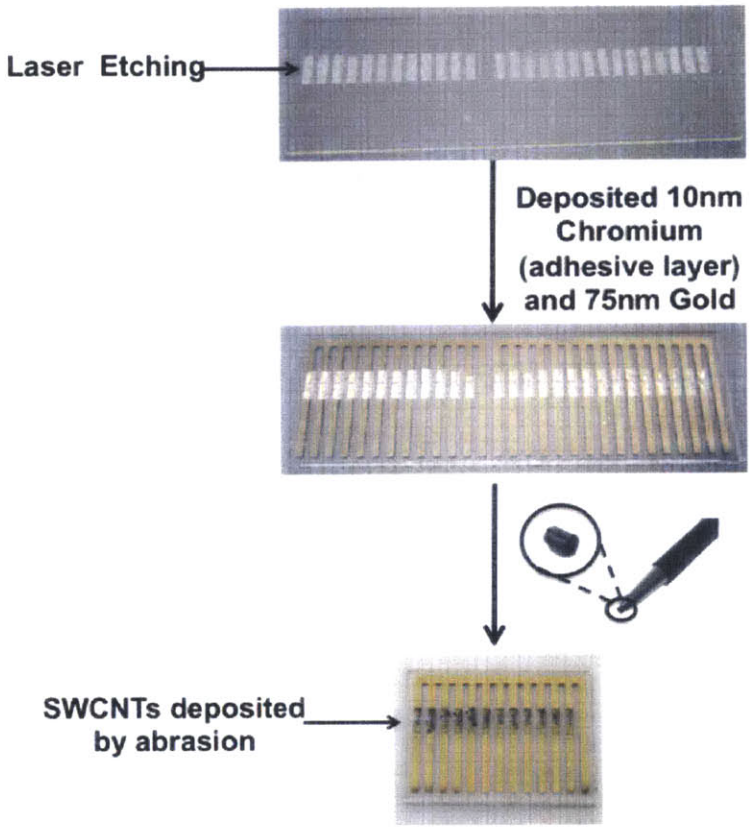

Figure A3.1. A stepwise procedure for the fabrication of partially-drawn SWCNT-based chemiresistive sensors on laser-etched glass. Step 1 involves laser etching of glass to define regions onto which the sensing material will be deposited. Step 2 involves deposition of gold electrodes on the surface of glass by thermal evaporation. Step 3 involves bridging the gap between the gold electrodes by depositing a film of SWCNTs by mechanical abrasion into etched regions of glass.

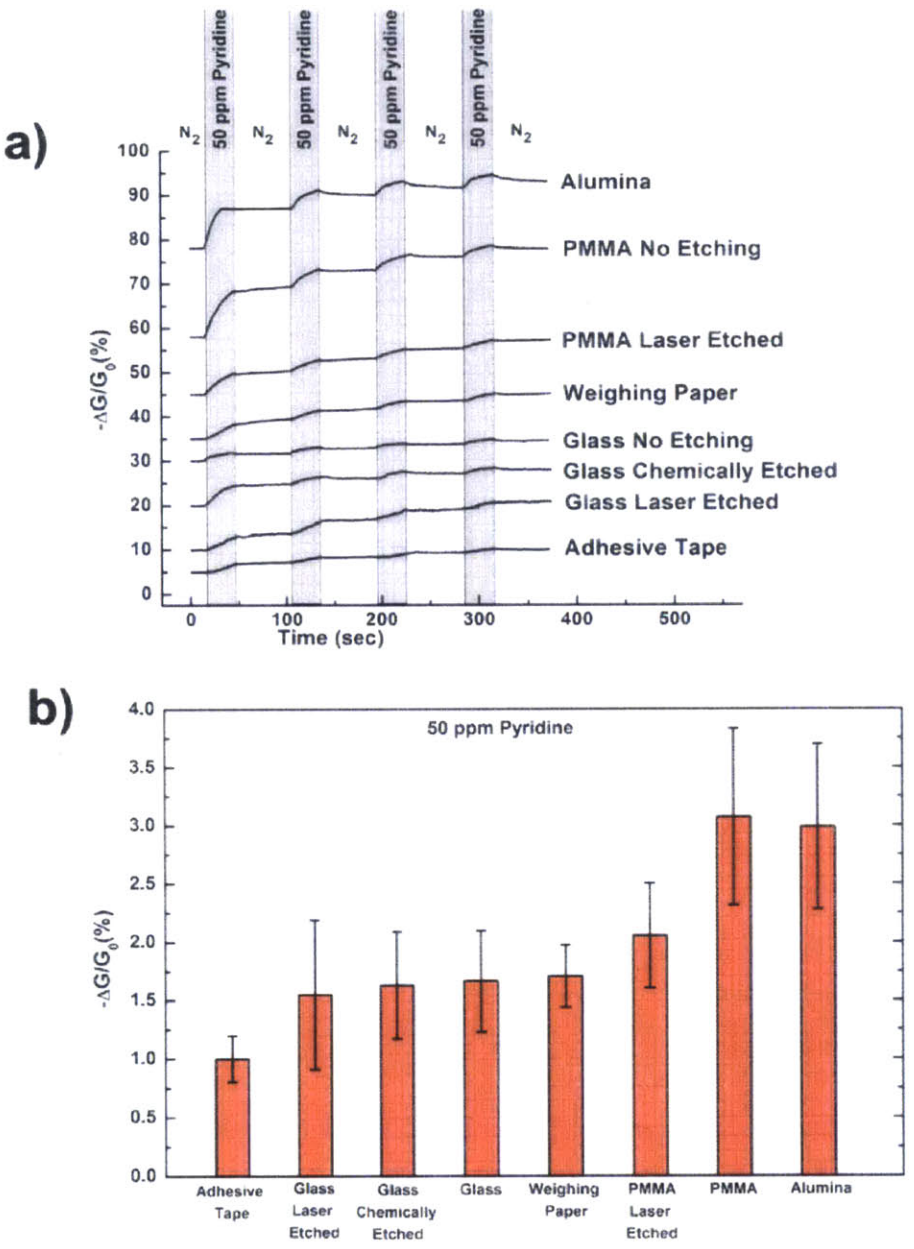

Figure A3.2. Sensing response of Pristine SWCNTs devices deposited by abrasion onto various substrates using gold electrodes (0.3 mm gap size). a) Normalized change of conductance over time from devices simultaneously exposed four consecutive times to 50 ppm pyridine for 30 s with recovery time of 60 s. b) Normalized average conductive responses (first exposure exempt) of at least three sensors simultaneously exposed four consecutive times to 50 ppm pyridine for 30 s with recovery time of 60 s.

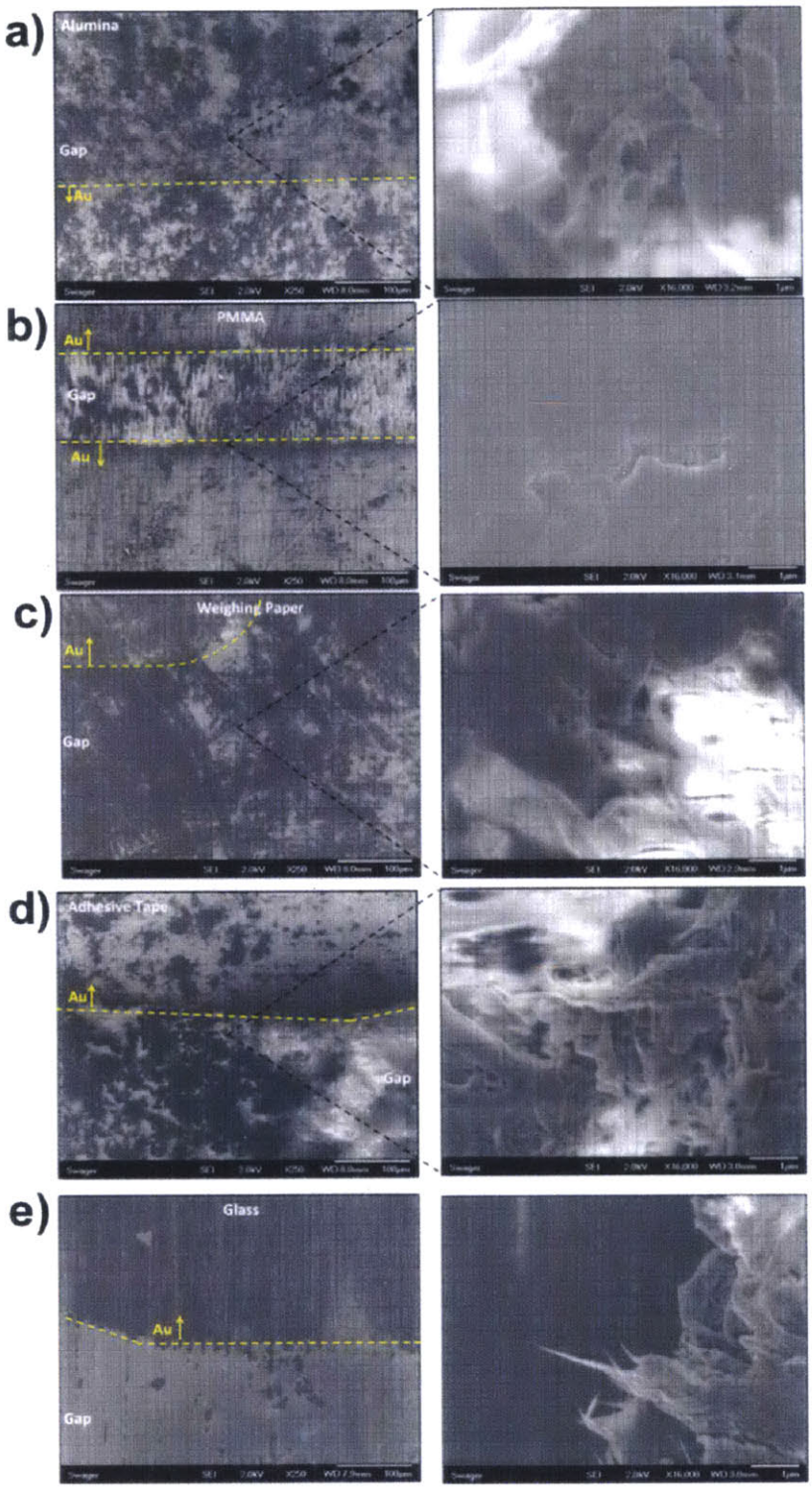

Figure A3.3. Characterization of abraded films of sensing materials using high resolution Scanning Electron Microscopy (SEM). a-e) Images of compressed pristine SWCNTs deposited by abrasion between and on top of gold electrodes onto alumina, PMMA, weighing paper, adhesive tape, and glass, respectively.

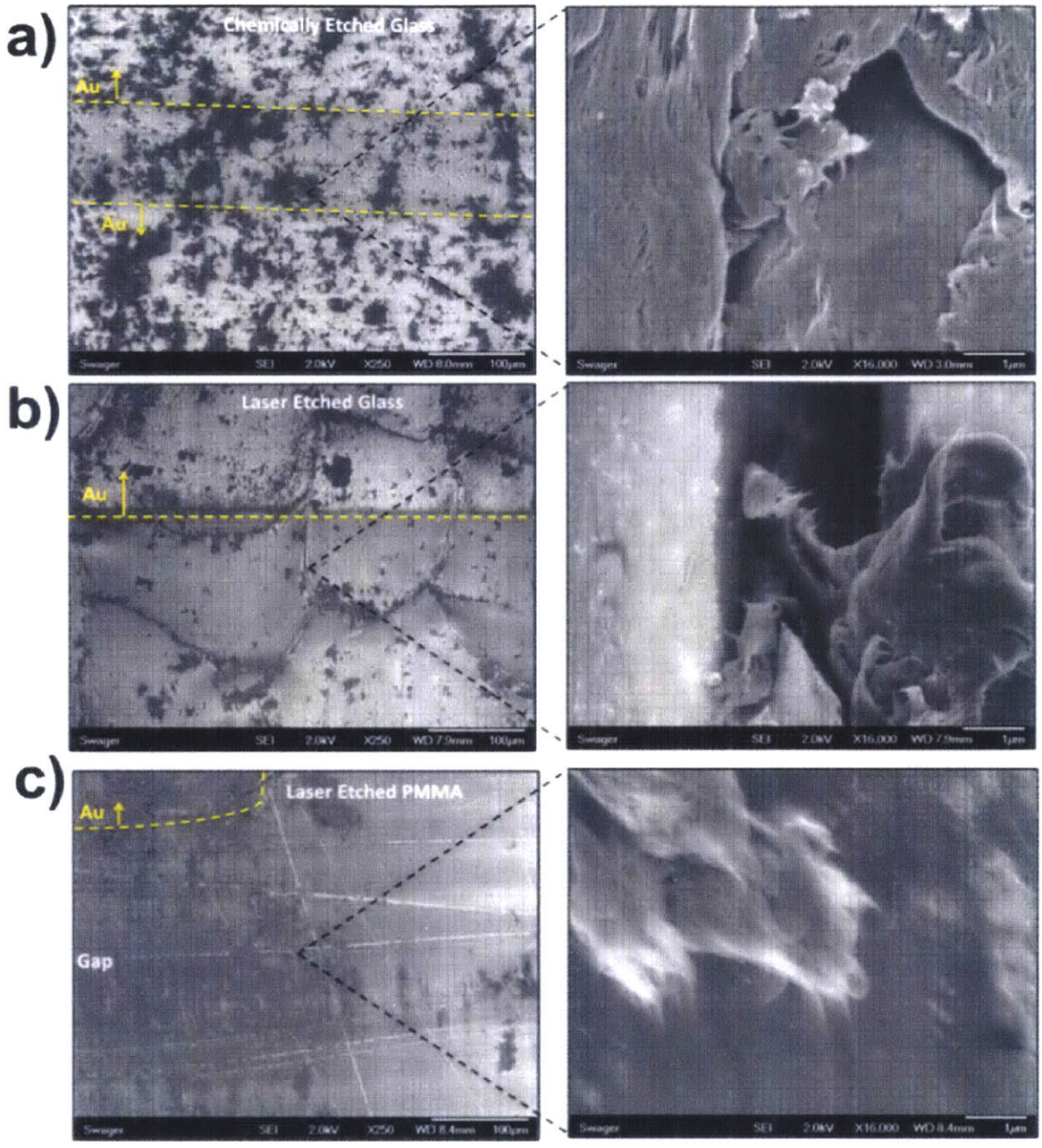

Figure A3.4. Characterization of abraded films of sensing materials using high resolution Scanning Electron Microscopy (SEM). a-c) Images of compressed pristine SWCNTs deposited by abrasion between and on top of gold electrodes onto chemically etched glass, and laser etched glass/PMMA.

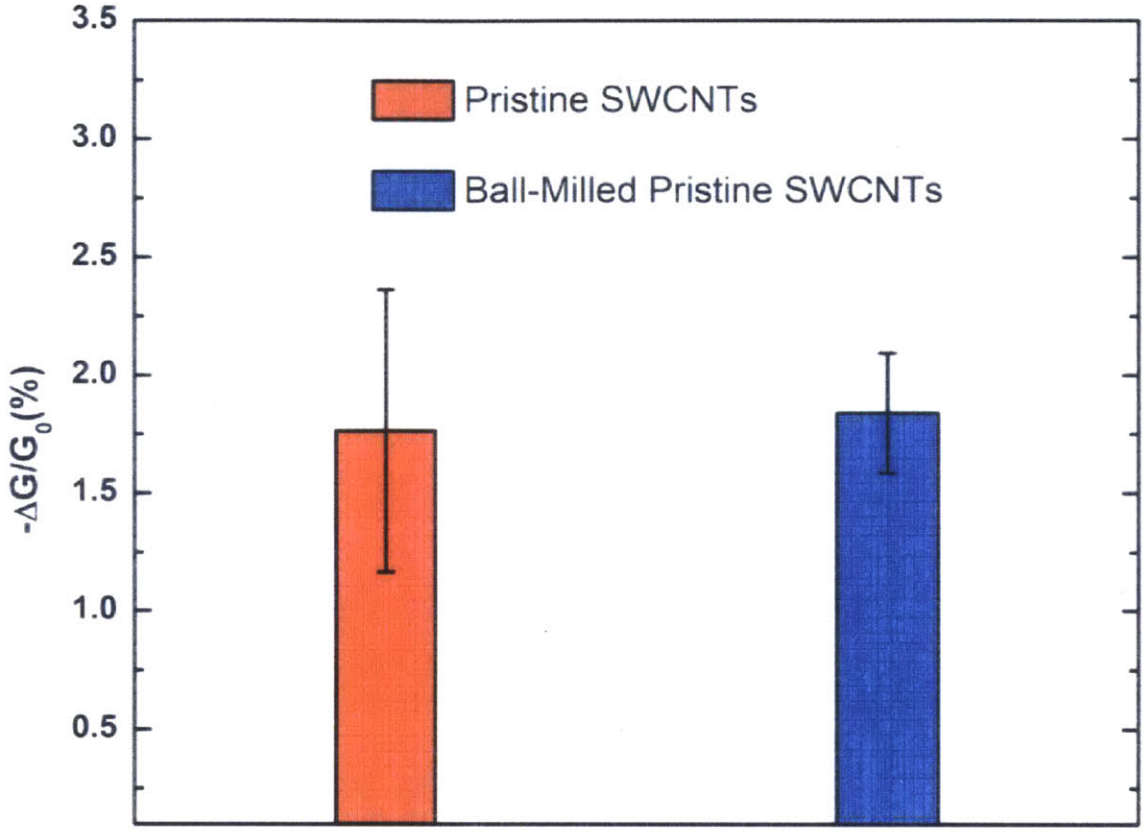

Figure A3.5. Investigation of the effect of ball milling on performance of SWCNTs as chemical sensing materials. Normalized average conductive responses of three pristine SWCNT-based sensors on weighing paper with gold electrodes simultaneously exposed four consecutive times to 50 ppm pyridine (first exposure exempt) for 30 s with recovery time of 60 s.

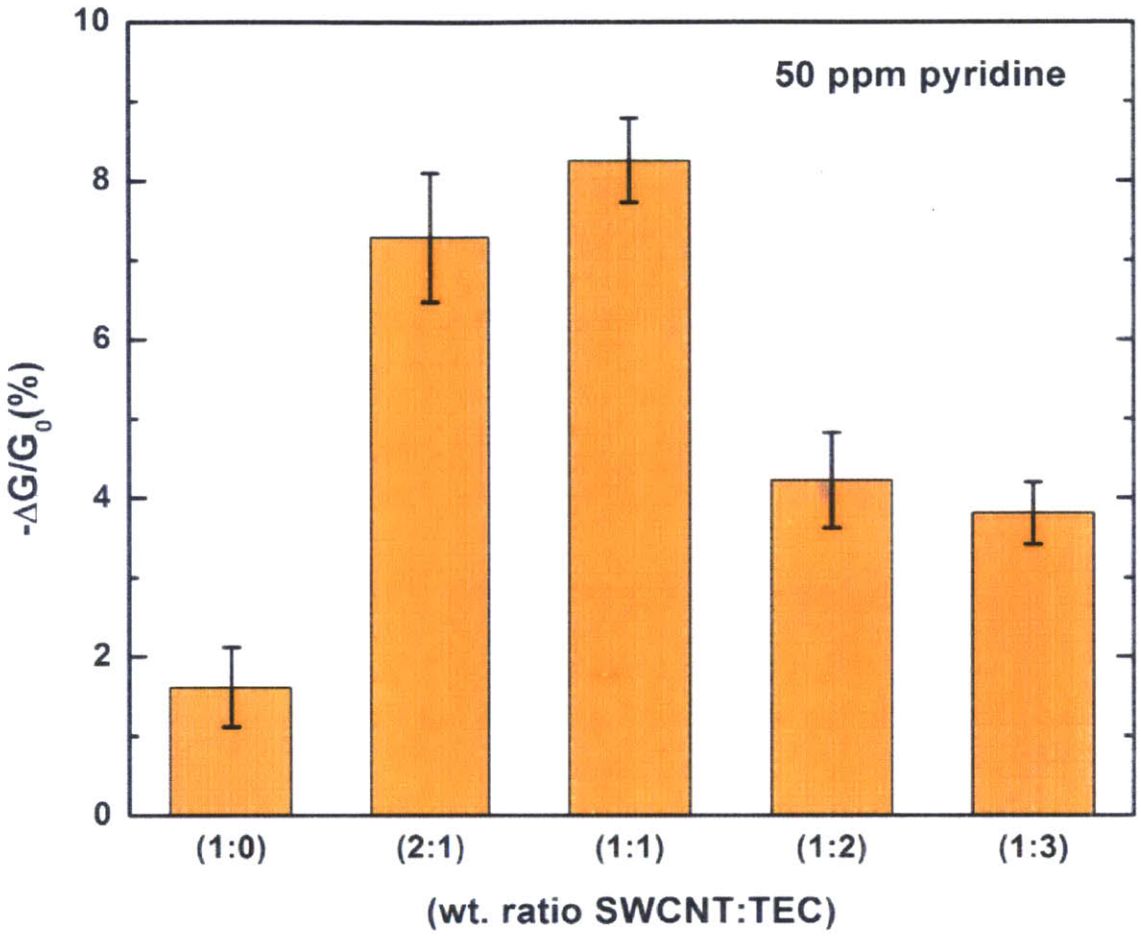

Figure A3.6. SWCNT and TEC was mechanically mixed at different mass ratios, compressed, and deposited between and on top of gold electrodes onto weighing paper (0.3 mm gap size). Normalized average conductive responses of two sensors simultaneously exposed four consecutive times to 50 ppm pyridine (first exposure exempt) for 30 s with a recovery time of 60 s.

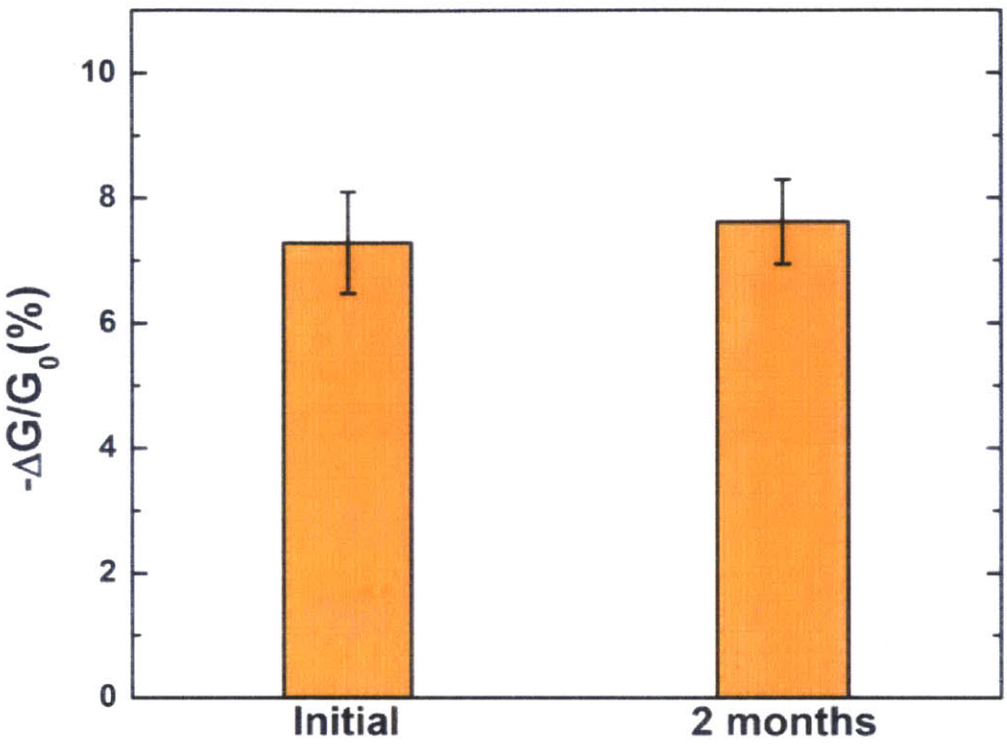

Figure A3.7. Stability of PENCILs. SWCNT and TEC (2:1 mass ratio) was mechanically mixed and deposited between and on top of gold electrodes onto weighing paper. Normalized average conductive responses of at least two sensors simultaneously exposed at least four consecutive times to 50 ppm pyridine (first exposure exempt) for 30 s with a recovery time of 60 s.

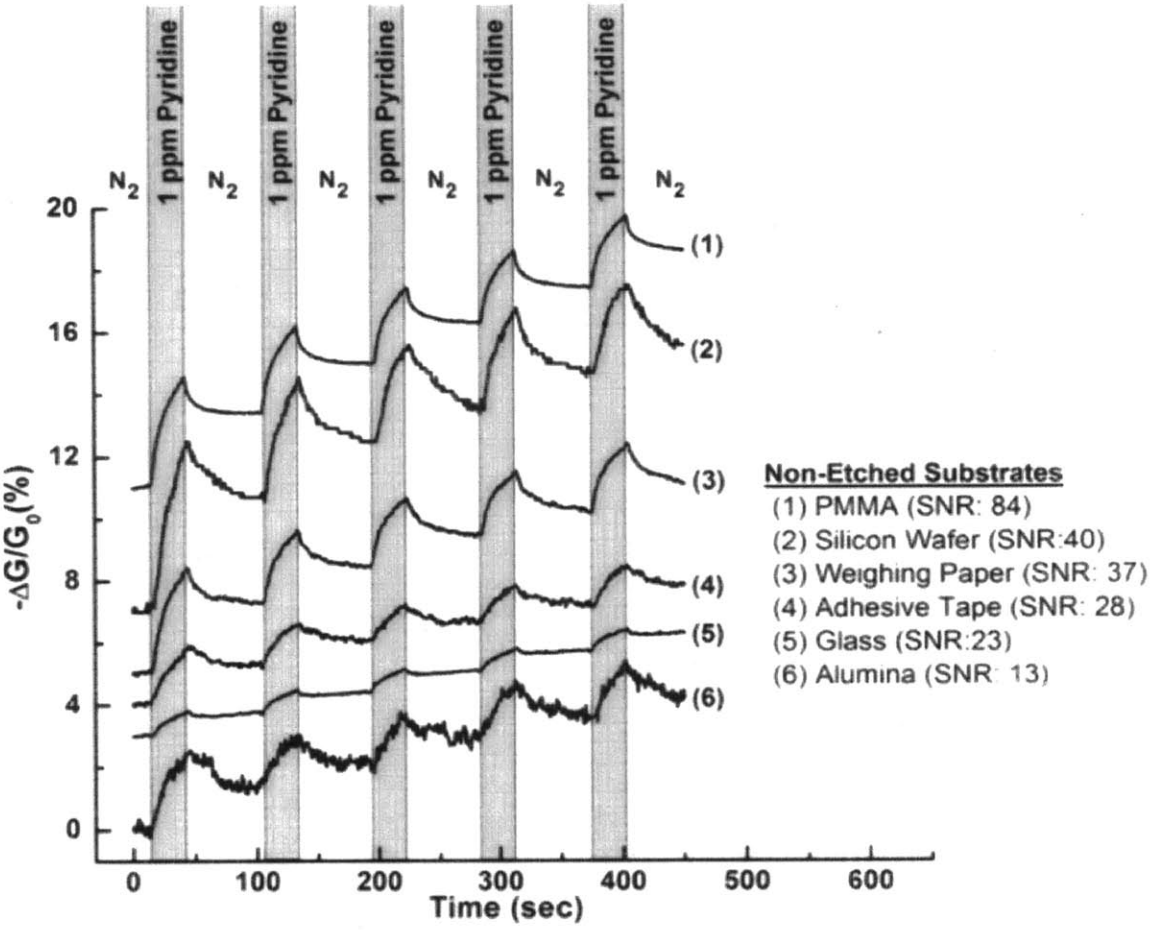

Figure A3.8. Investigation of the SWCNT-based chemiresistor's sensitivity on various unmodified substrates. Normalized change of conductance over time from devices simultaneously exposed five consecutive times to 1 ppm pyridine for 30 s with a recovery time of 60s. Devices were fabricated by depositing SWCNT:TEC (2:1 mass ratio) on top of and between gold electrodes by abrasion onto various substrates.

Glass					
Device -ΔG/G₀(%)	Exposure (50 ppm Pyridine)				
	1	2	3	4	5
1	2.681994599	2.50515168	2.328322819	2.32832282	2.21043457
2	2.48011096	2.33972627	2.10575922	2.05896804	2.01216571
3	2.809538145	2.61352241	2.482847844	2.41750667	2.31950659
4	3.206706066	2.86137555	2.713372552	2.68869558	2.59003476
5	2.845763745	2.5042702	2.333523421	2.30506789	2.27660557
6	3.264977026	2.96816327	2.806262521	2.80626252	2.64436177
7	2.883278345	2.66149024	2.578324665	2.49514587	2.35652996
8	4.64862109	3.91031237	3.718892961	3.69155012	3.52748007
Average Response	3.1	2.8	2.6	2.6	2.5
Standard Deviation	0.7	0.5	0.5	0.5	0.5
Overall Coefficient of Variance	20%		Overall Coefficient of Variance (first exposure exempt)		18%

Adhesive Tape					
Device -ΔG/G₀(%)	Exposure (50 ppm Pyridine)				
	1	2	3	4	5
1	6.74361725	5.83232526	4.52612896	4.31348595	3.9489706
2	9.30611923	6.24490259	5.67347652	5.55101695	5.46939022
3	10.4514714	6.68325454	6.54105944	6.25666076	5.9367239
4	13.2349655	7.81765585	7.13499436	6.78264838	6.91477353
5	14.4788349	8.57346731	8.00426524	7.57737641	7.61294836
6	11.8547745	7.4803203	6.95538746	6.7366598	6.60542007
7	11.6038209	7.4595963	6.96228659	6.46497688	6.54786512
8	10.9140538	7.0668499	6.35743594	6.27557999	6.05730177
Average Response	11	7.1	7	6	6
Standard Deviation	2	0.9	1	1	1
Overall Coefficient of Variance	31%		Overall Coefficient of Variance (first exposure exempt)		16%

Alumina					
Device -ΔG/G₀(%)	Exposure (50 ppm Pyridine)				
	1	2	3	4	5
1	13.59504074	8.01652891	7.314051248	7.1487592	6.81818003
2	13.5201551	8.16125839	7.325468881	7.22714174	6.63716716
3	12.66029908	7.33970092	6.766715727	6.54843101	6.19372403
4	15.05604576	7.39847665	6.9954485	6.93787697	6.79392756
5	12.07430556	9.08153325	7.80873729	7.49913761	6.15754719
6	14.15999413	8.87999535	8.559999466	7.92000771	8.07999611
7					
8					
Average Response	14	8.1	7.5	7.2	6.8
Standard Deviation	1	0.7	0.6	0.5	0.7
Overall Coefficient of Variance	30%		Overall Coefficient of Variance (first exposure exempt)		11%

Weighing Paper					
Device -ΔG/G₀(%)	Exposure (50 ppm Pyridine)				
	1	2	3	4	5
1	10.0404557	7.09820048	6.47297211	6.21551688	6.06840587
2	13.3563401	8.67422352	8.03351326	7.88565614	7.78708669
3	12.2302064	8.16758636	7.44816364	7.27888948	7.19424232
4	12.8393467	8.46375284	7.6333465	7.50559343	7.44171309
5	13.5167982	8.37717527	8.45810829	7.85107205	7.72967253
6	13.0000045	8.68421436	7.89473519	7.6842116	7.6842116
7	11.8730395	8.11128579	7.28839604	7.13165825	7.01410257
8					
Average Response	12	8.2	7.6	7.4	7.3
Standard Deviation	1	0.5	0.6	0.6	0.6
Overall Coefficient of Variance	24%		Overall Coefficient of Variance (first exposure exempt)		9%

PMMA					
Device -ΔG/G₀(%)	Exposure (50 ppm Pyridine)				
	1	2	3	4	5
1	10.13526496	7.12516798	6.267860386	5.8296862	5.31530346
2	8.942668887	6.38517343	5.698596694	5.21798643	4.80604531
3	9.858612413	6.78257557	5.961029086	5.50248558	4.98661959
4	9.498780337	6.60784213	5.838180253	5.38765105	4.82447837
5	10.34635383	7.10391051	6.190126105	5.7332339	5.20265508
6	10.5536855	7.28187882	6.375840295	5.87248911	5.35235263
7	12.19365222	8.28446966	7.262062327	6.735828	6.20959368
8	10.00481202	7.01782208	6.134574514	5.68492176	5.18708755
Average Response	10	7.1	6.2	5.7	5.2
Standard Deviation	1	0.6	0.5	0.5	0.4
Overall Coefficient of Variance	27%		Overall Coefficient of Variance (first exposure exempt)		14%

Silicon					
Device -ΔG/G₀(%)	Exposure (50 ppm Pyridine)				
	1	2	3	4	5
1	10.1851863	6.27572615	5.86420196	5.24691176	5.0411536
2	13.4642329	7.85414032	7.29312304	6.73212715	6.45161049
3	6.55737705	6.77595295	6.77595295	6.88524924	9.18032954
4	13.8345819	8.49623142	7.59398955	7.14286288	6.9924835
5	14.0449429	8.42696039	7.44381867	7.30336603	7.02247682
6	13.636359	8.55615142	7.62031646	7.08555509	7.21924288
7	11.2299481	7.21925308	6.68448151	6.41711612	6.14973543
8	14.8203609	9.43113044	8.38323087	8.23353256	7.78443763
Average Response	12	8	7.2	6.9	7
Standard Deviation	3	1	0.8	0.8	1
Overall Coefficient of Variance	30%		Overall Coefficient of Variance (first exposure exempt)		14%

Table A3.1. Device-to-device variance of chemiresistive material on 6 different substrates. Normalized average conductive response to 50 ppm pyridine 5 consecutive times for 30 s with recovery time of 60 s. Devices were fabricated by depositing SWCNT:TEC (2:1 mass ratio) on top on and between gold electrodes onto glass, adhesive tape, alumina, weighing paper, PMMA, or silicon.

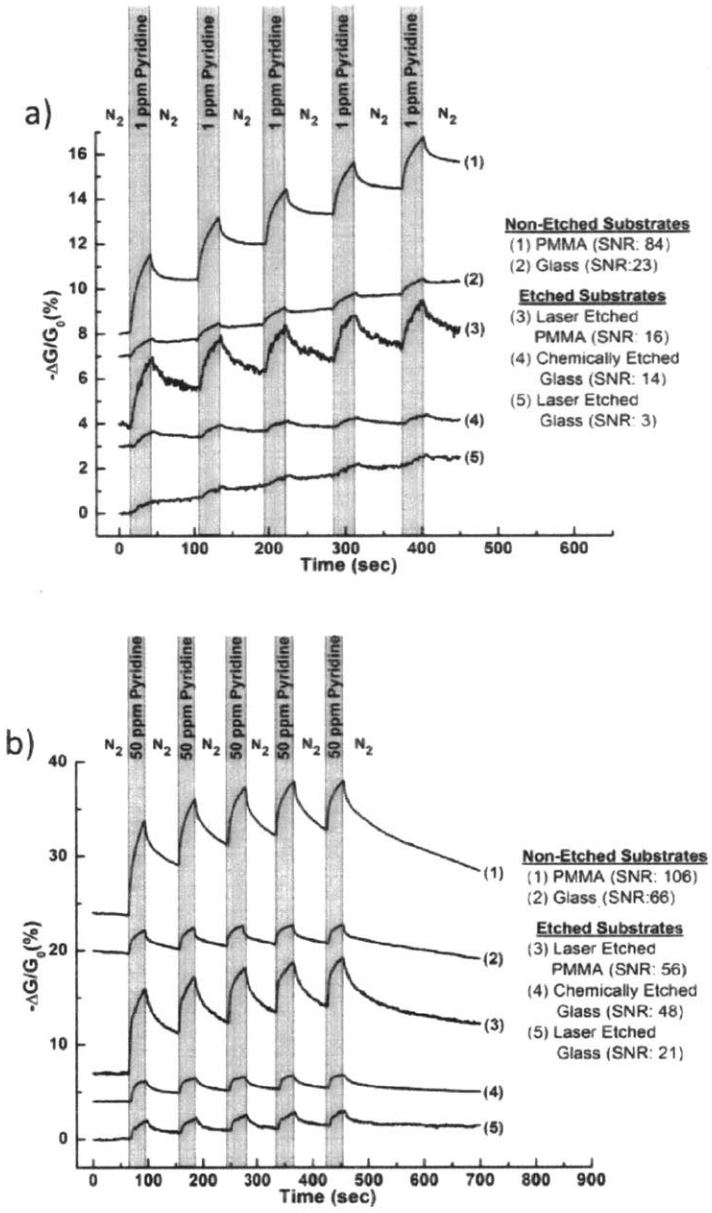

Figure A3.9. Comparison study of SWCNT-based chemiresistor's sensitivity on various modified or unmodified substrates. Normalized change of conductance over time of devices simultaneously exposed five consecutive times to 1 ppm (a) and 50 ppm (b) pyridine for 30 s with recovery time of 60s. The devices were fabricated by depositing SWCNT:TEC (2:1 mass ratio) on top of and between gold electrodes by abrasion onto various modified and unmodified substrates.

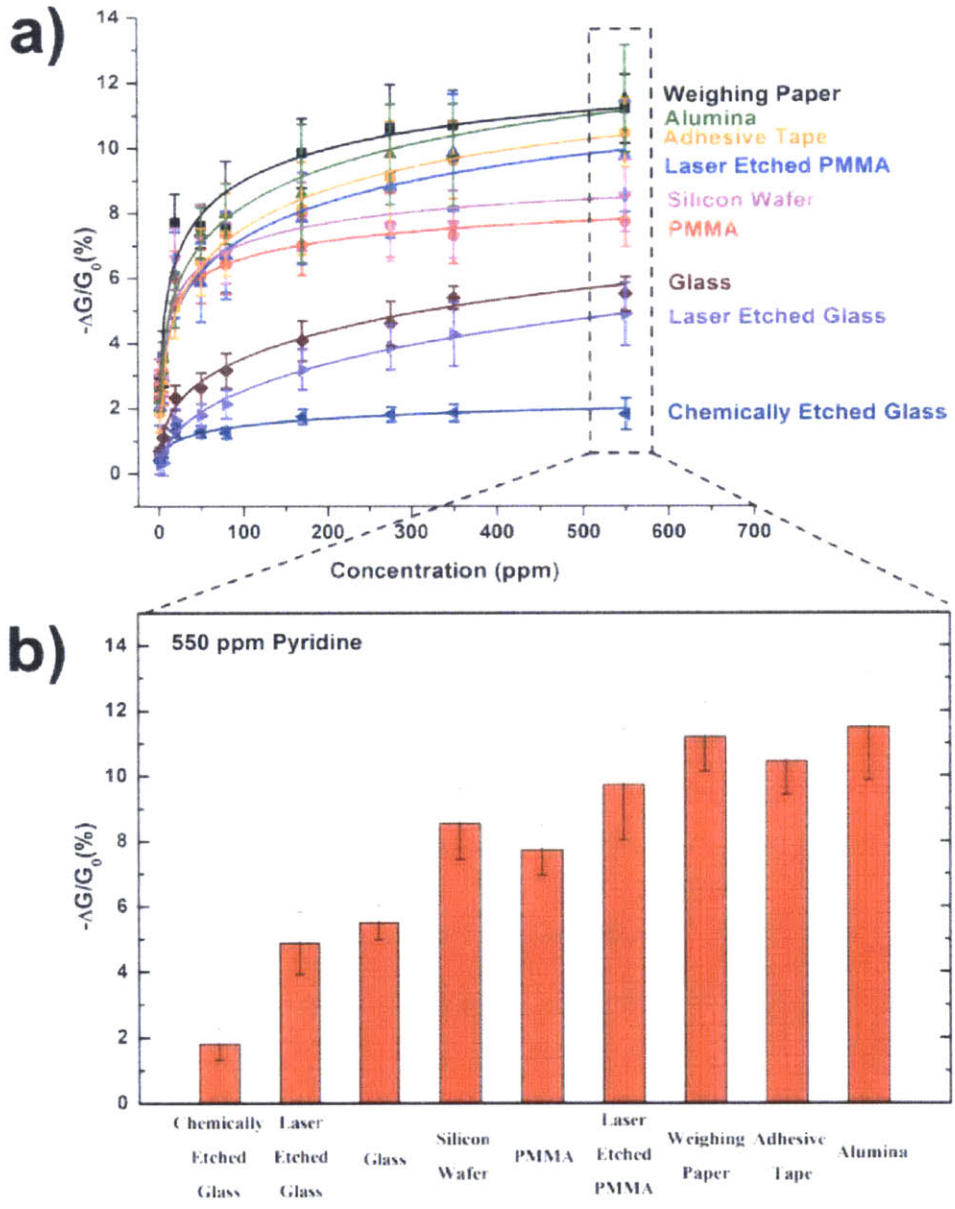

Figure A3.10. Sensing response of SWCNTs-TEC (2:1 wt. ratio) deposited by abrasion on various substrates between gold electrodes (1 mm gap size). a) Normalized average conductive responses (first exposure exempt) of at least six sensors simultaneously exposed five consecutive times to various concentrations of pyridine for 30 s with recovery time of 60 s. b) Substrate effects on the sensory performance was further investigated by analyzing the normalized average conductive responses (first exposure exempt) upon exposure to 550 ppm pyridine.

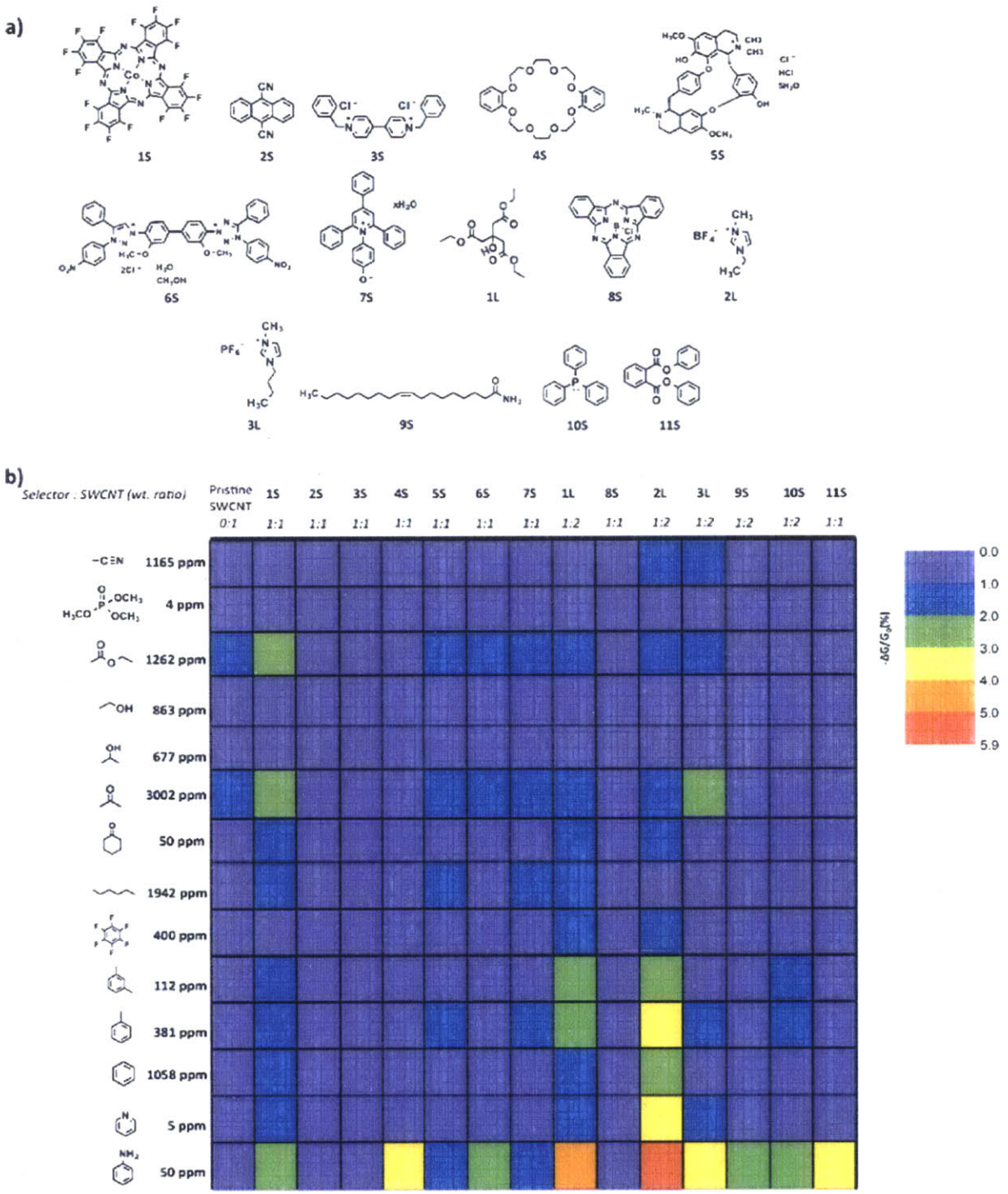

Figure A3.11. Sensing response of chemiresistor array fabricated on adhesive tape. The devices were fabricated by depositing SWCNT:Selector mixtures on top of and between gold electrodes by abrasion onto adhesive tape. a) Schematic diagram of the chemical structures of selectors used in the array. b) Normalized average conductive response (first exposure exempt) of three devices simultaneously exposed five consecutive times to various VOCs for 30 s with a recovery time of 60s.

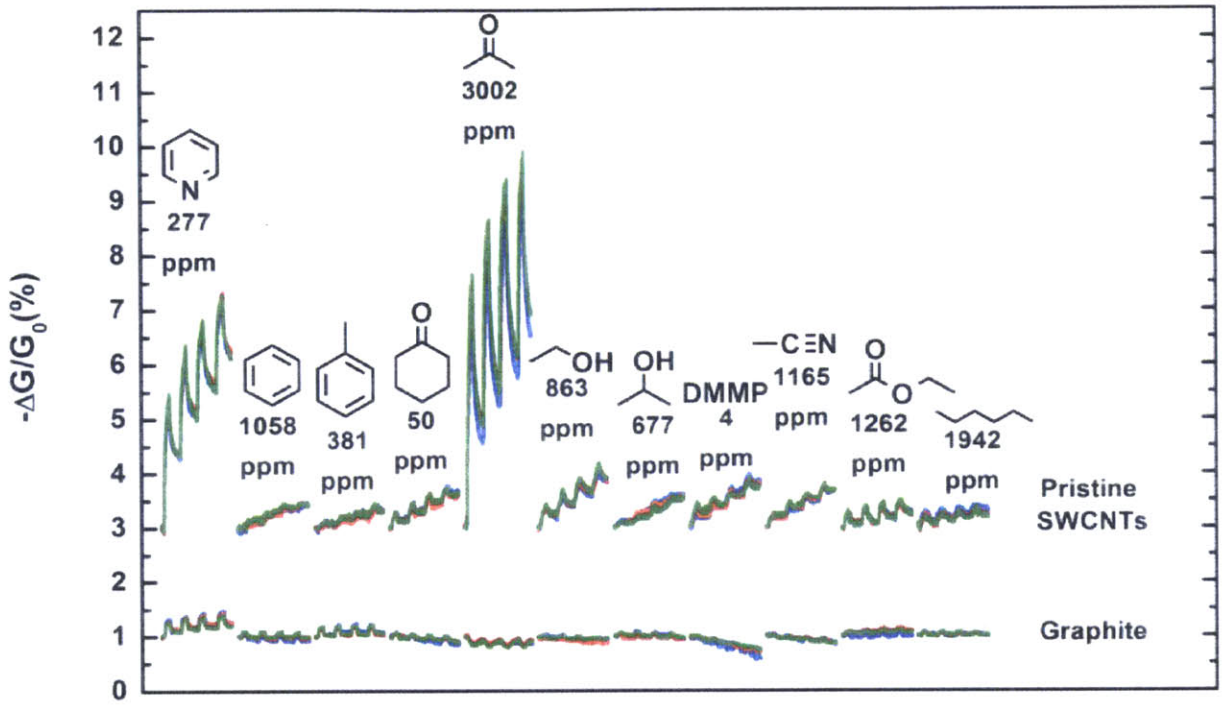

Figure A3.12. Comparison of sensing responses from graphite and pristine SWCNTs deposited on the surface of weighing paper between gold electrodes. Resistance range of the sensors was between 1-2 kΩ. Normalized change of conductance over time for three devices simultaneously exposed four consecutive times to various analytes for 30 s with a recovery time of 60 s.

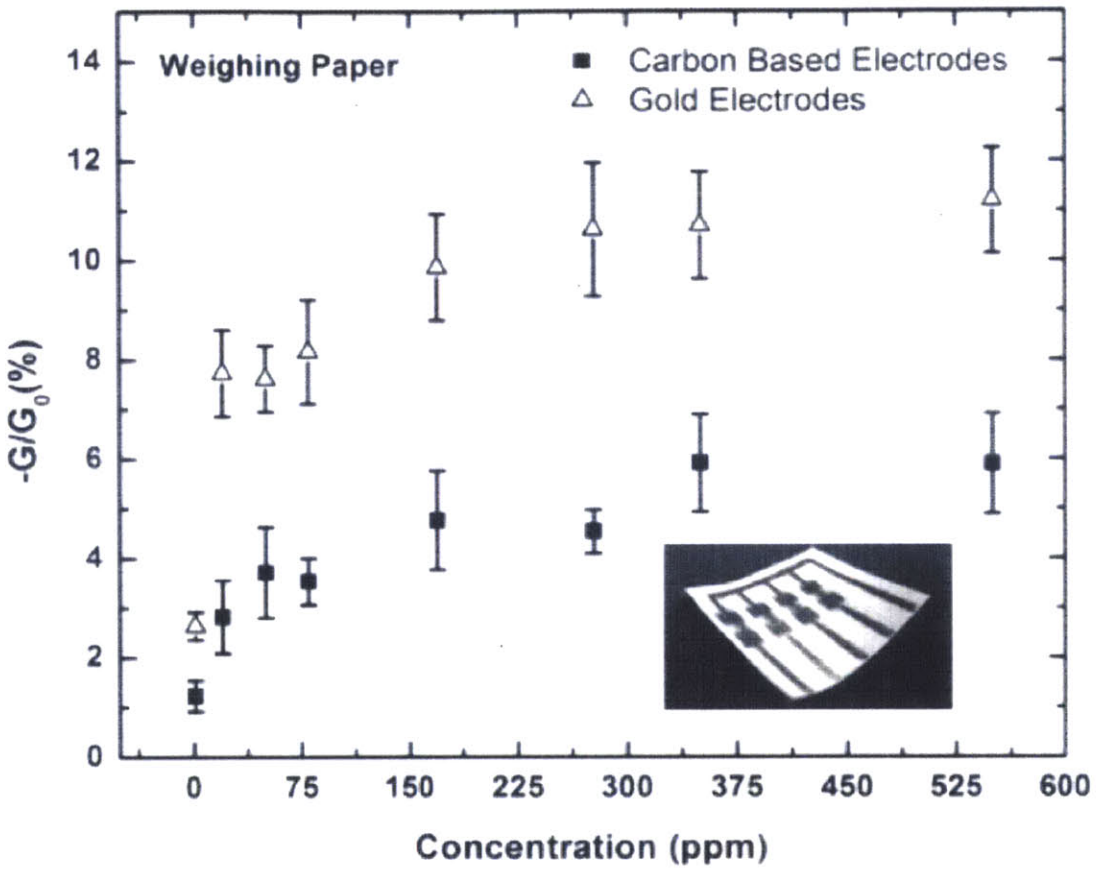

Figure A3.13. Normalized average conductive response (first exposure exempt) of at least four devices simultaneously exposed five consecutive times to various concentrations of pyridine for 30 s with recovery time of 60s. The devices were fabricated by depositing SWCNT:TEC (2:1 mass ratio) between carbon-based electrodes or gold electrodes by abrasion onto weighing paper. The carbon-based electrodes were fabricated by depositing graphite by abrasion on weighing paper.

Material	Power	Speed	Pulses-per-inch (PPI)
Weighing paper	15	100	1000
PMMA	20	50	500
Glass	10	10	1000

Table A3.2. Parameters used in laser-etching

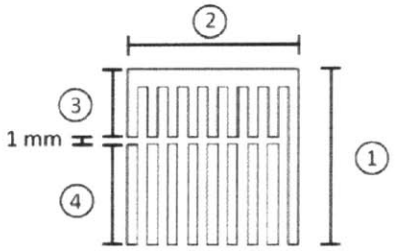

	Laser-Etched Weighing Paper		Laser-Etched PMMA		Adhesive Tape		Unpolished Silicon Wafer	
	Distance (cm)	*Resistance (kΩ)*	*Distance (cm)*	*Resistance (kΩ)*	*Distance (cm)*	*Resistance (kΩ)*	*Distance (cm)*	*Resistance (kΩ)*
1	2.2	7-8.4	2.2	2-2.6	1.7	8-9.9	2.2	4-4.8
2	2.2	5-6.5	2.2	2-2.5	2	8-9.7	2.2	3-3.7
3	0.8	2.8-5.5	0.8	0.8-1.2	0.7	2.6-3.2	0.8	2.1-2.4
4	1.3	4.2-6.5	1.3	1.6-2.3	0.9	2.7-3.2	1.3	2.7-3.8

Table A3.3. Resistive measurements of carbon-based electrodes used for chemiresitive sensors. Resistance ranges were derived from at least 2 drawn conductive lines. Functionalized SWCNTs with graphite electrodes (drawn within this range or below) had similar sensory performance as functionalized SWCNTs with gold electrodes.

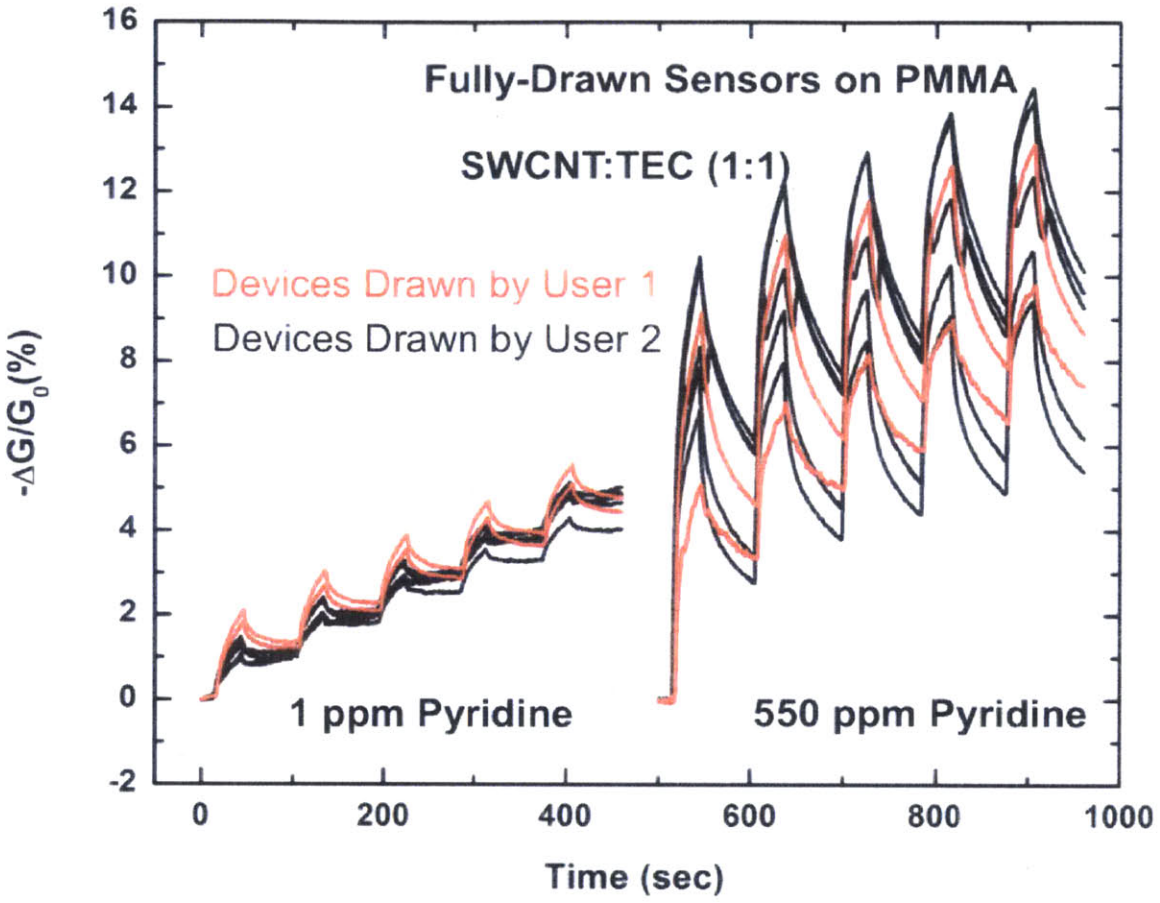

Figure A3.14. User-to-user reproducibility for fully-drawn carbon-based chemiresistors. Normalized change of conductance over time of 2 devices from user 1 and 5 devices from user 2 simultaneously exposed five consecutive times to 1 and 550 ppm pyridine for 30 s with a recovery time of 60s. The devices were fabricated by depositing SWCNT:TEC (1:1 mass ratio) between carbon-based electrodes. The carbon-based electrodes were fabricated by depositing graphite by abrasion onto laser-etched PMMA.

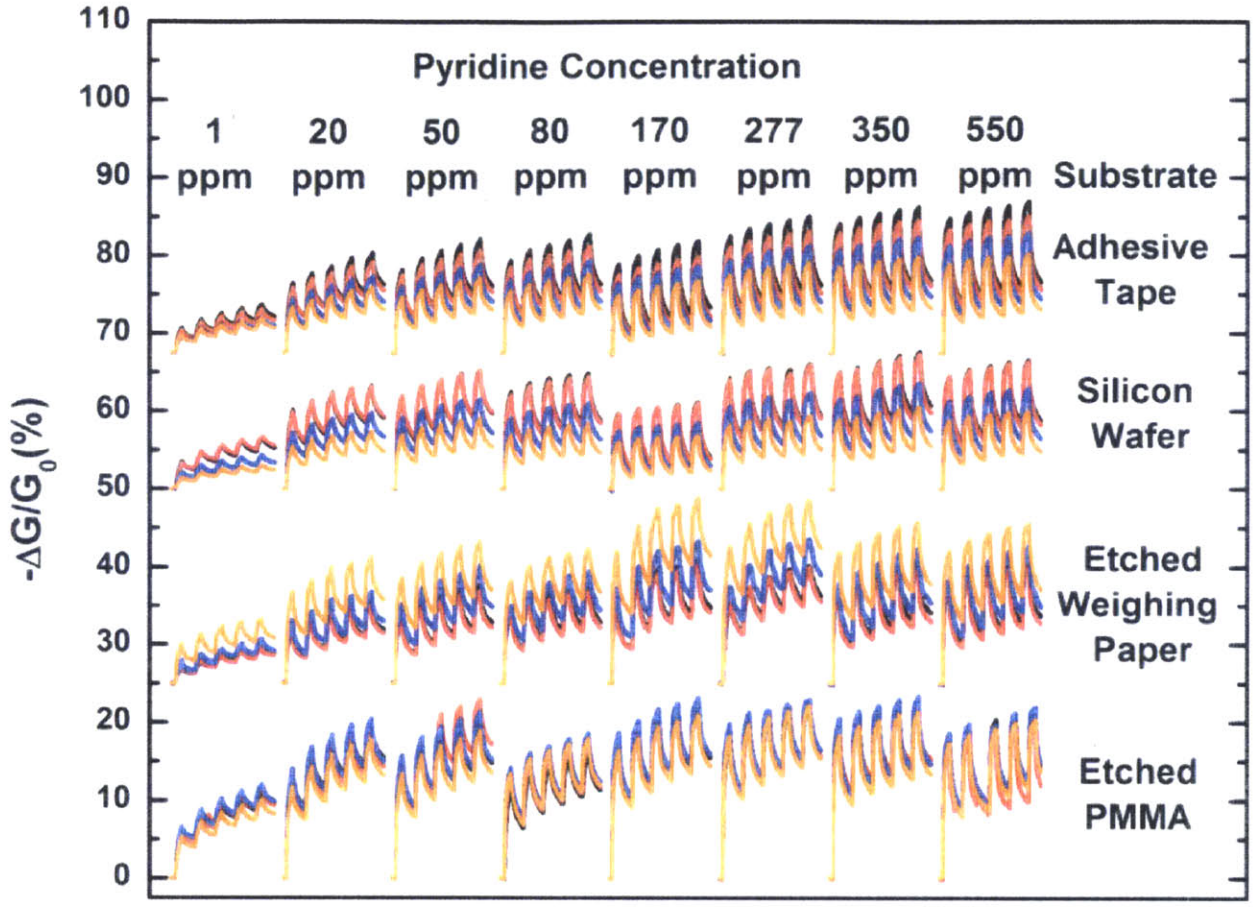

Figure A3.15. Sensing response traces of four fully drawn devices on various substrates. Normalized change of conductance over time for three devices simultaneously exposed five consecutive times to various concentrations of pyridine for 30 s with recovery time of 60s. The devices were fabricated by depositing SWCNTs-TEC (2:1 wt. ratio) as the sensing material and graphite as the electrode by abrasion on various modified (PMMA and weighing paper) and unmodified (adhesive tape and silicon wafer) substrates.

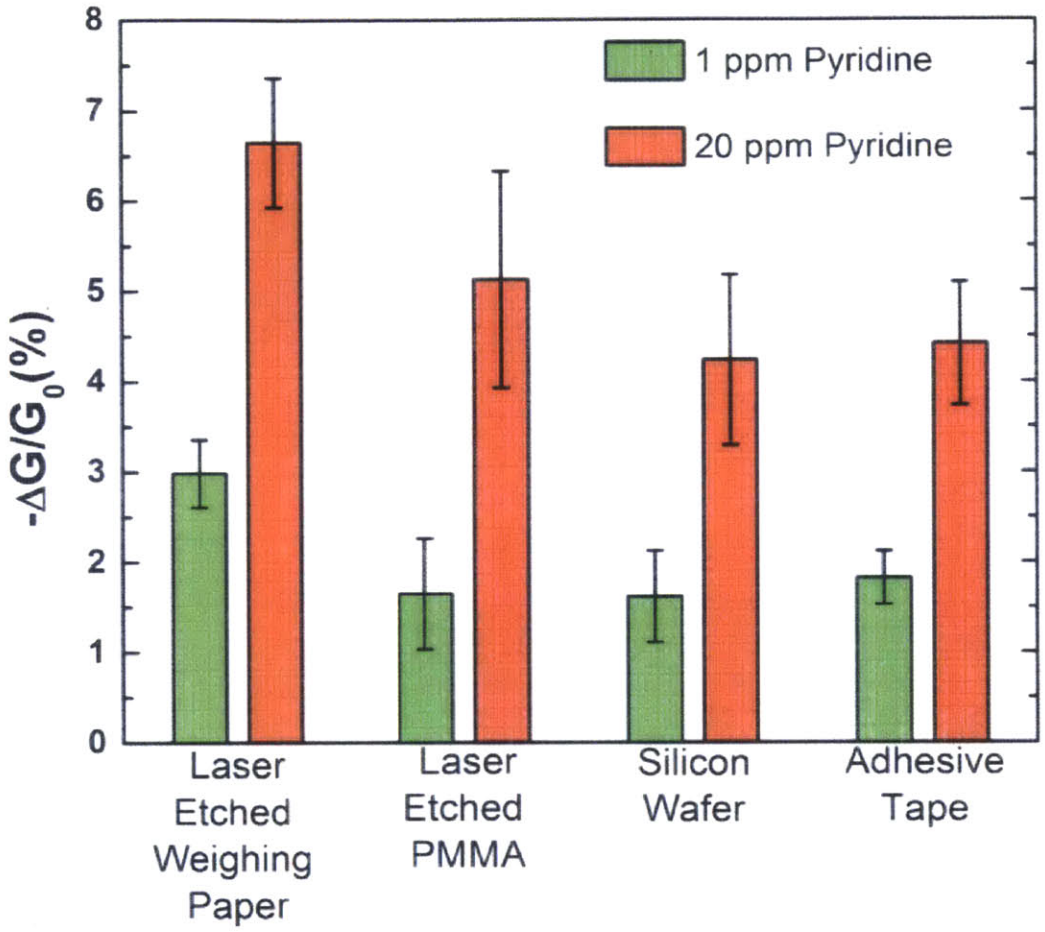

Figure A3.16. Discrimination of pyridine threshold value limit (1 ppm). Average normalized conductive response (first exposure exempt) of at least four sensors simultaneously exposed to 1 ppm and 20 ppm of pyridine for 30 s with 60 s recovery time. SWCT:TEC (1:2 wt. ratio) pellet was deposited by mechanical abrasion between carbon-based on non-etched substrates (adhesive tape and silicon wafer) and laser etched substrates (weighing paper and PMMA).

Silicon						Adhesive Tape					
Device -ΔG/G$_0$(%)	Exposure (50 ppm Pyridine)					Device -ΔG/G$_0$(%)	Exposure (50 ppm Pyridine)				
	1	2	3	4	5		1	2	3	4	5
1	12.0578244	7.13626659	6.53132438	6.60309686	6.03916469	1	10.7284573	7.55385452	7.19954479	7.00113972	7.00113296
2	12.0213998	6.90612895	6.34005908	6.42240133	5.92836744	2	10.0678072	6.61992556	6.24066438	6.11423486	6.06827194
3	9.06397735	5.40067357	4.95622924	5.05050492	4.68686923	3	8.47276308	5.80278056	5.53577552	5.4289752	5.44678233
4	6.93655398	4.42295678	4.03625483	4.07250598	3.84290386	4	7.22221857	5.02057513	4.79424428	4.69136127	4.73251055
5	11.576235	6.34017367	5.64247918	5.39863107	5.22928493	5	7.51670274	4.51002032	4.28730605	3.98107227	3.8697085
6	12.2462783	6.51781224	5.98782829	5.60442282	5.5705904	6	9.99798978	6.09503192	5.45345129	5.15938846	4.97226741
7	13.8777949	6.48214217	5.71084549	5.40452307	5.23494213	7	8.36486207	5.22502329	4.87883361	4.23476373	4.41188563
8	13.5554758	6.24504274	5.5423308	5.29865366	5.15697525	8	13.9947391	8.11433001	7.75295826	6.73456479	6.70170783
Average Response	11	6.2	5.6	5.5	5.2	Average Response	10	6	5.8	5	5
Standard Deviation	2	0.9	0.8	0.8	0.7	Standard Deviation	2	1	1	1	1
Overall Coefficient of Variance		39%	Overall Coefficient of Variance (first exposure exempt)		15%	Overall Coefficient of Variance		32%	Overall Coefficient of Variance (first exposure exempt)		20%

PMMA						Weighing Paper					
Device -ΔG/G$_0$(%)	Exposure (50 ppm Pyridine)					Device -ΔG/G$_0$(%)	Exposure (50 ppm Pyridine)				
	1	2	3	4	5		1	2	3	4	5
1	8.01757226	5.36252658	4.7921851	5.09374223	4.77251643	1	13.6962788	8.3094539	7.04871158	6.81948135	6.87679062
2	12.3745288	6.666992	5.99290704	5.73706107	5.67801247	2	16.3455903	9.74897433	8.58144012	8.17279515	8.05604242
3	12.0066484	6.44994052	5.7540495	5.45284176	5.38013746	3	16.8236341	9.50342395	8.34760936	7.91951741	7.79109697
4	8.45116782	4.77857169	4.35390648	4.12991831	4.11125337	4	15.4873855	8.51063428	7.47154933	7.22414731	7.02622805
5	8.81863876	6.48919016	6.07320727	5.9900107	5.82361755	5	15.1340237	8.82474102	10.1855653	7.25773135	7.09278503
6	8.41514523	6.10098046	5.82048253	5.61009905	5.4698434	6	15.8329512	9.04084507	7.89353096	7.57227863	7.34281581
7	10.2040879	7.1428583	6.29251494	6.29252305	6.29251494	7	13.5749072	8.00432635	6.92266167	6.6522455	6.65223906
8	13.7404541	8.53574204	7.8417769	7.63359001	7.28660744	8					
Average Response	10	6	6	6	6	Average Response	15	8.8	8	7.4	7.3
Standard Deviation	2	1	1	1	1	Standard Deviation	1	0.6	1	0.6	0.5
Overall Coefficient of Variance		32%	Overall Coefficient of Variance (first exposure exempt)		18%	Overall Coefficient of Variance		34%	Overall Coefficient of Variance (first exposure exempt)		12%

Table A3.4. Device-to-device variance of fully-drawn sensors on 4 different substrates. Normalized average conductive response to 50 ppm pyridine 5 consecutive times for 30 s with recovery time of 60 s. Devices were fabricated by depositing SWCNT:TEC (2:1 mass ratio) between graphite electrodes onto silicon, adhesive tape, and laser-etch substrates (weighing paper and PMMA).

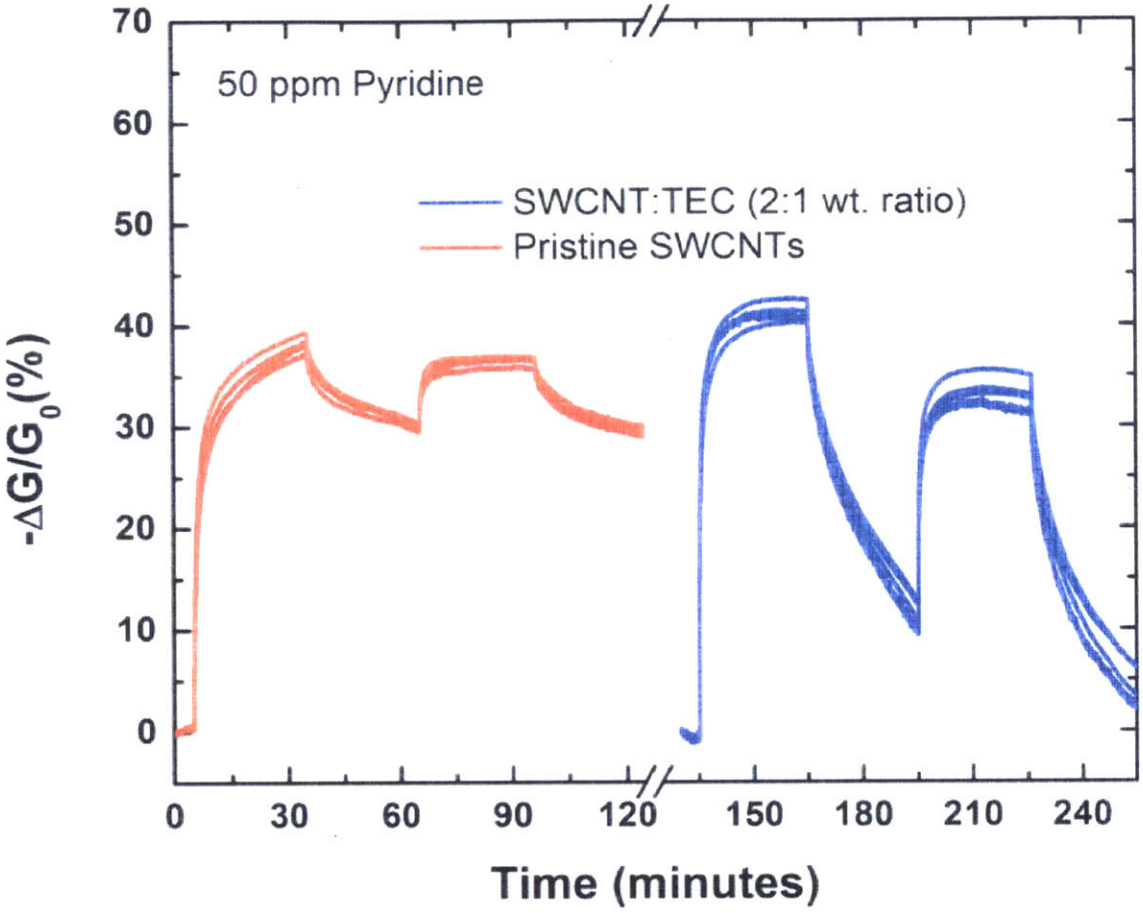

Figure A3.17. Investigation of sensing material's level of saturation towards pyridine vapor. PENCILs were deposited onto the surface of weighing paper between gold electrodes by abrasion. Resistance range of the sensors was between 100-200 kΩ. Normalized change of conductance over time for three devices simultaneously exposed 2 consecutive times to 50 ppm pyridine for 30 min with recovery time of 30 min.

	Chip #1 (-ΔG/G$_0$ %)				Chip #2 (-ΔG/G$_0$ %)			
Analyte	*1L*	*2L*	*3L*	*1S*	*1L*	*2L*	*3L*	*1S*
20 ppm Aniline	3.4998	4.0516	3.6254	0	3.3014	3.7777	3.0573	0
20 ppm Pyridine	6.2208	4.7428	4.9264	2.0746	5.9505	4.7035	4.3998	1.9809
20 ppm Triethylamine	5.6991	1.574	1.6256	3.0164	5.611	1.8037	1.6026	2.7151
381 ppm Toluene	2.2031	0.6984	1.0727	0.6223	2.035	0.6515	0.6662	0.4348
112 ppm m-Xylene	3.3803	0.7532	0.9402	1.1403	3.1614	0.8528	0.578	1.1362
1050 ppm Benzene	1.1924	0.7027	0.7014	0	1.2877	0.5016	0.7824	0.4932
1942 ppm Hexane	1.5517	0	0	0.7222	1.6472	0	0	0.65
20 ppm DMMP	1.7806	0.9568	0.8761	1.8728	2.1472	0.8766	0.7754	1.9125
3002 ppm Acetone	1.4481	0	0.6461	2.9139	1.6929	0.9648	0.6594	2.8587
1262 ppm Ethyl Acetate	1.0999	0.7478	0.3035	1.7982	1.242	0.6078	0.3362	1.5855

Table A3.5. Average Sensory Response of Array

	Analyte	Principal Component Scores			
Chip #1 (-ΔG/G$_0$ %)	*20 ppm Aniline*	3.02041886	-2.2582316	0.16862097	-0.0523087
	20 ppm Pyridine	5.93957538	0.01273108	0.40486797	0.32616433
	20 ppm Triethylamine	2.10436342	2.49164718	-0.6514034	-0.0291783
	381 ppm Toluene	-1.0189453	-0.5285157	-0.4579539	0.30565414
	112 ppm m-Xylene	-0.295261	0.44041291	-0.8795789	0.12017623
	1050 ppm Benzene	-1.8842341	-1.3814037	-0.3313354	0.07221962
	1942 ppm Hexane	-2.3889098	-0.2245515	-0.5225976	-0.0097312
	20 ppm DMMP	-1.1518008	0.18432001	0.64423895	-0.0218121
	3002 ppm Acetone	-1.9531439	1.21638674	1.14113892	0.43459919
	1262 ppm Ethyl Acetate	-2.0045452	0.03376882	0.78996348	-0.2851886
Chip #2 (-ΔG/G$_0$ %)	*20 ppm Aniline*	2.43645335	-2.1016593	0.04042156	-0.2872058
	20 ppm Pyridine	5.46054595	-0.0297108	0.3509106	-0.0294911
	20 ppm Triethylamine	2.14737117	2.14641303	-0.7209601	-0.1904269
	381 ppm Toluene	-1.3811679	-0.6236774	-0.604803	0.04287467
	112 ppm m-Xylene	-0.5688699	0.39697562	-0.8148094	-0.2086747
	1050 ppm Benzene	-1.8619098	-0.9127429	-0.1163166	0.25382786
	1942 ppm Hexane	-2.3348963	-0.2340929	-0.6289596	-0.0116566
	20 ppm DMMP	-1.0221521	0.44393529	0.38518922	-0.0569804
	3002 ppm Acetone	-1.2493162	0.94818345	1.27700276	-0.2042837
	1262 ppm Ethyl Acetate	-1.9935757	-0.0201882	0.52636351	-0.168578

Table A3.6. Principle Component Scores

Principle Component Coefficient			
0.73209117	0.25912844	-0.6295497	-0.0237101
0.4423137	-0.499677	0.33376159	-0.6657963
0.42100412	-0.4312922	0.2839683	0.74572417
0.30192159	0.70509743	0.64158584	-0.0069694

Table A3.7. Principle Component Coefficient

Hotelling's T^2 Statistic
5.11362545
8.20499205
6.03780699
3.05248265
2.23169517
2.25655176
1.50846816
1.16644824
9.0487706
3.94479193
5.99264882
4.7774959
5.98922314
1.4272243
2.68904729
2.67792425
1.74917323
0.70712322
5.52751278
1.89699407

Table A3.8. Hotelling's T^2 Statistic

Principal Component Eigenvalues
19.7631869
6.26920716
2.90945992
0.90057793

Table A3.9. Principal Component Eigenvalues

Percentage of the Total Variance
66.2251219
21.00769525
9.749406226
3.01777662

Table A3.10. Percentage of the Total Variance

Chapter 4

Mechanical Abrasion of Chemiresistive Anion Sensor Array Based on Single-Walled Carbon Nanotubes

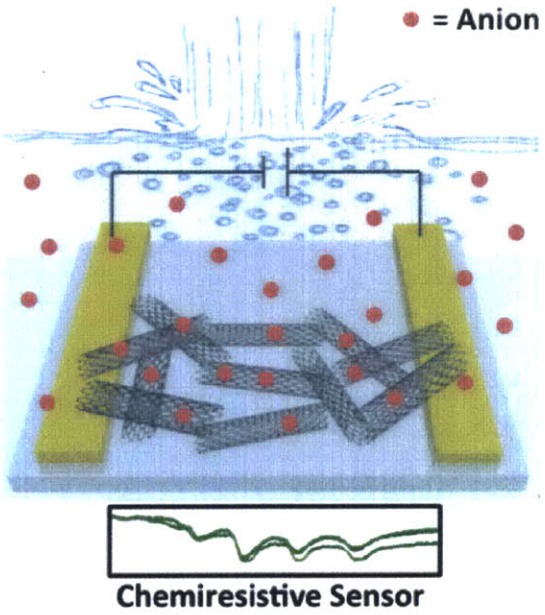

4.1 Introduction

Chemical sensing in a liquid media has an important role for the monitoring of environmental water pollution (e.g., seawater, ground water, and drinking water),[1,2] food quality,[1,3] human health,[1,4,5] and chemical warfare agents.[3] Anions, in particular, have a wide range of environmental, clinical, chemical, and biological relevance.[3,6] Exposure to certain anions, for example cyanide (CN^-), can lead to the disruption of bodily functions, including the vascular, visual, central nervous, cardiac, endocrine, and metabolic systems.[3] Other anions, such as fluoride (F^-), can be beneficial to dental health and treat osteoporosis, however overexposure can lead to acute gastric and kidney problems and bone diseases.[5,7] Current methods for detecting anions include optical (colorimetric and/or fluorescence) sensors,[3,5–14] liquid chromatography-mass spectrometry (LC-MS),[15] electrospray ionization tandem mass spectrometric (ESI-MS-MS),[1,4,16] and electrochemical techniques.[17] Optical sensors are one of the more popular methods for detecting anions due to its simple, inexpensive, and rapid implementation. However, the technique often suffers from the disadvantages of water insolubility of the transducing molecules, low quantum yields in water, high detection limits, poor photostability, or interference anions. To overcome these challenges and create new generations of sensors, we have developed a new solvent-free approach to fabricate chemiresistive anion sensors using carbon nanotube-based composites.

Single-walled carbon nanotubes (SWCNT) are essentially a single layer of graphene, sp^2 hybridize carbon sheet with a honeycomb lattice, rolled into a cylinder. Depending on the chirality (rolling of tube), the nanotubes can either be metallic and semiconductors.[18] The conductance of semiconducting nanotubes is highly sensitive to environmental effects making carbon nanotubes ideal material for sensory applications. Although the nanotubes are naturally

sensitive to their environment, they generally lack selectivity and response to many different molecules and ions. The nanotubes sensitivity and selectivity towards specific analytes can easily be manipulated by covalently or non-covalently functionalizing the nanotubes.[19–31] Covalent functionalization disrupts the nanotube sp^2 hybridization thereby rendering the tube less conductive. In contrast, non-covalent functionalization can largely preserve the nanotube's original conductance. Processing the nanotubes for device applications is normally done be dispersing the nanotubes in organic solvents that can be toxic and/or hazardous.[19,21,22,24,31] Recently, we[32–35] and others[36,37] have fabricated "PENCILs" (**p**rocess-**e**nhanced **n**ano**c**arbon for **i**ntegrated **l**ogic) made of compressed mixtures of carbon materials and selectors where the devices are fabricated using the "DRAFT" (**d**eposition of **r**esistors with **a**brasion **f**abrication **t**echnique) method. This is a simple, cost-effective, solvent-free technique where the PENCILs can abrade onto a wide array of substrates. In some cases a pre-etching treatment is required, however this method can be used to produce well defined geometries.[32]

Glass is an inexpensive, non-porous, mostly inert substrate that has ideal properties for liquid sensing applications. To obtain a highly robust and stable SWCNT-based film on the surface of glass during liquid sensing, the nanotubes are immobilized onto the glass substrate non-covalently by using selectors with an aromatic ring that promotes π-π stacking with the nanotubes and an alkoxy silyl group that can covalently attached onto the glass surface functionalized with hydroxyl groups and also produce a crosslinked polymer network (via hydrolysis).[19] The alkoxy silyl group can also be used to detect F^- and CN^- by undergoing Si-O and Si-C bond cleavage. [5,7,11,13] This approach yields highly sensitize, selective, inexpensive, on-demand sensors capable of detecting anions within minutes.

4.2 Results and Discussion

The PENCILs were fabricated by mechanically mixing 50 mg SWCNTs with 25 μL phenyltriethoxysilane (PTES) and compressing the carbon-based mixture into a pellet. The PENCILs were then deposited between and on top of gold electrodes with a 300 μm gap size by mechanical abrasion onto the surface of chemically-etched glass substrate until 0.5–2 kΩ resistance range was achieved. To catalyze the hydrolysis reaction, between the alkoxy silyl group and the hydroxyl group on the surface of the glass, the substrate was heated at 60°C for 10 min before any sensory measurements were conducted. A small voltage (50 mV) was applied to the sensor and the current was monitored during the analyte exposures. We used F^- (causes bone disease fluorosis and used in the manufacture of nuclear weapons)[5,11] and CN^- (toxic industrial hazard and chemical warfare agent)[3] anions as our model analytes to test this system. An exposure to CN^- concentrations above 300 ppm within minutes will cause human death by depressing the central nervous system.[8] The United State Environmental Protection Agency (EPA) has set the maximum contaminant level (MCL) for CN^- and F^- in drinking water at 200 ppb[3,38] and 4ppm[39], respectively.

Figure 4.1 displays the sensory performance over a period of time of pristine SWCNTs and SWCNT:PTES mixture upon simultaneous exposures to the EPA's MCL of CN^- (200 ppb) and F^- (4 ppm) anion. Each solution used Na^+ to form the salt solution in Milli-Q water. The sensors were simultaneously exposed to the salt solution four consecutive times for 5 min with a recovery time of 10 min. The SWCNT:PTES mixture showed reproducible enhanced sensory responses towards both F^- and CN^- compared to pristine SWCNTs. The proposed mechanism

behind SWCNT:PTES increase in resistance may be the result of active Si-O and/or Si-C bonds residing between the nanotubes that can be activated of cleaved. These reactions can create static charges or dipoles proximate to the CNTs or higher potential barrier for electron to tunnel between tube-tube contacts. The first exposure consistently produced the highest and partially reversible response with a 9-fold or 2-fold enhanced sensitivity, compared to pristine SWCNTs, towards 4 ppm F^- or 200 ppb CN^-, respectively. The additional exposures were less intensive and reversible responses. The recovery kinetics after the additional exposures to 4 ppm F^- typically takes 50 min for the complete recovery of the initial baseline (Figure A4.2). Overall, the immobilized SWCNTs with PTES as a selector had a higher response and better baseline compared to the pristine SWCNT's unstable baseline and a negligible increase in conductivity (which could be due to the ionic strength of the salt solution).

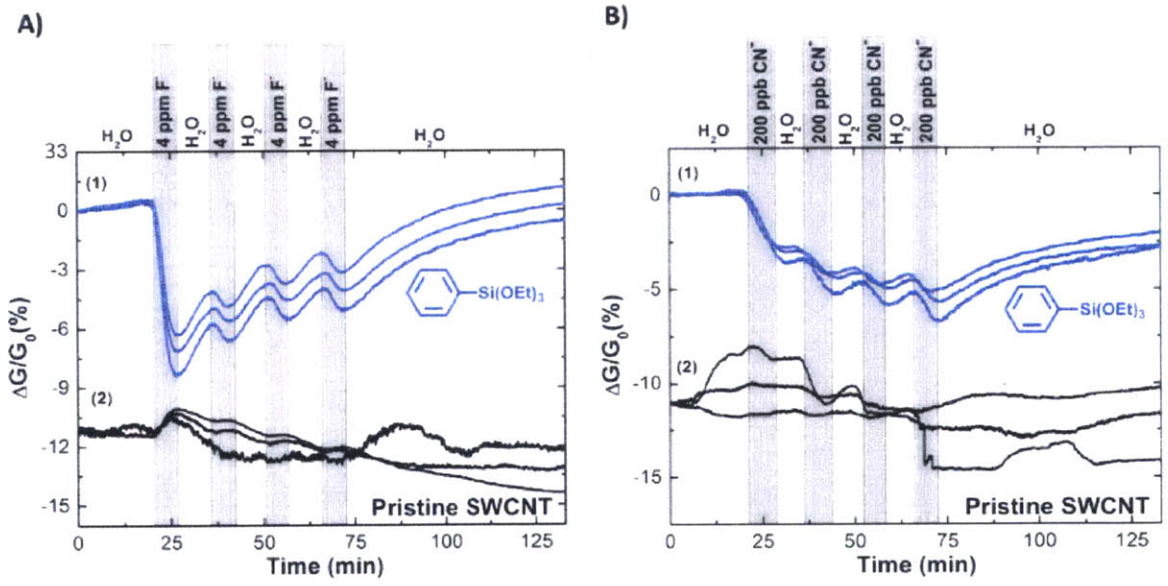

Figure 4.1. Single-walled carbon nanotube (SWCNT) based chemiresistive response towards anions. Plot displays sensory response traces over a period of time for pristine SWCNT and SWCNT:PTES (50 : 0.025 m/v ratio) exposed simultaneously to A) 4ppm F^- and B) 200 ppb CN^- four consecutive times for 5 min with a 10 min recovery rate.

We further investigated other receptors known to react/bind with F^- and CN^- to differentiate between F^- and CN^- responses. The following two additional functional groups can be used to detect F^- and CN^-: thiourea and salicylaldehyde moieties. The thiourea moiety is known to hydrogen bond to various anions.[10] The salicylaldehyde moiety is known to undergo selective nucleophilic addition by CN^-.[3,9,12] We initially investigated the thiourea selector with and without the alkoxy silyl group (Figure A4.3) and observed a response towards 4 ppm F^- exposures for both thiourea-selectors derivatives. The thiourea selector without the alkoxy silyl group demonstrated hydrogen bonding towards the F^-, however the response was weak and the baseline was unstable. Therefore, the alkoxy silyl group is important to facilitate stable baseline of the sensor wherein an additional selector is needed to improve selectivity. Figure 4.2 shows sensory performance over a period of time of pristine SWCNTs, SWCNT:PTES (50 : 0.025 m/v ratio), SWCNT: Thiourea-Selector (50 : 0.25 m/v ratio), and SWCNT:Salicylaldehyde-selector:PTES (50 : 50 : 0.025 m/m/v ratio) mixtures upon exposure to the EPA's MCL of CN^- (200 ppb) and F^- (4 ppm) anion. The thiourea-selector shows enhanced sensitivity towards F^- and CN^- compared to pristine SWCNT, however the difference is smaller than SWCNT:PTES performance and the device selectivity is not improved by this recognition element. We also have determined that thiourea hydrogen bonding motifs generally displays poor selectivity between anions.[6] Therefore, the thiourea-selector was removed from the sensor array. Interestingly, the SWCNT:Salicylaldehyde:PTES mixture showed a slight decrease in resistance

upon exposure to both F^- and CN^-. This could be the result of ionic strength of the salt solution (pristine SWCNTs also display a similar response). The combination of pristine SWCNT, SWCNT:PTES and SWCNT:Salicylaldehyde-selector:PTES in a sensory array could potential selectively detect F^- and CN^- at higher concentrations compared to other interference anions.

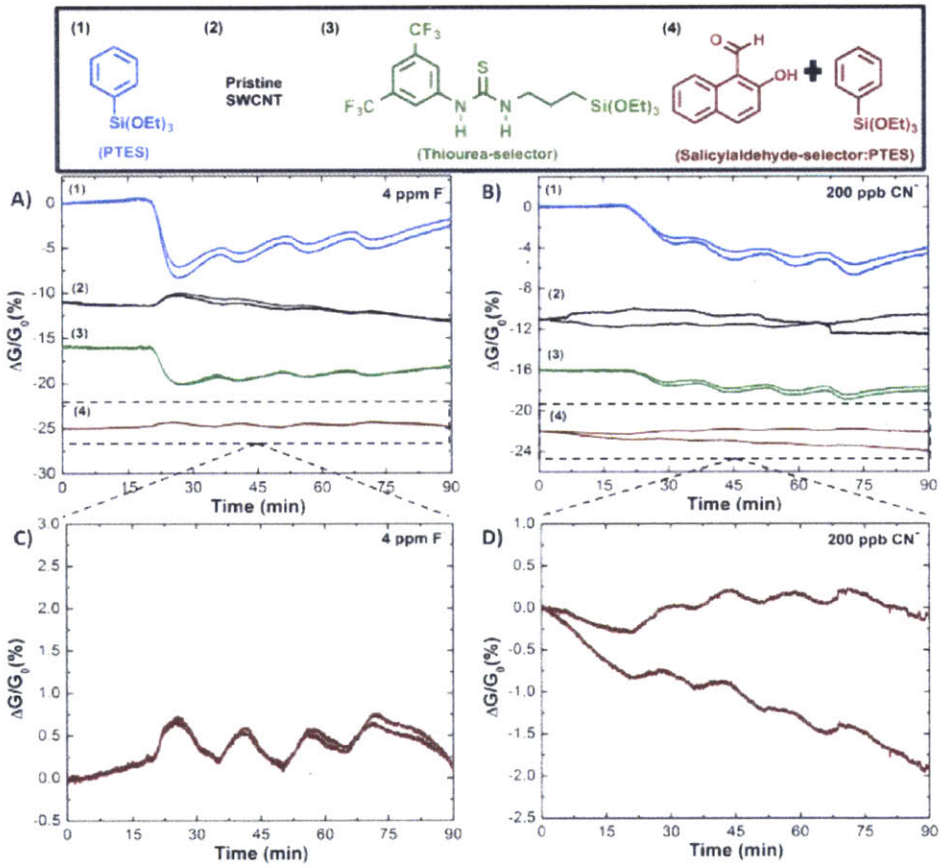

Figure 4.2. Single-walled carbon nanotube (SWCNT) mixed with various selectors chemiresistive response towards anions. Plot displays sensory response traces over a period of time for pristine SWCNTs, SWCNT:PTES (50 : 0.025 m/v ratio), SWCNT: Thiourea-Selector (50 : 0.25 m/v ratio), and SWCNT:Salicylaldehyde-selector:PTES (50 : 50 : 0.025 m/m/v ratio) mixtures exposed to A) 4 ppm F^- and B) 200 ppb CN^- four consecutive times for 5 min with a 10 min recovery rate. The sensory performance of SWCNT:Salicylaldehyde-selector:PTES mixture is shown in response towards C) 4ppm F^- and D) 200 ppb CN^- exposures.

Sensor arrays can be used to fingerprint analytes to yield highly selective detection of anions at various concentrations. Therefore, the components of the array should have some level of selectivity towards targeted anions to minimize the interference of other anions. Figure 4.3 displays a bar graph of average sensory responses of two devices from pristine SWCNTs, SWCNT:PTES (50 : 0.025 m/v ratio), and SWCNT:Salicylaldehyde-selector:PTES (50 : 50 : 0.025 m/m/v ratio) mixtures exposed one time for 5 min towards 4ppm of various anions (F^-, CN^-, $H_2PO_4^-$, and Cl^-) using Na^+ to form the salt solutions. The PENCILs with selectors had the same relative responses compared to pristine SWCNTs toward interference anions ($H_2PO_4^-$ and Cl^-) where there was little to no response. In contrast, the SWCNT:PTES mixture displays an increase in response to F^- and CN^- compared to pristine SWCNTs as previously observed. The SWCNT:Salicylaldehyde-selector:PTES mixture showed an increase in response only towards CN^- exposure compared to pristine SWCNT sensory responses. The possible mechanism for the selective response towards CN^- anion is that the nucleophillic addition of CN^- to the salicylaldehyde moiety carbonyl group creates a lone pair of electrons that can effectively pin the nanotube hole charge carriers, thus decreasing the nanotube conductance (Scheme 4.1).

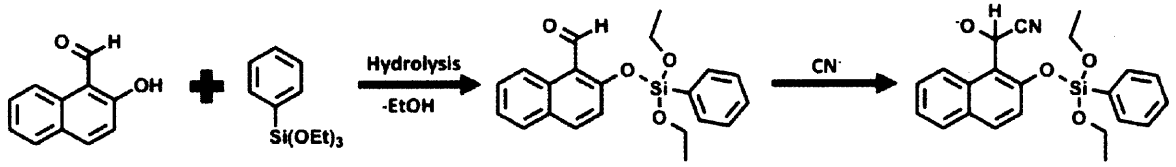

Scheme 4.1. Proposed mechanism for CN^- detection using the Salicylaldehyde-selector

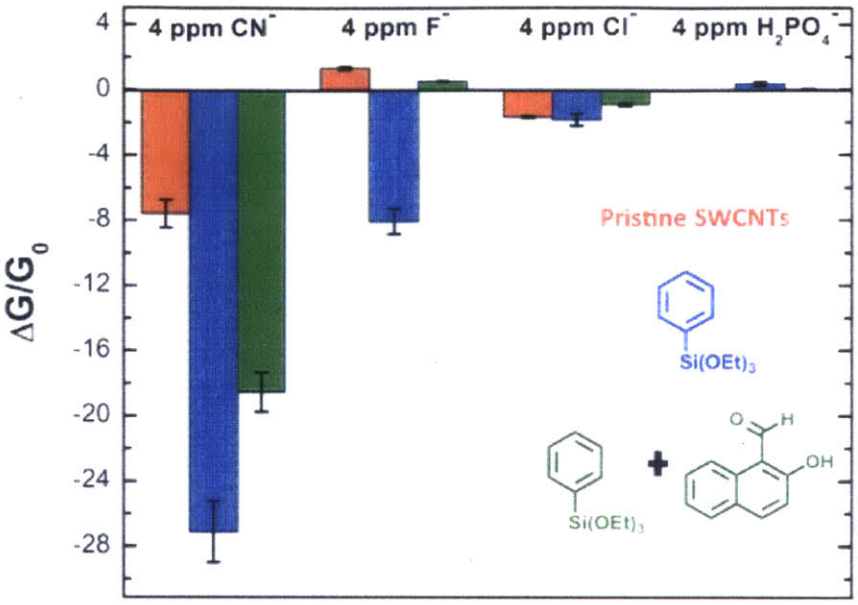

Figure 4.3. Bar graph of average chemiresistive array responses of two devices simultaneously exposed one time for 5 min to 4 ppm of various anions (F^-, CN^-, $H_2PO_4^-$, and Cl^-). The red, blue, and green bars correlates to fabricated sensors using pristine SWCNTs, SWCNT:PTES (50 : 0.025 m/v ratio), and SWCNT:Salicylaldehyde-selector:PTES (50 : 50 : 0.025 m/m/v ratio) mixtures, respectively.

4.3 Conclusion

We demonstrated the first fabrication of carbon nanotube-based chemiresistive anion sensor array by mechanical abrasion that can selectively detect and differentiate between F^- and CN^-. Our sensor was able to detect EPA MCL of F^- and CN^- anion within minutes, therefore can be used in practical systems. The use of an array can create a selective sensor with simple molecules without the need of synthesizing highly designed receptors. This method can be extended towards sensing other metal cations, small molecules, and protein contaminants.

4.4 Experimental Section

Thiourea-Selectors were synthesized by an established method.[19] Sodium chloride (cat. no. S7653-1KG), sodium cyanide (cat. no. 380970-5G), sodium nitrate (cat. no. 221341-500G) and 2-Hydroxy-1-naphthaldehyde (cat. no. H45353-25G) were purchased from Sigma Aldrich. Sodium phosphate dibasic anhydrous (cat. no. 7917-04) was purchased from Mallinckrodt Chemicals. Sodium fluoride (cat. no. A13019) and phenyltriethoxysilane (cat. no. L04684) were purchased from Alfa Aesar. Nano-C, Inc (Westwood, MA) provided purified SWCNTs (>95% SWCNTs). All chemicals and reagents were used without further purification, unless noted otherwise. SWCNTs, selector(s), and two 7 mm diameter stainless steel grinding balls were added into a 5 ml stainless steel ball-milling vial. The ball-milling vial was placed into a mixing mill (MM400, Retsch GmbH, Haan, Germany) where the carbon material was mechanically mixed at 30 Hz for 5 min under ambient conditions. The SWCNTs:selector mixture was then placed into a custom-made stainless steel pellet mold with 2 mm internal diameter where the SWCNT composites were compressed (Carver Press, model # 3912) for 1 min to make PENCILs. The PENCILs were stored at ~4°C to stabilize the PENCILs for a longer duration of time.

A thick layer of etching cream (Cat. No. 15-0200, Armour Products) was applied to cover the entire surface of the glass slides (cat. no. 16004-422, VWR International) and allowed to remain for 5 min. All traces of the Armour Etch Cream were washed with distilled water and dried using a stream of nitrogen. The etched glass slides were then cleaned with an UV Ozone Cleaner (Model no. 2, Jelight Company, Irvine, CA, http://www.jelight.com) for 10 min.

Using a stainless steel mask (purchased from Stencils Unlimited, Lake Oswego, OR, http://www.stencilsunlimited.com), layers of chromium (10 nm) and gold (75 nm) were deposited onto the glass substrate using thermal evaporation (Angstrom Engineering, Kitchener, Ontario, Canada). There was a 300 μm gap between the metal electrodes. The PENCILs were inserted into a holder (item no. DA, Alvin Tech DA) and deposited using DRAFT between and on top of the metal electrodes until 0.5–2 kΩ resistance range was achieved (as measured across the electrode gap with a multimeter). The device was then place on a hotplate and heated for 10 min at 60°C (measured with a thermocouple) before any sensory experiments.

The sensor chip was placed in a 2 × 30 pin edge connector and enclosed in a home-made Teflon enclosure equipped with an inlet, an outlet, and an internal channel for solution flow. Measurements of current were performed under a constant applied voltage of 50 mV using a PalmSense EmStat-MUX equipped with a 16-channel multiplexer (Palm Instruments BV, The Netherlands). The current through the sensor was monitored while exposing it to various anions solutions (delivered using Kd Scientific dual-syringe pump model KDS200, Hayward, CA) using Milli-Q water (Resistance 18.2 MΩ-cm) at 0.5 mL/min flow rate four consecutive times for 5 min with a recovery time of 10 min.

4.5 References

(1) Breitbach, Z. S., Berthod, A., Huang, K. & Armstrong, D. W. Mass spectrometric detection of trace anions: The evolution of paired-ion electrospray ionization (PIESI). *Mass Spectrom. Rev.* (2015). doi:10.1002/mas.21448

(2) Bruggink, C., van Rossum, W. J. M., Spijkerman, E. & van Beelen, E. S. E. Iodide analysis by anion-exchange chromatography and pulsed amperometric detection in surface water and adsorbable organic iodide. *J. Chromatogr. A* **1144,** 170–174 (2007).

(3) Xu, Z., Chen, X., Kim, H. N. & Yoon, J. Sensors for the optical detection of cyanide ion. *Chem. Soc. Rev.* **39,** 127–137 (2009).

(4) Minakata, K. *et al.* Determination of iodide in urine using electrospray ionization tandem mass spectrometry. *J. Chromatogr. B* **878,** 1683–1686 (2010).

(5) Mahapatra, A. K. *et al.* Colorimetric and ratiometric fluorescent chemodosimeter for selective sensing of fluoride and cyanide ions: tuning selectivity in proton transfer and C–Si bond cleavage. *RSC Adv.* **5,** 10716–10722 (2015).

(6) Sun, Y., Wang, G. & Guo, W. Colorimetric detection of cyanide with N-nitrophenyl benzamide derivatives. *Tetrahedron* **65,** 3480–3485 (2009).

(7) Liu, Y., Wang, S.-Q. & Zhao, B.-X. A novel pyrazoline-based fluorescent probe for detecting fluoride ion in water and its application on real samples. *RSC Adv.* **5,** 32962–32966 (2015).

(8) Wei, S.-C., Hsu, P.-H., Lee, Y.-F., Lin, Y.-W. & Huang, C.-C. Selective Detection of Iodide and Cyanide Anions Using Gold-Nanoparticle-Based Fluorescent Probes. *ACS Appl. Mater. Interfaces* **4,** 2652–2658 (2012).

(9) Sun, Y., Liu, Y. & Guo, W. Fluorescent and chromogenic probes bearing salicylaldehyde hydrazone functionality for cyanide detection in aqueous solution. *Sens. Actuators B Chem.* **143,** 171–176 (2009).

(10) Yang, W., Shao, J., Xu, Y., Zhou, W. & Xie, J. Fluorescence detection of iodide anion using a donor–acceptor (D–A) thiourea derivative. *J. Photochem. Photobiol. Chem.* **292,** 49–55 (2014).

(11) Kim, T.-H. & Swager, T. M. A Fluorescent Self-Amplifying Wavelength-Responsive Sensory Polymer for Fluoride Ions. *Angew. Chem.* **115,** 4951–4954 (2003).

(12) Lee, K.-S., Kim, H.-J., Kim, G.-H., Shin, I. & Hong, J.-I. Fluorescent Chemodosimeter for Selective Detection of Cyanide in Water. *Org. Lett.* **10,** 49–51 (2008).

(13) Sokkalingam, P. & Lee, C.-H. Highly Sensitive Fluorescence 'Turn-On' Indicator for Fluoride Anion with Remarkable Selectivity in Organic and Aqueous Media. *J. Org. Chem.* **76,** 3820–3828 (2011).

(14) Thomas, S. W., Joly, G. D. & Swager, T. M. Chemical Sensors Based on Amplifying Fluorescent Conjugated Polymers. *Chem. Rev.* **107,** 1339–1386 (2007).

(15) Mottier, N., Jeanneret, F. & Rotach, M. Determination of Hydrogen Cyanide in Cigarette Mainstream Smoke by LC/MS/MS. *J. AOAC Int.* **93,** 1032–1038 (2010).

(16) Minakata, K. *et al.* Determination of cyanide in blood by electrospray ionization tandem mass spectrometry after direct injection of dicyanogold. *Anal. Bioanal. Chem.* **400,** 1945–1951 (2011).

(17) Poluzzi, V. *et al.* Comparison of two different inductively coupled plasma mass spectrometric procedures and high-performance liquid chromatography with electrochemical detection in the determination of iodine in urine. *J. Anal. At. Spectrom.* **11,** 731–734 (1996).

(18) *Carbon Nanotubes*. **80,** (Springer Berlin Heidelberg, 2001).

(19) Frazier, K. M. & Swager, T. M. Robust Cyclohexanone Selective Chemiresistors Based on Single-Walled Carbon Nanotubes. *Anal. Chem.* **85,** 7154–7158 (2013).

(20) Dionisio, M. *et al.* Cavitand-Functionalized SWCNTs for N-Methylammonium Detection. *J. Am. Chem. Soc.* **134,** 6540–6543 (2012).

(21) Schnorr, J. M., van der Zwaag, D., Walish, J. J., Weizmann, Y. & Swager, T. M. Sensory Arrays of Covalently Functionalized Single-Walled Carbon Nanotubes for Explosive Detection. *Adv. Funct. Mater.* **23,** 5285–5291 (2013).

(22) Wang, F. & Swager, T. M. Diverse Chemiresistors Based upon Covalently Modified Multiwalled Carbon Nanotubes. *J. Am. Chem. Soc.* **133,** 11181–11193 (2011).

(23) Schnorr, J. M. & Swager, T. M. Emerging Applications of Carbon Nanotubes. *Chem. Mater.* **23,** 646–657 (2011).

(24) Liu, S. F., Petty, A. R., Sazama, G. T. & Swager, T. M. Single-Walled Carbon Nanotube/Metalloporphyrin Composites for the Chemiresistive Detection of Amines and Meat Spoilage. *Angew. Chem. Int. Ed.* (2015). doi:10.1002/anie.201501434

(25) Chen, R. J., Zhang, Y., Wang, D. & Dai, H. Noncovalent Sidewall Functionalization of Single-Walled Carbon Nanotubes for Protein Immobilization. *J. Am. Chem. Soc.* **123,** 3838–3839 (2001).

(26) Hirsch, A. Functionalization of Single-Walled Carbon Nanotubes. *Angew. Chem. Int. Ed.* **41,** 1853–1859 (2002).

(27) Sun, Y.-P., Fu, K., Lin, Y. & Huang, W. Functionalized Carbon Nanotubes: Properties and Applications. *Acc. Chem. Res.* **35,** 1096–1104 (2002).

(28) Balasubramanian, K. & Burghard, M. Chemically Functionalized Carbon Nanotubes. *Small* **1,** 180–192 (2005).

(29) Bahr, J. L. & Tour, J. M. Highly Functionalized Carbon Nanotubes Using in Situ Generated Diazonium Compounds. *Chem. Mater.* **13,** 3823–3824 (2001).

(30) Holzinger, M. *et al.* Sidewall Functionalization of Carbon Nanotubes. *Angew. Chem. Int. Ed.* **40,** 4002–4005 (2001).

(31) Esser, B., Schnorr, J. M. & Swager, T. M. Selective Detection of Ethylene Gas Using Carbon Nanotube-based Devices: Utility in Determination of Fruit Ripeness. *Angew. Chem. Int. Ed.* **51,** 5752–5756 (2012).

(32) Frazier, K. M., Mirica, K. A., Walish, J. J. & Swager, T. M. Fully-drawn carbon-based chemical sensors on organic and inorganic surfaces. *Lab. Chip* **14,** 4059–4066 (2014).

(33) Mirica, K. A., Azzarelli, J. M., Weis, J. G., Schnorr, J. M. & Swager, T. M. Rapid prototyping of carbon-based chemiresistive gas sensors on paper. *Proc. Natl. Acad. Sci.* E3265–E3270 (2013). doi:10.1073/pnas.1307251110

(34) Mirica, K. A., Weis, J. G., Schnorr, J. M., Esser, B. & Swager, T. M. Mechanical Drawing of Gas Sensors on Paper. *Angew. Chem. Int. Ed.* **51,** 10740–10745 (2012).

(35) Azzarelli, J. M., Mirica, K. A., Ravnsbæk, J. B. & Swager, T. M. Wireless gas detection with a smartphone via rf communication. *Proc. Natl. Acad. Sci.* **111,** 18162–18166 (2014).

(36) Dossi, N., Toniolo, R., Impellizzieri, F. & Bontempelli, G. Doped pencil leads for drawing modified electrodes on paper-based electrochemical devices. *J. Electroanal. Chem.* **722–723,** 90–94 (2014).

(37) Dossi, N., Toniolo, R., Terzi, F., Impellizzieri, F. & Bontempelli, G. Pencil leads doped with electrochemically deposited Ag and AgCl for drawing reference electrodes on paper-based electrochemical devices. *Electrochimica Acta* **146,** 518–524 (2014).

(38) US EPA, O. Basic Information about Cyanide in Drinking Water. <http://water.epa.gov/drink/contaminants/basicinformation/cyanide.cfm#four>

(39) US EPA, O. Basic Information about Fluoride in Drinking Water. <http://water.epa.gov/drink/contaminants/basicinformation/fluoride.cfm>

Chapter 4 Appendix

Additional Figures

Sensing data acquisition was done using PSTrace software provided by Palm Instruments. Microsoft Excel (2010) was used to calculate normalized sensing responses.

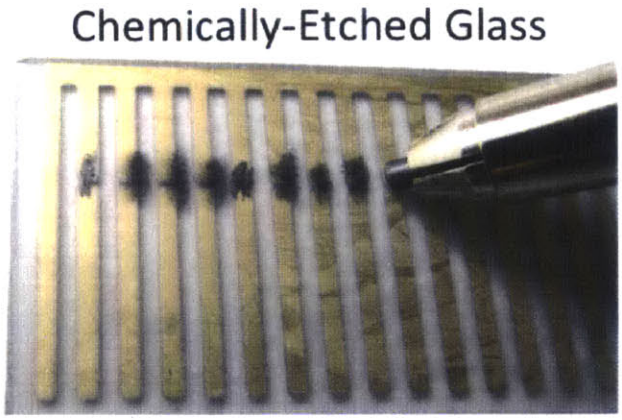

Figure A4.1. Image of PENCILs drawn between and on top of gold electrodes with 0.3 mm gap size on chemically-etched glass by DRAFT method

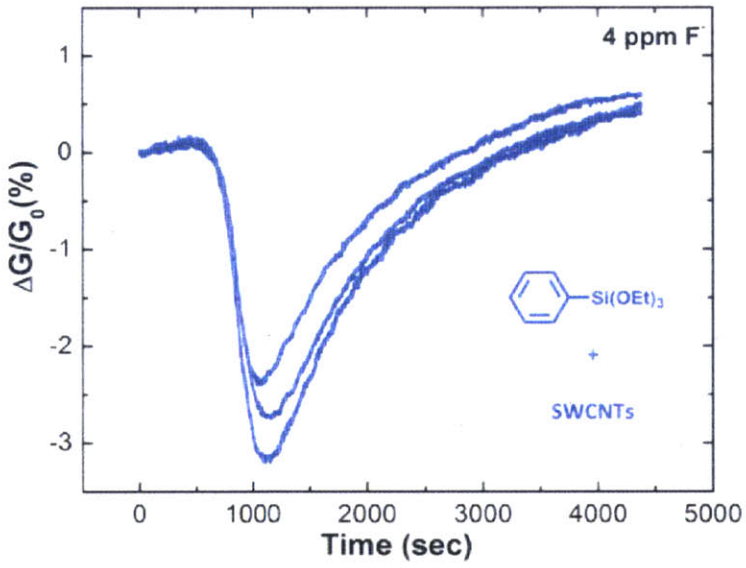

Figure A4.2. Recovery kinetics of SWCNT:PTES exposure to 4 ppm F^- for 5 min.

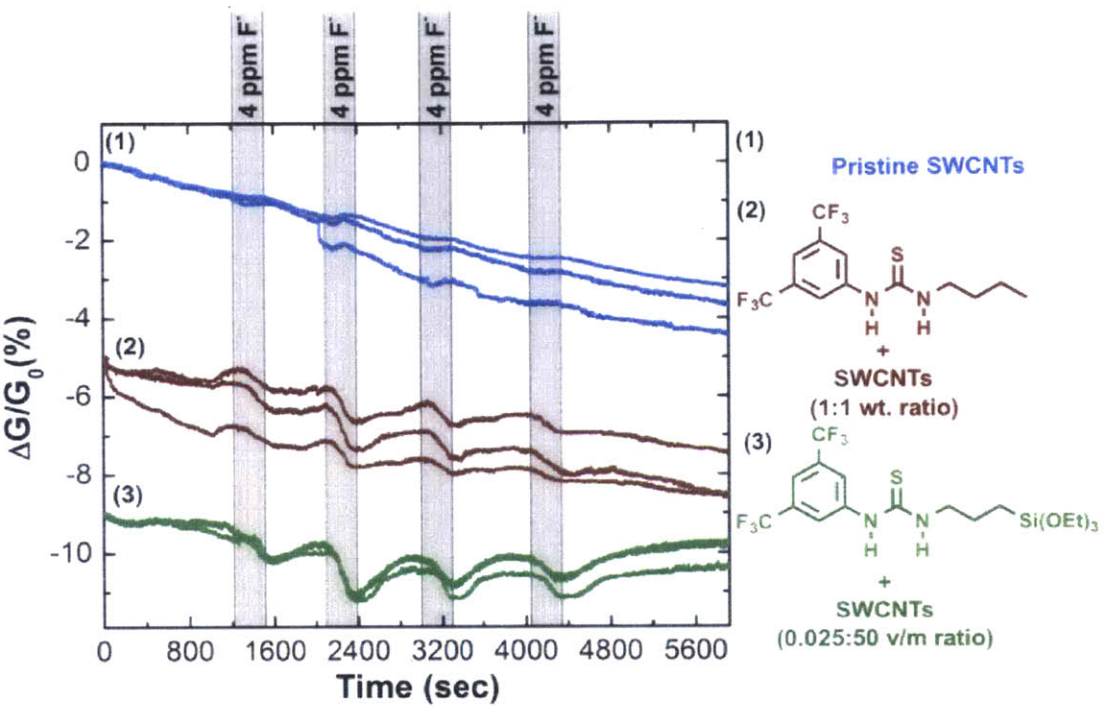

Figure A4.3. Sensory response traces over a period of time for pristine SWCNT and mixtures of Thiourea-selector derivatives simultaneously exposed to 4 ppm F^- four consecutive times for 5 min with a 10 min recovery time. PENCILs were drawn between and on top of gold electrodes with 0.3 mm gap size on chemically-etched glass.

77 Massachusetts Ave, 18-031 Cambridge, MA 02139 frazier@mit.edu

Kelvin Mitchell Frazier

Savannah State University (SSU)		Savannah, GA	Aug. 2006 - May 2010
Dual major: Chemistry and Mathematics	BS	*Magna Cum Laude*	
Massachusetts Institute of Technology (MIT)		Cambridge, MA	Sept. 2010- June 2015
Concentration: Physical Chemistry	Ph.D		

Work Experience

Teacher's Assistant (TA)

- General Chemistry Laboratory (SSU, *August 2008 – May 2009)*
  - Supervised and monitored as a single TA approximately 24 undergraduate students simultaneously while students performed various chemical experiments over the course of the academic year (e.g. fluid thermodynamics, formulation of acid/base and buffer solutions, etc.).
- Solid State Nuclear Magnetic Resonance (SS-NMR) Laboratory (MIT, *January 2011-May 2011 & January 2013-May 2013*)
  - Supervised and monitored as a single TA approximately 48 undergraduate students. The purpose of the course was to educate students to understand the theory behind SS-NMR and analyze two polymers (polystyrene and poly methacrylate) both pure and mixtures where they form a calibration curve and identify the component mixture of an unknown sample.
  - Instructed students how to make samples and explained how to use the SS-NMR equipment including discussions of the theory.
  - Acted as mentor discussing career objectives and research during sessions when samples were scanned for a long duration.
  - Held recitations to help students complete their lab report and graded all lab reports.
  - Achieved highest teacher ratings from the student survey compared to other TAs and faculty in the same module.

Non-Profit Organization: I Turn Research into Empowerment and Knowledge (i-Trek)

- Co-Founding i-Trek Team Member
- Volunteering from *October 2013-Current*
- Aided in establishing mission: to empower underserved and/or underrepresented college students by providing opportunities and resources for them to gain skills, knowledge and experiences necessary to pursue higher degrees in the STEM fields.
- Assisted in selection of pilot program's four undergraduate students from three institutions that where sent to Key Largo, FL June 2014 to do research on coral reef's health.
- Assisted in developing the student program (selecting students, mentor, research project) and successfully solicited funds for the organization

Research/Internship Experience

Summer 2007 at SSU

- Analyzed the mechanism behind the interactions between various proteins and photosensitizers by fluorescence for the development of photodynamic therapy.
- Trained two high school students in the SEED program (Summer Research Internship Program for Economically Disadvantaged High School Students) to perform quality research.

Summer 2008 at the University of Connecticut (UCONN)

- Conducted microwave synthesis of different environmental molecules derivatives by using Raman Spectroscopy as a tool for monitoring the organic reactions.

Summer 2009 at Proctor and Gamble (P&G)

- Developed a technical method that predicts how the target consumers perceive how well body wash rinses off.

Graduate School at MIT (Swager Group)

- Developed a novel, robust, scalable, and simple fabrication method of chemiresistive sensors using chemically modified single-walled carbon nanotubes for various applications (e.g., explosive detection, food quality analysis, etc.).
- Assisted in the successful funding from MIT Deshpande Center for Technological Innovation where funds were directed towards the in-lab start up company C2Sense.

Leadership Experience

- President of the Savannah State University American Chemical Society (ACS) Student Affiliated Chapter from August 2008-May 2010
  - Revitalized organization from zero membership with zero activities to over 50 members with over 20 activities.
  - Steered chapter to receive two national awards consecutively from the ACS Headquarters, making this the first time in SSU history.
- Chemistry Representative for the National Organization for the Professional Advancement of Black Chemist and Chemical Engineers (NOBCChE) MIT Chapter from September 2011-June 2012.
- President of the Academy of Courageous Minority Engineers (ACME) at MIT from January 2011-December 2012.
  - Revitalized organization from zero meeting to over 64 meetings that provided a supportive network for over 20 minority graduate students at MIT. Successfully solicited and received funds to sustain the organization for years after my presidency.
- President of Black Graduate Student Association (BGSA) at MIT from May 2013 – May 2014.

Revitalized organization from zero activities to over 10 activities (e.g., community lunches, workshop, bowling, billiards, etc.).

- Aided in organization's awarding of the 2014 MIT Engineering Community Award at the Office of Multicultural Program's Awards Banquet.
- Wrote proposals for all funded activities.
- Led a full day Personal Branding Workshop where we had approximately 100 attendees at MIT. Our keynote speaker was Ice-T.
  - Wrote proposals that funded the workshop cost.
  - Organized room reservation, equipment rental, food purchase, contracts, tickets sales and publicity.

Publications/Patents

- Jones, C.; Grier, K.; Frazier, K.; "Fluorescence Detection and Interactions of Singlet Oxygen" *J. Undergrad. Chem. Res.* **2008**, 7 (2), 43-47.
- Frazier, KM.; Swager, TM.; " Robust Cyclohexanone Selective Chemiresistors Based on Single-Walled Carbon Nanotubes" *Anal. Chem.* **2013**, 85 (15), 7154-7158.
- Frazier, KM; Mirica, KA; Walish, JJ; Swager, TM; "Fully-drawn carbon-based chemical sensors on organic and inorganic surfaces" *Lab Chip*, **2014**, 14(20), 4059-4066.
- Swager, T.; Frazier, K; Mirica, K; Walish, J; 2014 "Methods and Devices for Deposition of Materials on Patterned Substrates." U.S. Patent Application 62/039,787 filed August 20,2014. Patent Pending

Membership

- Alpha Kappa Mu National Honor Society (top 10% of SSU 2010 graduating class)
- Founding member of the Golden Key International Honor Society Chapter at Savannah State University (top 15% of SSU 2010 graduating class)
- Beta Kappa Mu National Honor Society
- National American Chemical Society (ACS)
- Choral Membership: Kuumba Singers of Harvard College, MIT Gospel Choir, Morningstar Baptist Church Choir, and Joshua 12 (praise and worship team)

Honors/Awards

Undergraduate Studies

- 1st place undergraduate chemistry oral competition: 2007 & 2008 Peach State Louis Stokes Alliance for Minority Participation Conference (PSLSAMP), and 2008 National Historically Black Colleges and Universities Undergraduate Program (HBCU-UP) Conference
  - Competed against over 20 participants at each conference.
- Honorable mention in the 2007 NOBCChE Undergraduate Poster Session Competition
- Outstanding undergraduate chemistry poster award for 2008 Annual Biomedical Research **Conference** for Minority Students (ABRCMS)
  - Competed against thousands of conference participants.
- Travel Awards: ABRCM (2007 & 2008), Society of Toxicology Conference (2008), and ACS National Conference (2008)
- Most outstanding freshmen chemistry student at SSU (2006-2007)
- Most outstanding chemistry student at SSU (2008-2009)
- Most outstanding graduating senior mathematics, chemistry and STEM student at SSU (2010)
- President Second Mile Award: Highest reward given to a graduating senior at SSU (2010)
- Scholarships obtained during my undergraduate studies: MAGEC-STEM, Grady Young Foundation-SSU Foundation, Windsor Forest High School PTA, Hope, Tom Joyner, Band Tiger Ambassador, Choir Tiger Ambassador, T.I.G.E.R, K.B. Raut Endowment, National Alumni, and Chapter 249 National Association of Retired Federal Employee

Graduate Studies

- Daniel S. Kemp Summer Graduate Fellowship 2010 at MIT
- MIT Provost Presidential Fellowship 2010-2011 at MIT
- BGSA Member of the Year 2013-2014.
- MIT 2015 Dr. Martin Luther King, Jr. Leadership Award

Presentations

Undergraduate Studies

- Oral Research Presentations: PSLSAMP (2007-2009), HBCU-UP (2008), and ABRCM (2007)
- Poster Research Presentations: PSLSAMP (2007-2008), ACS (2008), and ABRCM (2008-2009)

Graduate Studies

- Poster Research Presentations: MIT Polymer Day Symposium (March 2012), MIT Materials Day (October 2014), PITTCON conference (March 2014), and NOBCChE National Conference (2012)
- Poster Presentation: MIT IDEAS Global Challenge Competition (2014) for funding opportunities with i-Trek
- Oral Presentation: led Grad Catalysis Workshop at Hampton University (2013) to teach their students how to get into graduate school.
- Oral Research Presentation: NOBCChE National Conference (September 2014)

Acknowledgements

It is hard to believe my five years at MIT are over. While getting to this point, it didn't seem like time was flying by that quickly. I really enjoyed the science and the relationships that I formed while I was at MIT.

First I would like to thank my research advisor, *Timothy Swager*, for taking me in as his student and the great academic, career, and socially advise he has given me over the years. I couldn't have asked for a better advisor/mentor as I matriculated into the MIT community. I loved our meetings (even though your office was cold) where you had so many ideas for research projects and great stories to share about your past experiences.

I would like to thank my thesis chair, *Moungi Bawendi*, for all of his helpful advise during our annual meetings. You really helped me to start thinking more like a physical chemist with my projects instead of an engineer. I valued all of our interactions and appreciate the guidance.

I would also like to thank my third thesis committee member, *Keith Nelson*, for all his great questions during my 2nd year oral and check up meeting during my 3rd year. You always brought up great points that I needed to further investigate to get answers to.

I would like to thank my collaborators *Kat and Joe W.* for all the help in putting things together for the fully drawn sensor paper.

I would like to thank my fellow Swager lab cohorts *Grace Han, John Goods, Jonathan Weis, and Jolene Mork* who joined the Swager group along with me. I really enjoyed our conversations and bonding activities when we were all just first year grad students trying to survive MIT. It has been a long journey.

I would like to thank Swager Lab carbon nanotube sensing team *Birgit, Jan, Kat, Daan, Hitoshi, John F., Jisun, Joe A., and Jon W.* for all the helpful research discussions during my time at MIT.

I would like to thank all of my officemates *Ellen, Joel, Eilaf, Byungjin, Yanchuan, Olesya, Yi, Jan, Jose, Duncan, Stefanie, Jason, John G., Eiji, and Markrete* for all the fun discussions and research advise. I moved around like 3 times during my tenure at MIT. I was in two offices in building 18 and one office in the ISN building.

I will also like to thank the ISN staff *Amy, Donna, Marlisha, Steve, and Bill* who were great people to work with while I was there. If I needed anything, there were always there and I also enjoyed our conversations as well.

I would like to thank the entire Swager group from 2010-2015. This group was so much fun to work with and I enjoyed meeting and having conversations with each of my labmates. I especially enjoyed playing volleyball over the summer with my labmates. We were the 2013 undefeated chemistry department summer volleyball league champions!!!!

I would like to thank all my friends in the Academy of Courageous Minority Engineers (ACME) and Black Graduate Students Association (BGSA) for all the fun activities we did together and helpful advise as we all were graduate students trying to survive MIT. I especially would like to thank *David, Obi, Niaja, Kevin, and Alan* who helped me revitalize these great organizations.

I would like to thank *Dean Staton* for the one-on-one talks we had as I was in need of help to get through the stresses of MIT. I would not have made it through without your help and positive spirit.

I would like to thank choirs that I participated in *MIT Gospel Choir, Called to Praise, Kuumba Singers of Harvard University, Morningstar Baptist Church Choir, and Joshua 12* for all the great music. This was surely the places were I could distress and forget about being a MIT student.

I would also like to thank my roommates *David and Obi* for all the fun times and talks throughout grad school. We all came from similar backgrounds, so it was great to have you as a source to talk. You both knew exactly where I was coming from when I had issues.

I would like to thank all the friends I have gained in the Boston area and my friends from back home in Savannah. You all really helped me to keep my mind off of my studies when I needed the break.

Finally, I would like to thank my family especially my parents *Richard Frazier, Jr. and Edythe Frazier* and my older brother *Ricky Frazier* for all the support that started since the day I was born. I certainly would not be the person I am today without you. You gave me a wise mind and a humble heart. I love you so much and appreciate how you go beyond the common expectations with your support.